Modelling Hydrogen Gas Flow in High Pressure Systems

L.C.M. Drummen

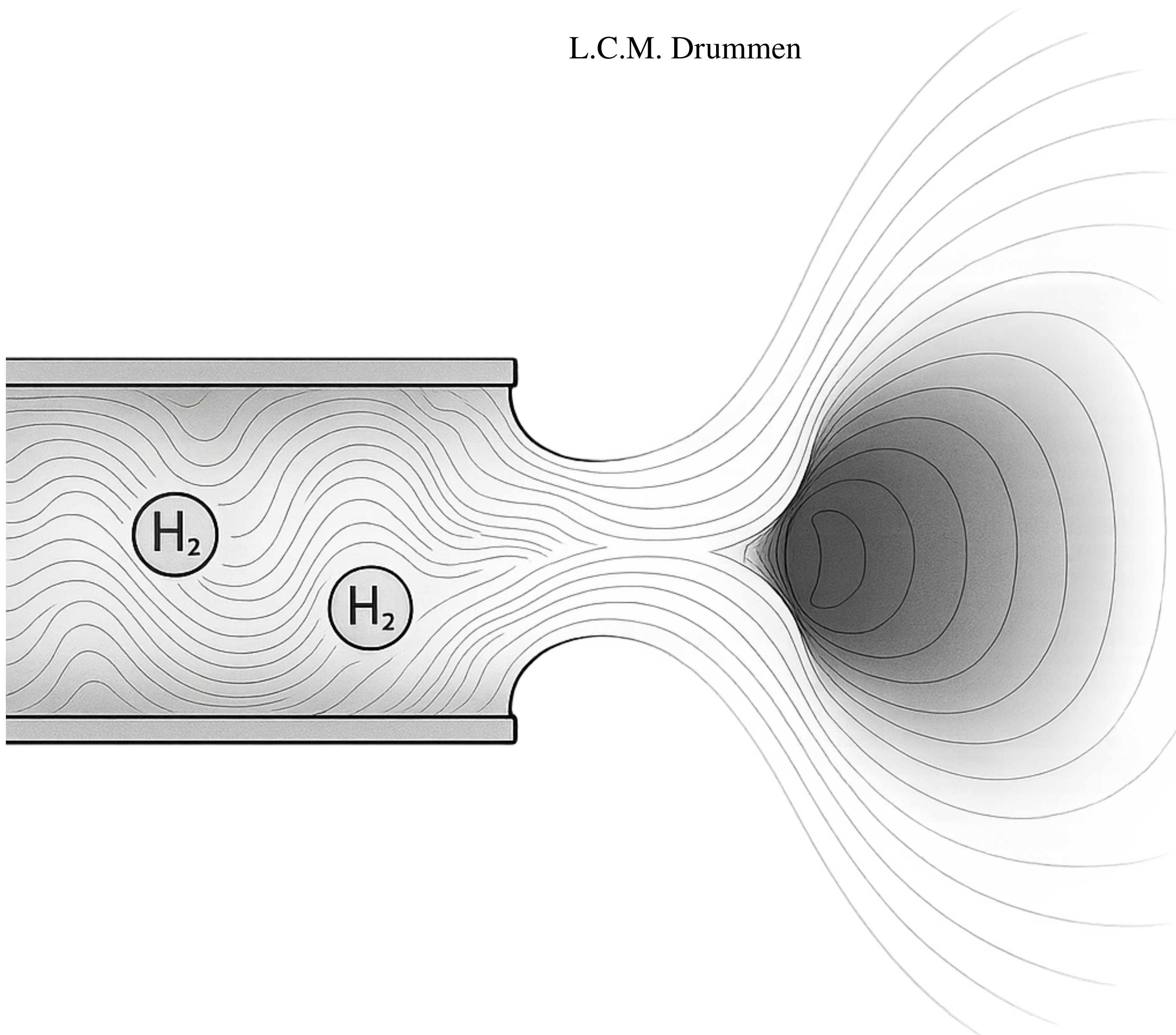

Document Number: 474

Faculty of Engineering Technology
Department Engineering Fluid Dynamics
University of Twente

June 17, 2025

Modelling Hydrogen Gas Flow in High Pressure Systems

Thesis report

by

L.C.M. Drummen

To obtain the degree of Master of Science
at the University of Twente
to be defended on June 20, 2025 at 14:00

Thesis committee:

Chair:	Dr.Ir. E.T.A. van der Weide
Supervisors:	Dr.Ir. J.A.M. Withag
External examiner:	Dr.Ir. J.S. Smink
Company supervisor	ing. R. van Goor
Faculty:	Faculty of Engineering and Technology
Place:	Enschede, The Netherlands
Project Duration:	March, 2024 - June, 2025
Student Number:	2855518
Document Number:	474

Faculty of Engineering and Technology · University of Twente

Summary

By 2030, EU member states must ensure that hydrogen refuelling stations (HRS) are installed along the Trans-European Transport Network, with a maximum spacing of 200 km. Each HRS must provide at least 1 tonne of gaseous hydrogen per day and include a 70 MPa dispenser. Meeting these targets requires a large expansion of the current HRS network, which still faces significant technical and economic challenges.
One major bottleneck in hydrogen transport is pipelines. Due to the low density and high diffusivity of hydrogen, pressure variations during pipeline transport can be significant, especially during fast refuelling, when compressibility effects dominate. These conditions result in high flow velocities, making it difficult to accurately predict outlet pressure and temperature.

This research investigated the following question:
"How can analytical, empirical, and numerical models be used to approximate hydrogen flow in pipelines of varying diameter, and to what extent are they suitable to predict pressure and temperature under measured inlet conditions?"

A selection of commonly used hydrogen pipeline diameters was studied. Experimental data was obtained using a custom-developed test setup, and subsequently compared to analytical, empirical and numerical models. Additionally, shadowgraph imaging was performed at pipeline outlets to visualise flow phenomena.
The investigated analytical and empirical models included: The Darcy-Weisbach, Weymouth, Panhandle, isentropic flow, and Fanno flow equations. Furthermore, a correction on the isentropic flow equations using the Soave-Redlich Kwong equation of state was investigated. Numerical modelling was performed with the SU2 and OpenFOAM CFD codes.

In conclusion, analytical and empirical models offer a fast and reasonably accurate means of estimating outlet conditions in many practical scenarios, particularly when applying Fanno and isentropic formulations. Although the numerical models did not provide a direct method for predicting outlet conditions in the cases considered, they yielded deeper insights into the overall flow behaviour within the pipe.

Nomenclature

Fluid Properties

Symbol	Description	Units
ρ, ρ_0, ρ^*	Density (reference/critical)	kg/m^3
μ	Dynamic viscosity	Pa·s
Z	Compressibility factor	—
n	Refractive index	—
K	Gladstone-Dale constant	m^3/kg

Thermodynamic Properties

Symbol	Description	Units
p, p_0, p^*	Pressure (Total/critical)	Pa
T, T_0, T^*	Temperature (Total/critical)	K
R	Universal gas constant	J/(mol·K)
c_p	Specific heat at constant pressure	J/(kg·K)
c_v	Specific heat at constant volume	J/(kg·K)
γ	Heat capacity ratio	—
α	Acentric factor	—
v_u	Molar volume	m^3/mol
E	Energy	J
α	temperature-dependent correction factor	-

Flow and Kinematic Properties

Symbol	Description	Units
x, y, z	Spatial coordinates	m
u, v, w	Velocity components (x,y,z- direction)	m/s
u^*	Friction velocity	m/s
$\dot{m}$	Mass flow rate	kg/s
Q	Volumetric flow rate	m^3/s
M	Mach number	—
a	Speed of sound	m/s
Re	Reynolds number	—
f	Friction factor	—
A	Area	m^2
D	Pipe diameter	m
L	Length	m
m	Mass	kg
t	Time	s
τ_s	Time scale	s
η_k	Length scale	m

Turbulence and CFD

Symbol	Description	Units
τ_{ij}	Stress tensor components	Pa
τ_w	Wall shear stress	Pa
k	Turbulent kinetic energy	m^2/s^2
ω	Specific dissipation rate	1/s
y^+	Non-dimensional wall distance	—
C_μ	Empirical constant in turbulence models	—

Surface and Optical Properties

Symbol	Description	Units
Ra, Rz, Rq, Rt	Surface roughness parameters	μm
I	Light intensity	W/m^2
H	Slit height or speed of sound	m
ϵ	Roughness height	m
ζ	Coordinate fluid blob	—
θ	Angle	deg
η	Efficiency factor	

Other Symbols and Acronyms

Acronyms	Description
EOS	Equation of State
SAE	Society of Automotive Engineers
HRS	Hydrogen Refuelling Station
TEN-T	Trans-European Transport Network
SD	Standard Deviation
CFD	Computational Fluid Dynamics
RANS	Reynolds-Averaged Navier-Stokes
FANS	Favre-Averaged Navier-Stokes
DNS	Direct Numerical Simulation
LES	Large Eddy Simulation
PISO	Pressure-Implicit with Splitting of Operators
SIMPLE	Semi-Implicit Method for Pressure Linked Equations
PIMPLE	Pressure Implicit Pressure-Linked Equations
SST	Shear Stress Transport model

Contents

1 Introduction

On 28 March 2023, the European Commission agreed on a proposal for a regulation on the deployment of alternative fuels infrastructure. This regulation stated that the Member States must ensure that, by 2030, publicly accessible hydrogen refuelling stations (HRSs) with a minimum cumulative capacity of 1 ton/day and at least a 70 MPa dispenser are placed along the Trans-European Transport Network (TEN-T), no more than 200 km apart [1]. The TEN-T network is shown in Figure 1 and the enlarged version is provided in appendix A.

At the time of writing this document, Europe has 187 HRSs available, of which the majority are in Germany [3, 4]. Various news articles announce a total requirement of 700 HRSs by 2030 [5, 6]. Furthermore, accessing a map of current available HRSs shows that many European member states require much more HRSs [7]. As a result, a drastic increase in the HRS production rate is required before 2030.

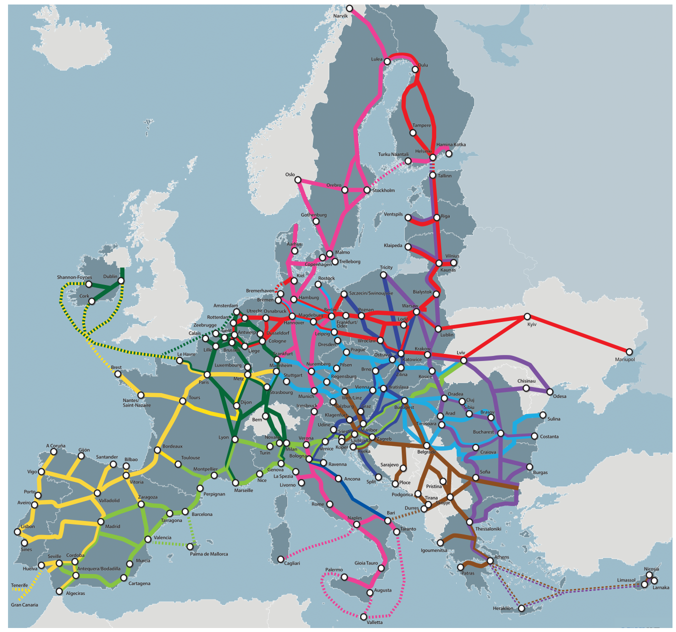

Figure 1: TEN-T Network [2]

At the same time, many technical challenges are still present in the current state of HRSs. The high production, storage, distribution, transmission, utilisation costs and technical challenges associated with refuelling stations remain the major bottleneck in the hydrogen-based transport sector [8].

Therefore, many studies have been performed to overcome these bottlenecks. A large majority of these studies focus on transient-temperature simulations of vessels, yet little studies have focused on the influence of separate system components in HRSs. Moreover, Bourgouis et al. [9] signify the importance of considering the entire fuelling line when studying the fuelling procedure. Kuroki et. al. [10] recognised this research gap and provides as one of the first a model of a complete HRS with empirical relations and a custom algorithm. Additionally, Ebne-Abbasi et. al. [11] implemented a Computational Fluid Dynamics (CFD) model of an HRS to provide deeper insight into the underlying physical phenomena of hydrogen flow.

In the context of system components, pipelines alone present several challenges when used in hydrogen systems. Here, an ongoing research topic is the integration of gaseous hydrogen in existing pipeline infrastructure. Examples of these challenges include leaks, hydrogen embrittlement, and pressure losses. Notably, the roots of these challenges come from the properties of gaseous hydrogen. Under standard conditions, gaseous hydrogen has a very low density and is highly diffusive, leading to high pressure variations during transport [12].

Comparative studies show that gaseous hydrogen has lower pressure losses than other gases because of its low density. However, the mass flow rate of hydrogen is also comparatively lower under similar conditions [13]. Because of the low density and high diffusivity, it is expected that flow velocities in pipelines are much higher than those of denser gases.

The conditions of pressure, temperature, and density are set in an HRS by the Society of Automotive Engineers (SAE). The limits of an H70 vehicle (70 MPa gaseous hydrogen) are shown in Figure 2, showing that pressure, density, and temperature can vary greatly during a refilling process. As a result, pipelines in an HRS must be able to accommodate a wide range of flow conditions, posing unique challenges for the analysis of an HRS.

High mass flow rates are desired in fuelling applications, but uncontrolled fast fuelling can cause numerous problems. Therefore, fuelling protocols have been established for HRSs to ensure a safe and fast fill for hydrogen vehicles. The proposed fuelling protocols are given by the SAE J2601. The SAE J2601 fuelling protocol uses a combination of a lookup table approach and the "MC formula" (mass × specific heat) to control the hydrogen fuelling process.

These methods essentially regulate the rate at which pressure increases in the vehicle's tank, while ensuring that safe temperature and pressure limits are not exceeded [14].

The hydrogen flow conditions encountered in the pipelines of an HRS, particularly at fast fills, can reside in flow regimes where compressibility effects become significant. Due to the combination of low density and high mass flow rate demands, high velocities are involved. As a consequence, Mach numbers can reach values where compressible effects can no longer be neglected. In addition, high Reynolds numbers typically result in turbulent flow throughout most of the pipeline. These combined effects introduce strong pressure and temperature gradients along the pipeline, complicating the accurate prediction of outlet conditions. As such, compressible and turbulent flow modelling becomes essential for analysing and designing hydrogen refuelling systems that are both safe and efficient.

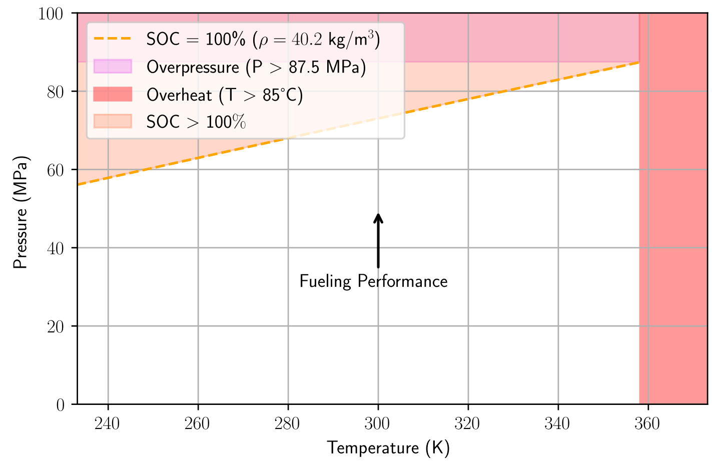

Figure 2: H70 operating window [14]

1.1 Resato High Pressure Technology

This research was conducted at Resato High Pressure Technology, a Dutch company that specialises in high-pressure systems and equipment. Resato develops and manufactures hydrogen testing equipment, such as tank and component testing systems. The practical challenges faced in the development and operation of these systems provided the basis for this research assignment. One of these challenges is the noticeable increasing demand for higher mass flow rates. Resato High Pressure Technology seeks a modelling approach that aids in the prediction of pressure and temperature for a given mass flow rate in a range of their commonly used pipes in hydrogen systems. An overview of the pipe classifications studied in this research is given in Table 1.

Figure 3: Resato High Pressure Technology [15]

In addition, an experimental setup was built in collaboration with Resato High Pressure Technology to perform measurements on the pipes listed in Table 1. Here, Resato High Pressure Technology arranged parts, a test site, and overall support. The setup was used to collect pressure, temperature, and mass flow rate data for validation of a modelling approach.

Designation	Internal diameter [mm]	External diameter [mm]
∅ 8	8	14
∅ 5	5	10
∅ 3.2	3.2	9.6

Table 1: Pipe classifications with available diameters

1.2 Overview of modelling approach

Several analytical and numerical models are used in this research to analyse hydrogen flow in pipelines. The Darcy–Weisbach equation, combined with (approximations of) the Colebrook–White friction factor, is used for initial pressure loss estimates. However, since this formulation is primarily valid for incompressible flow, corrections are required when applied to hydrogen. Therefore, the Fanno flow relation is employed to account for compressibility and frictional effects. To improve accuracy, the Fanno model is further extended by incorporating real-gas behaviour using the Soave-Redlich-Kwong (SRK) equation of state (EOS).
Analytical calculations are implemented in Python using the CoolProp library, which internally uses the NIST EOS. Additionally, numerical simulations are performed using the open-source CFD packages OpenFOAM and SU2. The OpenFOAM simulations are conducted with the SRK EOS, while SU2 is used with the ideal gas law, as neither have the NIST EOS available at the moment. The most appropriate available EOS is chosen for each case to balance accuracy with software capabilities.
The measurements from the experimental setup are compared with the analytical and numerical models. Here, experimentally measured inlet and flow parameters serve as input for the models to compute outlet conditions. The outlet conditions are subsequently compared with the experimental measurements.

1.3 Research questions

The main research question treated in this text is:

"How can analytical, empirical, and numerical models be used to approximate hydrogen flow in pipelines of varying diameter, and to what extent are they suitable to predict pressure and temperature under measured inlet conditions?"

In support of the main research question, the following research questions along with research goals are set:

1. "What is the influence of pipeline diameter, and how do different diameters impact the performance of the modelling approaches?"
2. "To what extent do analytical, empirical, and numerical models agree with experimentally measured outlet conditions, given known inlet conditions?"
3. "How do analytical and empirical models compare with numerical models in predicting the outlet pressure and temperature of a pipe?"

To address these research questions, the following objectives have been formulated:

1. "To validate analytical, empirical, and numerical models against experimental measurements".
2. "To assess the predictive capability of models when only inlet and geometric conditions are known."
3. "To quantify the effect of pipe geometry on pressure and temperature along a pipeline."

1.4 Outline

Chapter 2 presents the analytical and empirical models, along with their dependencies on equations of state and friction factors. Chapter 3 presents the numerical modelling procedure, including the mesh construction, turbulence models, and solution methods. Next, the experimental setup that was used to gather data for the latter models is presented in Chapter 4. Optical flow visualisation techniques are presented, along with their working principles and applicability. To provide additional insight into the resulting images, Chapter 4 concludes a brief theory on shock waves and their common structures. Finally, Chapter 5 presents the methodologies chosen to answer the research questions. The results are given in Chapter 6, discussed and concluded in Chapter 7. Finally, the recommendations are given in Chapter 8.

2 Governing equations

In a modelling approach, the approximation of a state parameters, like pressure and temperature, often depend on simplifying assumptions. Since these assumptions play a crucial role, this section provides a brief overview of the development of analytical and empirical models of general conservation equations. Next, the general conservation equations are introduced, where the first simplifications are applied. The following subsections detail more specific assumptions associated with each model, building from the general conservation equations introduced here.

2.1 Conservation equations

Firstly, the continuity equation:

$$\frac{\partial \rho}{\partial t} + \frac{\partial \rho u_j}{\partial x_j} = 0 \tag{2.1}$$

where ρ is the fluid density, u_j the velocity vector, and x_j the directional vector. The momentum equation:

$$\frac{\partial \rho u_i}{\partial t} + \frac{\partial \rho u_i u_j}{\partial x_j} - \frac{\partial \sigma_{ij}}{\partial x_j} - \rho g_j = 0 \tag{2.2}$$

where $\sigma_{ij} = -p\delta_{ij} + \tau_{ij}$, here δ_{ij} is the Kronecker delta, p is the pressure, μ is the dynamic viscosity, and

$$\tau_{ij} = \mu \left(\frac{\partial u_i}{\partial x_j} + \frac{\partial u_j}{\partial x_i} \right) - \frac{2}{3}\mu\delta_{ij}\frac{\partial u_k}{\partial x_k}. \tag{2.3}$$

The energy equation:

$$\frac{\partial \rho E}{\partial t} + \frac{\partial}{\partial x_j} \left(\rho E u_j - \sigma_{ij} u_i - k\frac{\partial T}{\partial x_j} \right) = \rho g_j u_j \tag{2.4}$$

where k is the thermal conductivity and T is temperature. This research is focused on steady flow, that is,

$$\frac{\partial \phi}{\partial t} = 0 \tag{2.5}$$

with ϕ an arbitrary flow variable. Henceforth, the continuity equation reduces to

$$\frac{\partial \rho u}{\partial x} + \frac{\partial \rho y}{\partial y} + \frac{\partial \rho z}{\partial z} = 0. \tag{2.6}$$

Considering a flow in the x direction and integrating this equation over the surface of an arbitrary system

$$\rho u A = \dot{m} = \text{constant} \tag{2.7}$$

here, $\dot{m}$ represents the mass-flow rate.
For steady flow, the momentum equation reduces to:

$$\frac{\partial \rho u_i u_j}{\partial x_j} - \frac{\partial \sigma_{ij}}{\partial x_j} - \rho g_i = 0 \tag{2.8}$$

Finally, the energy equation reduces to:

$$\frac{\partial}{\partial x_j} \left(\rho E u_j - \sigma_{ij} u_i - k\frac{\partial T}{\partial x_j} \right) = \rho g_j u_j \tag{2.9}$$

The steady conservation equations (Eqs. 2.6, 2.8, 2.9) are further adjusted according to the assumptions stated in the following subsections. The next subsections first discuss the independent function for the analytical models, after which in section 2 the analytical models are presented.

2.2 Dimensionless quantities

An important dimensionless quantity used in this text is the Reynolds number:

$$Re = \frac{\rho \bar{u} D}{\mu} \tag{2.10}$$

where $\bar{u}$ is the averaged velocity in x-direction. The diameter D of a pipe represents the characteristic length, The analysis of the characteristic length is given in Appendix B. As the Reynolds number is significantly affected by variations in both density and velocity, it is convenient to employ a mass flow rate instead for pipe flow, as the density ($\rho(p, T)$) is often not measured directly. As $\rho \bar{u} D = \frac{4}{\pi D}\dot{m}$, we simply substitute the numerator:

$$Re = \frac{4\dot{m}}{\mu \pi D} \tag{2.11}$$

Each fluid exhibits a speed of sound, depending on its microscopic properties. An important ratio between fluids velocity and its speed of sound is the Mach number:

$$M = \frac{u}{a} \tag{2.12}$$

where a is the local speed of sound. For example, the speed of sound in air under standard conditions is $a = 343$ m/s, while for hydrogen under standard conditions, the speed of sound is $a = 1294$ m/s. These differences can be recognised by observing that hydrogen has a much lower density compared to that of air under these conditions. Additionally, density plays an important role when increasing the speed of a fluid to its speed of sound, particularly at $M \simeq 0.3$ [16].

2.3 The friction factor

The internal walls of the pipe induce friction on the flow. Nikuradse [17] conducted experiments in which sand grains were glued to the walls of the pipes, creating artificial roughness. He introduced the relative sand-grain roughness, ϵ/D, whereas the roughness of pipes is still frequently represented by an equivalent sand-grain roughness [18].
From this relation, von Karman introduced an expression for the friction factor of rough pipes. This expression was combined with Prandtl's equation for a smooth pipe friction factor by Colebrook in collaboration with White, resulting in the famous Colebrook-White equation:

$$\frac{1}{\sqrt{f}} = -2\log\left[\frac{2.51}{Re\sqrt{f}} + \frac{\epsilon}{3.7}\right] \tag{2.13}$$

The validity of the Colebrook-White equation is given in Table 2, along with several other explicit approximations of the Colebrook-White equation. As the Colebrook-White equation is of implicit nature, it is convenient to resort to an explicit impression such as the Haaland equation. Some alternative friction factor equations are listed in Table 2.

Equation	Description	Validity
Colebrook-White	$\frac{1}{\sqrt{f}} = -2\log\left[\frac{2.51}{Re\sqrt{f}} + \frac{\epsilon}{3.7}\right]$	$Re = 4000 - 10^8$ $\epsilon = 0 - 0.05$ mm
Haaland	$\frac{1}{\sqrt{f}} = -1.8\log\left[\left(\frac{\epsilon/D}{3.7}\right)^{1.11} + \left(\frac{6.9}{Re}\right)\right]$	$Re = 4000 - 10^8$ $\epsilon = 0.000001 - 0.05$ mm
Swamee-Jain	$\frac{1}{\sqrt{f}} = -2\log\left(\frac{\varepsilon}{3.7} + \frac{5.74}{Re^{0.9}}\right)$	$Re = 5000 - 10^8$ $\epsilon = 0.000001 - 0.05$ mm
Zigrang and Sylvester	$\frac{1}{\sqrt{f}} = -2\log\left[\frac{\varepsilon}{3.7} - \frac{5.02}{Re}\log\left(\varepsilon - \frac{5.02}{Re}\log\left(\frac{\varepsilon}{3.7} + \frac{13}{Re}\right)\right)\right]$	$Re = 4000 - 10^8$ $\epsilon = 0.00004 - 0.05$ mm
Churchill	$f = \left[\left(\frac{8}{Re}\right)^{12} + \frac{1}{(A+B)^{3/2}}\right]^{1/12}$ $A = \left[2.457\log\frac{1}{(7/Re)^{0.9}+0.27\epsilon/D}\right]^{16}$ $B = \left(\frac{37530}{Re}\right)^{16}$	$Re =$ unspecified range $\epsilon = 0.001 - 0.01$ mm

Table 2: Friction factor equations [19]

The friction factor is derived by an equivalent sand-grain roughness, as developed by Nikuradse. Roughness measurements were conducted, given in the Appendix F. For this research, roughness measurements were performed of the pipes examined. The raw outputs are given in the appendix F, summed up in Table 3. A key difference between the roughness considered by the Colebrook-White equation is the sand-grain scale. The measurement gives four roughness measurement outputs, namely: R_a, R_z, R_q, R_t. Adams et. al. [20] conclude that R_z approximates the sand-grain roughness more accurately after conversion, i.e.,

$$\epsilon = 0.978 R_z. \tag{2.14}$$

The corresponding roughness R_z is converted into sand-grain roughness in Table 3.

Designation	Average R_z of samples (μm)	Sand-grain roughness ϵ (μm)
∅ 3.2	2.943	2.878
∅ 5	1.807	1.778
∅ 8	3.880	3.795

Table 3: Pipe roughness

2.4 Darcy-Weisbach

Friction factors are often employed in combination with the Darcy-Weisbach equation, commonly used in engineering practice to evaluate pressure losses. The Darcy-Weisbach equation for pressure loss is found from the steady momentum equation 2.8 when assuming:

- Constant velocity.
- An incompressible fluid.
- One-dimensional flow.
- Constant friction.
- No elevation (specific for this context).

Applying these assumptions yields the Darcy-Weisbach equation [21]:

$$\Delta p = f \frac{L}{D} \frac{1}{2} \rho u^2 \tag{2.15}$$

A closer look at the definition of Darcy-Weisbach reveals the presence of dynamic pressure ($\frac{1}{2}\rho u^2$), which is scaled by the physical properties of the pipe (f, L, D). As the Darcy-Weisbach equation considers an incompressible fluid without changes in its velocity, we can conclude that the Δp indicated by Darcy-Weisbach is, in fact, a loss of total pressure.

2.5 The Weymouth and Panhandle equations

An alternative approach to the Darcy-Weisbach equation is the Weymouth equation, often employed for compressible flows [21]. The Weymouth and Panhandle equations come from a family of equations developed for the oil and gas industry, whereas the Weymouth and Panhandle equations were specifically developed for natural gasses. The Weymouth and Panhandle equations contain several correction factors and model-specific constants, but their general form is found from the steady-momentum equation when assuming [22]:

- Real gases, with a constant compressibility factor Z and ratio of specific heats γ.
- Isothermal flow.
- One-dimensional flow.
- No change in elevation (specific for this context).

The general expression for these equations is [22]:

$$Q = a_1 \eta \left(\frac{T_{\text{sc}}}{p_{\text{sc}}} \right)^{a_2} \left[\frac{p_1^2 - p_2^2}{TZL} \right]^{a_3} \left(\frac{1}{\gamma_{\text{g}}} \right)^{a_4} D^{a_5} \tag{2.16}$$

where Q is the volumetric flow rate, η is the efficiency factor, $T_{sc} = 288.15$ K, is the temperature at standard conditions and $p_{sc} = 101325$ Pa, is the pressure at standard conditions, g_c is the specific gravity. For no elevation changes $\Delta z = 0$:

The coefficients to form the Weymouth and Panhandle equations are given in Table 4.

Equation	a_1	a_2	a_3	a_4	a_5
Weymouth	137.19	1	0.5	0.5	2.667
Panhandle	157.92	1.0788	0.5394	0.4604	2.6182

Table 4: Coefficients for the Weymouth and Panhandle equation [22]

To compute the outlet pressure, p_2, this equation is rewritten to:

$$p_2 = \sqrt{p_1^2 - \left(\frac{Q}{a_1 \eta \left(\frac{T_{\mathrm{sc}}}{p_{\mathrm{sc}}}\right)^{a_2} \left(\frac{1}{\gamma_{\mathrm{g}}}\right)^{a_4} D^{a_5}} \right)^{\frac{1}{a_3}} TZL} \tag{2.17}$$

The presence of the root invokes the possibility of negative and positive results, but negative pressures will never occur in reality, therefore, only positive pressures are accepted as feasible results from this calculation. Some combinations of inlet pressure p_1 and volume flow rate Q can result in a negative argument in the square-root. Cases where a negative argument occurs will be treated in more detail in Section 5.

2.6 The isentropic flow relations

Steady one-dimensional flows where friction, heat conductivity, and gravity are negligible can be analysed using isentropic flow equations. In such flows, total quantities such as total pressure (p_0), total temperature (T_0), and total density (ρ_0) remain constant along a streamline, a property known as streamline invariance [23]. Under these assumptions, and by applying the continuity, momentum and energy equations alongside the ideal gas law, the isentropic flow equations can be derived. The isentropic flow equations are as follows:

$$\frac{p}{p_0} = (1 + \frac{\gamma - 1}{2} M^2)^{-\frac{\gamma}{\gamma - 1}} \tag{2.18}$$

$$\frac{T}{T_0} = (1 + \frac{\gamma - 1}{2} M^2)^{-1} \tag{2.19}$$

$$\frac{\rho}{\rho_0} = (1 + \frac{\gamma - 1}{2} M^2)^{-\frac{1}{\gamma - 1}} \tag{2.20}$$

where p_0, T_0, and ρ_0 are the total pressure, temperature, density, respectively, γ is the ratio of specific heats and M is the Mach number. The left-hand sides of equations 2.18, 2.19, 2.20 gives the static to total ratio's, which can be evaluated at any point along a streamline. The ratios tend to a minimum for the flow approaching $M \to 1$. The flow achieves a critical-condition when $M = 1$, and the isentropic flow equations reduce to:

$$\frac{p^*}{p_0} = \left(\frac{2}{\gamma + 1} \right)^{\frac{\gamma}{\gamma - 1}} \tag{2.21}$$

$$\frac{T^*}{T_0} = \frac{2}{\gamma + 1} \tag{2.22}$$

$$\frac{\rho^*}{\rho_0} = \left(\frac{2}{\gamma + 1} \right)^{\frac{1}{\gamma - 1}} \tag{2.23}$$

where the starred conditions denote the critical conditions. An important observation from these equations is that these functions become purely dependent on γ, a useful property of critical conditions.
The ratios of previous equations can be evaluated at any point of a streamline, even if there has been a change in total quantities. If we enforce that total quantities remain constant, the static ratios are found between two points along a streamline:

$$\frac{p_2}{p_1} = \left(\frac{2 + (\gamma - 1) M_1^2}{2 + (\gamma - 1) M_2^2} \right)^{\frac{\gamma}{\gamma - 1}} \tag{2.24}$$

$$\frac{T_2}{T_1} = \frac{2 + (\gamma - 1) M_1^2}{2 + (\gamma - 1) M_2^2} \tag{2.25}$$

$$\frac{\rho_2}{\rho_1} = \left(\frac{2 + (\gamma - 1)\, M_1^2}{2 + (\gamma - 1)\, M_2^2}\right)^{\frac{1}{\gamma - 1}} \tag{2.26}$$

2.7 Fanno flow

Fanno flows refer to steady, one-dimensional flows of a compressible fluid experiencing frictional effects. These flows are assumed to be adiabatic (not isentropic), with constant-area flow passages and perfect gas properties. The flow is subject to frictional losses, which affect the flow characteristics, such as pressure, temperature, and velocity, along the length of a pipe [24]. The Fanno flow relation is given by:

$$\frac{fL^*}{D} = \frac{1 - M^2}{\gamma M^2} + \frac{\gamma + 1}{2\gamma} \ln\left(\frac{(\gamma + 1)M^2}{2 + (\gamma + 1)M^2}\right) \tag{2.27}$$

The working principle of this equation is as follows: In Figure 4, flow with Mach number M and ratio of specific heats γ enters the pipe. After travelling through the pipe, experiencing the wall friction factor f, the flow exits the pipe with the mach number $M + dM$. If the length was long enough for the flow to reach the critical point, $x = L^*$.

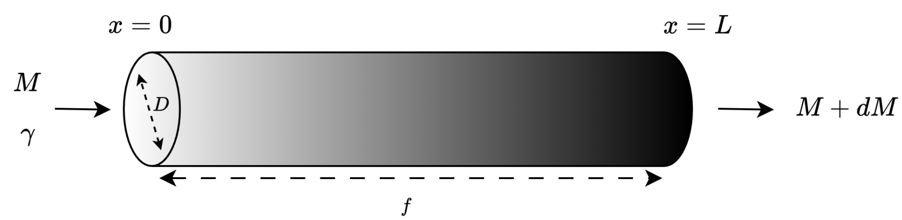

Figure 4: Fanno flow through a tube

To relate pressure, temperature, and density to the Fanno flow equation, a similar derivation must be performed. As Fanno flow itself assumes non-isentropic flow, these equations do not rely on total conditions, but on critical conditions. These equations are referred to as the Fanno property relations [24]:

$$\frac{p}{p^*} = \frac{1}{M}\sqrt{\frac{\gamma + 1}{2 + (\gamma - 1)M^2}} \tag{2.28}$$

$$\frac{T}{T^*} = \frac{\gamma + 1}{2 + (\gamma - 1)M^2} \tag{2.29}$$

$$\frac{u}{u^*} = \frac{\rho^*}{\rho} = M\sqrt{\frac{\gamma + 1}{2 + (\gamma - 1)M^2}} \tag{2.30}$$

The outlet conditions can be computed using these equations by using another ideal gas property. As γ remains constant, the critical conditions p^*, T^*, and ρ^* also remain constant. Therefore, the latter can be rewritten to:

$$\frac{p_2}{p_1} = \frac{M_1}{M_2}\sqrt{\frac{2 + (\gamma - 1)M_1^2}{2 + (\gamma - 1)M_2^2}} \tag{2.31}$$

$$\frac{T_2}{T_1} = \frac{2 + (\gamma - 1)M_1^2}{2 + (\gamma - 1)M_2^2} \tag{2.32}$$

$$\frac{\rho_2}{\rho_1} = \frac{M_1}{M_2}\sqrt{\frac{2 + (\gamma - 1)M_1^2}{2 + (\gamma - 1)M_2^2}} \tag{2.33}$$

Thus, the Fanno relation (Eq. 2.27) can be used to determine the outlet conditions of a pipe by substituting the predicted exit Mach number M_2 into equations 2.31, 2.32, and 2.33.
The isentropic flow and Fanno relations rely on ideal-gas properties. However, in some cases, like non-ideal gases, it might be necessary to resort to a different equation of state, discussed next.

2.8 Equation of State (EOS)

The operating window described in Figure 2 suggests a word of caution with regard to the use of the ideal gas law, viz.,

$$p = \rho R T \tag{2.34}$$

In other words, under high pressure conditions, gaseous hydrogen can deviate significantly from the ideal-gas law [25]. To get an impression of the deviations, observe the virial EOS 2.35:

$$Z = \frac{PV}{nRT} = 1 + \rho^2 B(T) + \rho^2 C(T) + \rho^3 D(T) + ... \tag{2.35}$$

The compressibility factor (Z) represents the difference between the left and right sides of equation 2.34, thus indicating the deviation. The virial coefficients, i.e. $B(T)$, $C(T)$, etc., are found experimentally. SAE J2601 refers to the Leachman EOS for hydrogen [26]. Leachman's EOS is a Helmholtz free energy equation, which may not be convenient for direct computations in this text. Furthermore, Lemmon et. al. presented a more convenient equation which is based on the virial series [27]:

$$Z(p,T) = \frac{p}{\rho R T} = 1 + \sum_{i=1}^{9} a_i \left(\frac{100\text{ K}}{T}\right)^{b_i} \left(\frac{p}{1\text{ MPa}}\right)^{c_i} \tag{2.36}$$

The constants for a_i, b_i, c_i are given in Table 5. Lemmon's EOS is plotted in Figure 5. In contrast, the ideal-gas law ($Z = 1$) shows at low pressures little deviation from Lemmon's EOS.

i	a_i	b_i	c_i
1	0.058 884 60	1.325	1.0
2	-0.061 361 11	1.87	1.0
3	-0.002 650 473	2.5	2.0
4	0.002 731 125	2.8	2.0
5	0.001 802 374	2.938	2.42
6	-0.001 150 707	3.14	2.63
7	0.958 852 8 × 10^{-4}	3.37	3.0
8	-0.110 904 0 × 10^{-6}	3.75	4.0
9	0.126 440 3 × 10^{-9}	4.0	5.0

Table 5: NIST EOS constants [27]

Although it may not be as precise, the Soave-Redlich Kwong (SRK) EOS offers a more practical option for hand calculations as the NIST EOS becomes rather lengthy due to its summation term. For moderate pressures, the SRK EOS captures the essential characteristics of gaseous hydrogen [28]. The SRK EOS is essentially a modification of the original Redlich-Kwong (RK) EOS, which is also a viable option for gaseous hydrogen [9][12]. In fact, the RK EOS approximates the NIST EOS better at moderate pressures [9]. That being said, the SRK EoS EOS better available in relevant literature and CFD-packages. For relevance, we focus on the SRK EOS. The SRK EOS is as follows [29]:

$$p(T,\nu) = \frac{RT}{\nu - b} - \frac{\alpha a^2(T)}{\nu(\nu + b)} \tag{2.37}$$

with

$$a = 0.42748\frac{R^2T_c^2}{p_c^2} \tag{2.38}$$

$$b = 0.08664\frac{RT_c}{p_c} \tag{2.39}$$

$$\alpha(T) = 1 + m\left(1 - \sqrt{\frac{T}{T_c}}\right) \tag{2.40}$$

$$m = 0.480 + 1.574\omega - 0.176\omega^2 \tag{2.41}$$

where a and b are constants derived from the critical state parameters p_c and T_c of hydrogen, ν is the molar volume, and ω is the accentric factor. The critical state parameters of hydrogen are given in Table 6.

p_c (Pa)	T_c (K)	ω
12.964e5	33.145	-0.219

Table 6: Critical state parameters of hydrogen

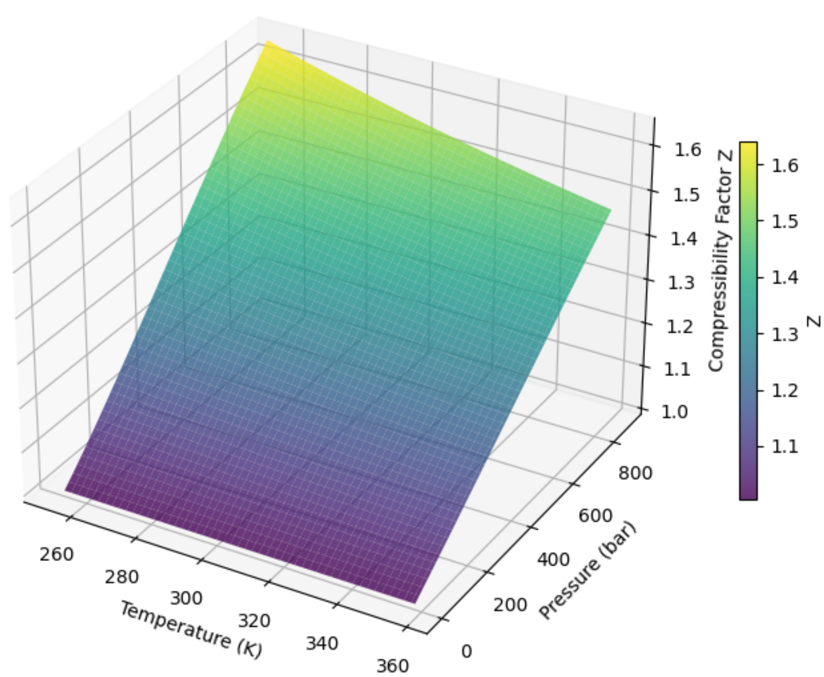

Figure 5: Lemmon's EOS compared to the ideal gas law ($Z = 1$)

2.9 Real gas effects and the isentropic flow equations

The isentropic flow equations provided so far are derived under the assumption of an ideal gas. By introducing two adjusted expressions for the isentropic exponents [30]:

$$\gamma_{T\nu} = 1 + \frac{\nu}{c_v} \left(\frac{\partial p}{\partial T} \right)_\nu \tag{2.42}$$

$$\gamma_{p\nu} = -\frac{\nu}{p} \frac{c_p}{c_v} \left(\frac{\partial p}{\partial \nu} \right)_T \tag{2.43}$$

where ν is the molar volume, and c_v is the specific heat at constant volume. Working out the derivatives $\left(\frac{\partial p}{\partial T}\right)_\nu$ and $\left(\frac{\partial p}{\partial \nu}\right)_T$ from the SRK EOS (Eq. 2.37) [28]:

$$\left(\frac{\partial P}{\partial \nu} \right)_T = -\frac{RT}{(\nu - b)^2} + \frac{a\alpha^2}{\nu(\nu + b)} \left(\frac{1}{\nu} + \frac{1}{\nu + b} \right) \tag{2.44}$$

$$\left(\frac{\partial P}{\partial \nu} \right)_T = -\frac{RT}{(\nu - b)^2} + \frac{a\alpha^2}{\nu(\nu + b)} \left(\frac{1}{\nu} + \frac{1}{\nu + b} \right) \tag{2.45}$$

The isentropic exponents γ_{T_ν} and $\gamma_{p\nu}$ are subsequently applied in the isentropic flow equations 2.18, 2.19 and 2.20, resulting in:

$$\frac{p_1}{p_2} = \left(\frac{2 + (\gamma_{p\nu} + 1)\, M_1^2}{2 + (\gamma_{p\nu} + 1)\, M_2^2} \right)^{\frac{-\gamma_{p\nu}}{\gamma_{p\nu} - 1}} \tag{2.46}$$

$$\frac{T_1}{T_2} = \left(\frac{2 + (\gamma_{p\nu} + 1)\, M_1^2}{2 + (\gamma_{p\nu} + 1)\, M_2^2} \right)^{\frac{\gamma_{T\nu} - 1}{\gamma_{p\nu} - 1}} \tag{2.47}$$

$$\frac{\rho_1}{\rho_2} = \left(\frac{2 + (\gamma_{p\nu} + 1)\, M_1^2}{2 + (\gamma_{p\nu} + 1)\, M_2^2} \right)^{\frac{-1}{\gamma_{p\nu} - 1}} \tag{2.48}$$

Thus, by incorporating a dependence on molar volume and temperature, equations 2.46, 2.47, and 2.48 can offer a better approximation in non-ideal gas cases.

3 Numerical Modelling

A major limitation of the models presented so far is their dependence on flow simplifications. For instance, the isentropic flow equations assume that the total properties such as total pressure and total temperature remain constant along a streamline.
However, when frictional or other non-ideal effects become dominant, these assumptions break down, possibly leading to inaccurate predictions, thereby losing their validity. In such cases a different modelling approach is required where numerical methods over an outcome. In turn, these numerical methods are employed in CFD.
This section discusses the procedure and options for setting up a CFD case for gaseous hydrogen flowing through a ∅ 5 mm pipe, investigating viable options in open-source CFD packages.
Open-source CFD packages are easily accessible today and show promising potential. CFD codes are developed for specific purposes and can involve simplifications as well. Therefore, a good impression of their working principles and governing equations is necessary to provide an accurate assessment from their results.
The following topics, in order of building a CFD case, are discussed next:

1. Meshing: The construction of a computational grid in the geometry considered.

2. Selection of a turbulence model: A wide variety of turbulence models exits, each having their individual advantages.

3. Numerical solution methods: CFD codes consist of numerous sets of equations, e.g., the continuity, momentum, and energy equations. There are multiple options available to solve these equations on the numerical grid.

These items are treated in the following subsections, starting with the construction of a computational grid.

3.1 Meshing

A flow simulation is carried out on a computational grid, often called the mesh. In the process of creating a mesh, or *meshing*, careful consideration of the properties of the flow, the desired quality, and the computational expense is required. In case of this research, the pipes can be meshed in various ways. This subsection covers the basic performance metrics of a mesh and the available options to model pipe flows.
As often stated in CFD practice: 'Good mesh - good results'. A geometry can be fitted with a structured and unstructered mesh, referring to the way grid lines are constructed. A structured mesh consists of cells that are organised in a predictable pattern, e.g. squares on graph paper or bricks on a wall. Each cell has a fixed number of neighbours, and the connectivity between cells can be described using a regular grid of indices. Structured meshes can be used on simple geometries and have a computational advantage, as will be shown later. Typical cell types for structured grids include quadrilateral or hexahedra cells. An unstructured mesh is made up of cells that are arranged irregularly, without a predictable grid pattern. These types of meshes become particularly useful when faced with complex geometries where a structured pattern just cannot be fitted properly. Typical cell types for unstructured meshes include tetrahedra, hexahedra, pyramids, or polyhedra.

3.1.1 Mesh performance metrics

In the process of fitting a mesh to a geometry, the individual cells can undergo some deformation to properly connect them. The following metrics are evaluated to assess mesh quality:

- Skewness: The mesh is fitted to a geometry, which involves some deformation for cells to properly connect them. Viewing a square, pulling its sides leads to *skewness*, whereas the faces that interconnect between cells gain orientation with respect to a cell centre. Drawing a perpendicular line from a cell face, a perfect cell would have this line intersect with its centre. When a cell becomes *skewed*, this perpendicular line lies far off the cell centre.

- Non-orthogonality: When a mesh is adapted to complex geometries, cells often undergo deformation to maintain topological connectivity and fit curved or irregular surfaces. This deformation affects several key mesh quality metrics.
- Aspect ratio: The aspect ratio refers to the ratio of the longest to the shortest dimension of a cell; ideally, this should be close to one, but in stretched regions, such as inflation layers, high aspect ratios are commonly encountered.
- Growth ratio: As neighbouring cells sometimes differ in size, their volume also differs. Here, large differences between neighbouring cells can lead to unwanted numerical damping.

Each of these metrics is desired to optimise in the construction of a mesh. In the context of this text, a straight $\varnothing 5$ pipe flow can be meshed in various ways. To name a few:

- Radial: Radial meshes are perhaps the simplest and most straightforward approach. The cross-section of a pipe is divided by lines travelling perpendicular from its walls to the pipe centre, like slices of a pizza. These individual slices are refined by several concentric circles placed around the center of the pipe. This structure repeats over the length of the pipe, thereby slicing the pipe.

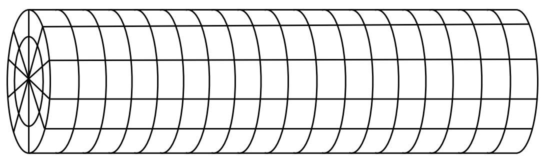

Figure 6: radial-grid mesh

- OH-grid: An OH-grid mesh approaches the cross-section differently. In the cross-section, a square shape is placed around the cell centre. The outer portions of the pipes are subdivided into 4 major regions, bound by lines travelling from edges of the square perpendicular to the pipe wall. The length of these meshes are the same as a radial mesh.

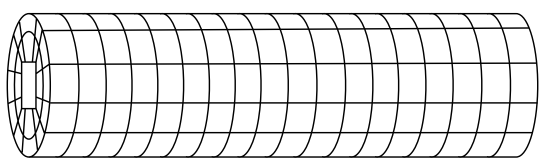

Figure 7: OH-grid mesh

- Hybrid approaches: In hybrid approaches, a large portion of the inner pipe volume is fitted with unstructured elements. The outer parts are fitted with structured elements.

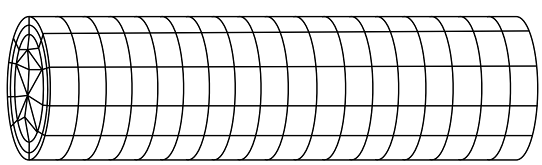

Figure 8: hybrid-grid mesh

To properly assess wall friction, inflation layers were constructed to assess the boundary layer. As this is a significant design aspect of meshes, an overview of boundary layer principles is given next.

3.1.2 Boundary layers

Wall bounded flows can be divided into different regions, as shown in Figure 9.

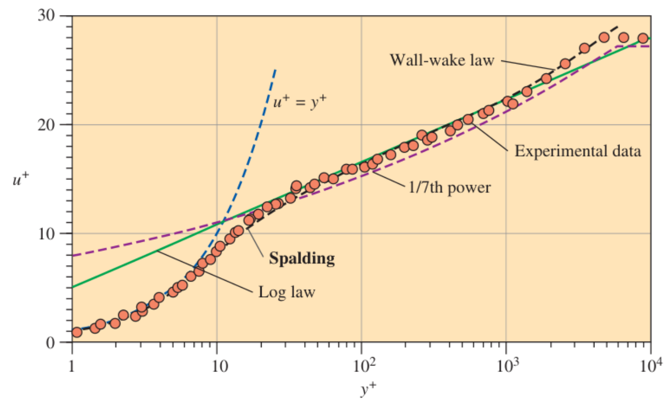

Figure 9: The viscous boundary layer regions [24]

The turbulence models presented later often require a certain y^+, thereby imposing a design criteria on the computational grid. In this figure, the velocity and distance from the wall are non-dimensionalised with the law of the variables, viz. [31],

$$y^+ = \frac{yu_*}{\nu} \quad u^+ = \frac{u}{u_*} \tag{3.1}$$

Here, u_* represents the friction velocity, defined as:

$$u_* = \sqrt{\frac{\tau_w}{\rho}} \tag{3.2}$$

Flows that experience significant interaction with their boundary layer require proper modelling, starting with a proper mesh. The mesh is therefore designed to contain inflation layers, which are thin layers that reside around or in the viscous boundary layer. Turbulence models impose specific requirements on the design criteria for these inflation layers.

3.2 Turbulence models

Flows that experience sufficiently high disturbances and Reynolds numbers can transition to turbulence. In such flows, eddies form, carrying kinetic energy (k), and transfer energy through a cascade from larger to smaller scales, dissipating their energy with rate ϵ. Turbulence is characterised by this eddying motion, which poses challenges for numerical modelling. In CFD, three primary approaches are reviewed in this text to handle turbulence: Reynolds-Averaged Navier–Stokes (RANS), Large Eddy Simulation (LES), and Direct Numerical Simulation (DNS). Starting by averaging the Navier-Stokes equations, the RANS and FANS models are found. These models essentially provide a complete modelling approach for the turbulent eddies, thus not computing them exactly. DNS and (partially) LES compute these eddies exact, so no (or little) modelling is involved in these approaches. In short, these methods differ in how they treat turbulent structures. As will be shown, a consequence of these different modelling approaches leads to significant differences in computational cost and accuracy.

3.2.1 RANS

An essential working principle of RANS is averaging. Here, the velocity is decomposed in an averaged and fluctuating part: $u = \bar{u} + u'$. If the conservation equations (2.1, 2.2) are treated with this averaging process, the governing RANS equations are found:

$$\rho \frac{\partial \bar{u}_i}{\partial t} + \rho \bar{u}_j \frac{\partial \bar{u}_i}{\partial x_j} = -\frac{\partial p}{\partial x_i} + \frac{\partial}{\partial x_j}\left(2\mu S_{ji} - \rho \overline{u'_j u'_i}\right) \tag{3.3}$$

The term $\rho \overline{u'_j u'_i}$ is the Reynolds stress tensor, which requires special treatment. The term $\overline{u'_j u'_i}$ is a time-averaged rate of momentum transfer due to turbulence. Essentially, the Reynolds stress tensor adds more unknowns to the system of equations, thereby requiring additional equations to close the system. This is the closure problem [32].

3.2.2 FANS

An alternative to Reynolds-Averaging is Favre-Averaging, particularly useful in steady compressible flows. The principle of Favre-averaging is again a decomposition of the velocity: $u = \tilde{u} + u''$, where u is the velocity, $\tilde{u}$ is the mass averaged velocity and u'' is the Favre fluctuation. When applying this to the Navier-Stokes equations, the Favre-Averaged Navier-Stokes equations are found:

$$\frac{\partial}{\partial t}(\bar{\rho}\bar{u}_i) + \frac{\partial}{\partial x_j}(\bar{\rho}\bar{u}_j\bar{u}_i) = -\frac{\partial p}{\partial x_i} + \frac{\partial}{\partial x_j}\left[\bar{t}_{ji} - \overline{\rho u''_j u''_i}\right] \tag{3.4}$$

The Favre Reynolds stress tensor appears in this equation as $\overline{\rho u''_j u''_i}$. Compared to its RANS counterpart, this Reynolds stress tensor is much less complicated as density fluctuations do not appear in product with velocity fluctuations. For a more detailed explanation, see Appendix D.
Several approaches exist to compute the Reynolds stress tensor. The most popular ones being the $k-\epsilon$, $k-\omega$ and $k-\omega$ SST models. A short overview of these models and their expected applicability is provided next.

3.2.3 $k-\epsilon$ model

A widely used turbulence model is the $k-\epsilon$ model. This is a two-equation model, which contains one equation for turbulence kinetic energy k [33], and one for the dissipation rate ϵ.
The $k-\epsilon$ turbulence model is a two-equation model widely used in CFD to simulate turbulent flows. Introduces two additional transport equations into the Navier–Stokes framework: one for turbulent kinetic energy k, and another for the turbulent dissipation rate ϵ. The kinetic energy k represents the energy contained in turbulent eddies, while ϵ characterises the rate at which this energy is dissipated into heat due to viscous effects. By solving these two coupled equations, the model provides an estimate of the turbulent viscosity, which is then used to close the RANS equations.
The standard $k-\epsilon$ model is known for its robustness, relatively low computational cost, and reasonable accuracy for a wide range of engineering flows, especially in high-Reynolds-number, fully turbulent regimes. However, it has limitations in predicting flows with strong pressure gradients, separation, or swirl.

3.2.4 $k-\omega$ model

The $k-\omega$ turbulence model is another widely used two-equation model in CFD to simulate turbulent flows. Like the $k-\epsilon$ model, it introduces two additional transport equations: one for the turbulent kinetic energy k, and one for the specific dissipation rate ω. The variable ω represents the rate of dissipation of k per unit turbulent kinetic energy and has dimensions of inverse time, offering a more direct control over turbulence frequency [34].
One of the key advantages of the $k-\omega$ model is its superior performance in near-wall regions, where it provides accurate predictions without the need for empirical damping functions. This makes it particularly effective for boundary layer flows and flows with adverse pressure gradients or separation. However, the model is sensitive to freestream values of ω, which can lead to inaccuracies away from walls.
To overcome this, the Shear Stress Transport (SST) $k-\omega$ model was developed. It blends the $k-\omega$ model near the wall with the $k-\epsilon$ model in the freestream, combining the strengths of both models and offering improved accuracy in a wide range of flow conditions.

3.2.5 Menter's Shear Stress Transport (SST) model

The Shear Stress Transport (SST) model, developed by Florian Menter[35], is an advanced turbulence model that combines the strengths of both the $k-\epsilon$ and $k-\omega$ models to improve accuracy and robustness in a wide range of flow scenarios. It was specifically designed to overcome the limitations of the standard $k-\omega$ model's sensitivity to freestream conditions and the $k-\epsilon$ model's inaccuracy in the near-wall region.
The SST model uses the formulation near walls, where it excels at capturing boundary layer behavior, and gradually transitions to the $k-\epsilon$ formulation in the far field, where it is less sensitive to the freestream turbulence quantities. This blending is controlled by a smooth function that switches the model behavior depending on the distance to the nearest wall.
One of the key innovations in Menter's SST model is the inclusion of a shear-stress limiter, which improves the prediction of adverse pressure gradients and flow separation. Traditional eddy viscosity models often overpredict the turbulent shear stress in these regions, leading to inaccurate separation behavior. By limiting the eddy viscosity based on the local shear stress, the SST model provides more realistic turbulence behavior and significantly better predictions for flows over airfoils, diffusers, and other geometries with complex separation phenomena.
The SST model is widely regarded as a reliable and relatively computationally efficient model for industrial applications, especially where wall-bounded turbulence and separation play a significant role.

3.2.6 Beyond Averaged Models: LES and DNS

The most computationally demanding of the approaches mentioned here is DNS. This model provides a transient three-dimensional solution to the Navier-Stokes and continuity equation. DNS can serve as a means to verify the approximations of other models, acting as an extra source of experimental data. DNS resolves the smallest eddies in a simulation in the order of the Kolmogorov length scale.

Kolmogorov scales

In the cascading process of eddies, the eddies eventually become so small that viscosity becomes dominant. At this size, the eddies dissipate to thermal energy, therefore being the smallest scale of turbulence. This scale is governed by the Kolmogorov scales:

$$\eta_k \sim \left(\frac{\nu^3}{\epsilon}\right)^{\frac{1}{4}}, \quad \tau_s \sim \left(\frac{\nu}{\epsilon}\right)^{\frac{1}{2}}, \quad v \sim (\nu\epsilon)^{\frac{1}{4}} \tag{3.5}$$

where η_k is the length scale, τ_s is the time scale, and v is the velocity scale.
To get an impression of the additional computational expense of DNS, a comparison is made in which the initial layer thickness is computed. As demonstrated in section 3.1.1, the initial layer thickness enforces the use of more layers to retain proper growth ratios. We therefore assume in this example that thinner initial layers require larger numerical grids.
Start by computing the initial layer thickness required for $k-\omega$ SST. The skin friction factor is given by:

$$C_f = [2\log(Re) - 0.65]^{-2.3} \tag{3.6}$$

the wall shear stress is then given by:

$$\tau_w = C_f \frac{1}{2} \rho u_{\text{freestream}}^2 \tag{3.7}$$

the friction velocity is found using equation 3.2. Combining these results, the initial layer thickness should then be:

$$y = \frac{y^+ \mu}{\rho u^*} \tag{3.8}$$

Here, y implies the layer thickness in order to properly resolve the viscous layer when using $k-\omega$ SST. Moving on to DNS simulations, which continue to resolve eddies towards the Kolmogorov scales, the smallest layer is computed with:

$$\eta = \left(\frac{\nu^3}{\epsilon}\right)^{\frac{1}{4}} \tag{3.9}$$

Unfortunately, this equation can only be solved when knowing ϵ, which is hard to guess since it depends on the velocity fluctuation u'. Other ways to accurately compute this require many insights into the flow; something that can be simply unknown in an early stage. A crude estimation of ϵ:

$$\epsilon = \frac{u^3_{\text{freestream}}}{D} \tag{3.10}$$

In many cases, a DNS simulation requires a much smaller layer thickness. For a three-dimensional case, and recalling volume ratio's, the same case would require many more cells and therefore impose much more computational load.

In Large-Eddy Simulations (LES), the need for a fine numerical grid—as required in DNS—is mitigated by modelling the smaller turbulent scales instead of resolving them directly. Henceforth, there is no longer a need to build the grid all the way towards the Kolmogorov length scale. These unresolved motions, known as subgrid-scale (SGS) eddies, are filtered out by the mesh, which only resolves the larger, energy-containing eddies. However, LES faces significant challenges near walls, where all turbulent structures become small and the range of eddy sizes narrows. In these regions, the resolved and subgrid scales begin to overlap, making accurate modelling more difficult.

3.3 Numerical Solution Methods

The CFD codes considered in this text employ the Finite Volume Method (FVM). In this approach, the computational domain is divided into a finite number of control volumes and the governing equations are applied directly to each volume. The governing equations are, in turn, treated by a solver, either segregated or coupled.
A choice between these strategies is driven by pressure-velocity coupling. At high flow speeds, this coupling is said to be strongly connected, while at lower speeds, this becomes segregated [36].
Segregated solvers employ algorithms to couple pressure and velocity. The essential steps in the following segregated methods involve solving the momentum and continuity equations iteratively by introducing a pressure correction equation. This results in a Poisson equation — an elliptic partial differential equation for pressure — which ensures mass conservation by enforcing the divergence-free condition on the velocity field. These methods are powerful for incompressible flows, but require some adjustments to include changes in density. This is mostly overcome using the energy equation and an EOS.
The general procedure is:

1. Estimate the velocity field, either from an initial condition or by solving the momentum equation using a guessed pressure field. This velocity field typically does not satisfy the continuity equation.

2. Compute the advective and viscous terms based on the current velocity field. These terms are used to update the momentum balance.

3. Solve a Poisson equation for pressure correction. This equation is derived from combining the momentum and continuity equations, and ensures that the corrected velocity field will satisfy mass conservation.

4. Correct the velocity field using the newly computed pressure field. This step adjusts the velocity to become divergence-free, thereby satisfying the continuity equation.

5. The corrected velocity field, however, is now no longer consistent with the original momentum equation, since it was derived using an earlier pressure guess. The process must therefore be repeated until both momentum and continuity equations are satisfied within a given tolerance.

3.3.1 SIMPLE

The SIMPLE algorithm, developed by Patankar and Spalding [37], is one of the most widely used segregated solvers for incompressible steady state flow. It follows the general structure above, but introduces two key techniques:

- Pressure correction: Instead of solving for absolute pressure, SIMPLE solves a pressure correction equation that adjusts the guessed pressure field iteratively to drive the velocity field toward mass conservation.
- Under-relaxation: Since the momentum and pressure equations are only loosely coupled, SIMPLE employs under-relaxation factors to stabilize convergence. Without these, the iterative scheme may diverge due to the artificial time lag between updated fields.

SIMPLE is robust for steady-state simulations, especially in incompressible flows where pressure does not enter through an equation of state. However, its convergence can be slow for strongly coupled or transient problems.

3.3.2 PISO

The PISO algorithm, introduced by Issa in 1986 [38], is a segregated algorithm designed for transient (time-dependent) flow problems. It improves upon SIMPLE by addressing its limited pressure–velocity coupling within each time step.
While SIMPLE relies on outer iterations across time steps, PISO performs multiple pressure corrections within a single time step. This tighter coupling enhances stability and convergence for unsteady flows, especially when using large time steps.
The typical steps in PISO are:

1. Predict the velocity field by solving the momentum equation using the known pressure field from the previous time step.
2. First pressure correction: Solve the pressure Poisson equation to correct pressure and make the velocity field divergence-fee.
3. Correct the velocity using the new pressure.
4. Additional corrector steps (usually 1 or 2): Repeat the pressure correction and velocity update to better satisfy both momentum and continuity equations.

Unlike SIMPLE, no under-relaxation is typically needed in PISO due to the multiple corrector steps within each time level. This makes PISO particularly effective in simulations involving:

- Rapid transients
- Moving boundaries
- Strong pressure-velocity interactions

However, PISO is less efficient for steady-state cases, as it lacks the steady under-relaxation and outer-loop structure found in SIMPLE. For such cases, a hybrid approach like PIMPLE is preferred.

3.3.3 PIMPLE

The PIMPLE algorithm is a hybrid approach that combines features of both SIMPLE and PISO. It is particularly useful for transient simulations where stability and convergence need to be balanced, such as in compressible or turbulent flows.
PIMPLE is essentially a PISO loop embedded within a SIMPLE-like outer iteration. This allows it to:

- Perform multiple pressure–velocity corrector steps per time step (like PISO),
- While also including outer corrector loops (like SIMPLE) for increased robustness and under-relaxation control.
- Handle large time steps more stably than PISO
- Support convergence acceleration via under-relazation (unlike pure PISO)
- Perform well in both steady and transient simulations

In OpenFOAM, the number of outer correctors (the SIMPLE-like loop) and inner correctors (the PISO-like pressure corrections) are both user-defined, giving fine-grained control over the trade-off between computational cost and convergence stability.
PIMPLE is commonly used in solvers such as rhoPimpleFoam for compressible flows, where strong coupling between pressure, density, and velocity demands a more robust strategy than SIMPLE or PISO alone.

rhoPimpleFoam

Including density variations requires minor alterations to the already discussed PIMPLE algorithm. The major additions include the energy equation and an equation of state. The steps are as follows [39, 40]:

1. Momentum equation (predictor step): Solve the momentum equation for velocity $\mathbf{U}$ using the current pressure field.
2. Solve the energy equation for internal energy e: This provides updated thermodynamic information for temperature and pressure.
3. Solve the pressure equation: A Poisson-like equation is solved to enforce mass conservation by correcting pressure.
4. Correct the velocity field: Use the corrected pressure gradient to update the velocity field, ensuring continuity.
5. Update density: Recalculate density using the equation of state, based on updated pressure and temperature.

   Steps 2–4 form a PISO-like inner corrector loop.
6. Solve the energy equation for temperature: Using the latest internal energy and pressure, update the temperature field.
7. Update turbulence models, e.g., k–ω SST: Recalculate turbulence quantities based on the latest flow field.

   Steps 1–7 are repeated as part of the outer corrector loop until a specified number of iterations or convergence tolerance is met.

3.3.4 Coupled

Although segregated algorithms like SIMPLE and PISO are computationally efficient, they can become unstable or converge slowly in flows with strong compressibility effects. This is because pressure, density and temperature become tightly coupled through the equation of state, and iterative decoupling struggles to resolve these strong interactions efficiently. In contrast, a coupled solver solves the full set of governing equations simultaneously. This leads to a large matrix system, with pressure, velocity, temperature, and density coupled together. This approach is more computationally expensive as the this resulting matrix is much larger and more complex, requiring more memory and computational effort.

4 Experimental setup

An in-house developed experimental setup was used to collect validation data. A range of pipe diameters is subject to a range of mass flow rates. In addition, pressure and temperature measurements were performed at various locations throughout the setup. The setup was envisioned with the ISA 75.01 standard. The standard is intended for control valve testing; henceforth, slight modifications were made to accommodate pipe flow measurements. That is, the placement of equipment downstream of the test subjects was minimised to prevent disturbances. A schematic overview of the test setup is given in Figures 10 and 11. The flow path in the test configuration is as follows: Gaseous hydrogen flows from a large storage vessel through a pressure regulator, as shown in Figure 10. Here, the mass flow rate is monitored and manipulated with a pressure regulator. The flow then passes through a mass flow sensor, a thermocouple, and a pressure sensor. Thereby obtaining the mass flow rate ($\dot{m}$), pressure p_1, and temperature T_1.

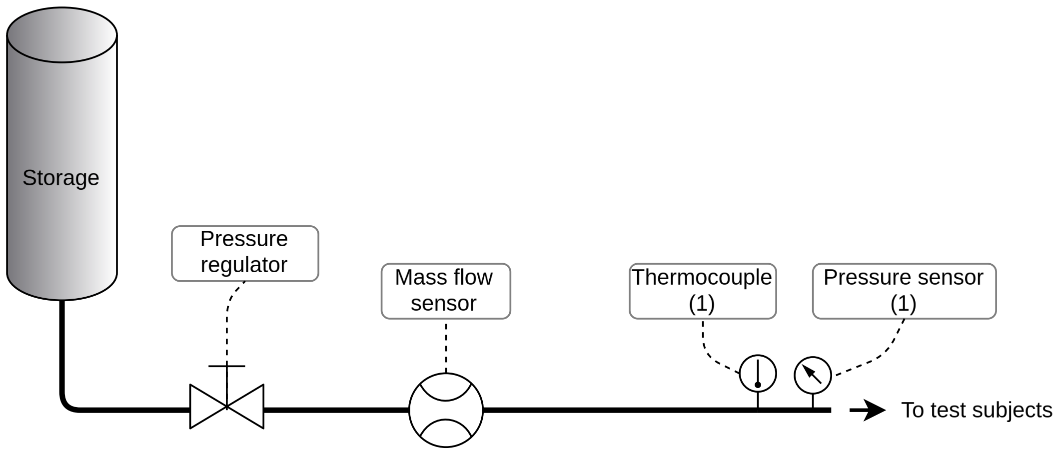

Figure 10: Test setup: supply line from storage to test subjects

After transport through the supply line, gaseous hydrogen reaches the test subjects as shown in Figure 11. For $\varnothing 5$ and $\varnothing 3.2$ pipes, pressure and temperature measurements are taken directly on the pipes, providing the inlet conditions p_2, T_2 and the outlet conditions p_3, T_3.

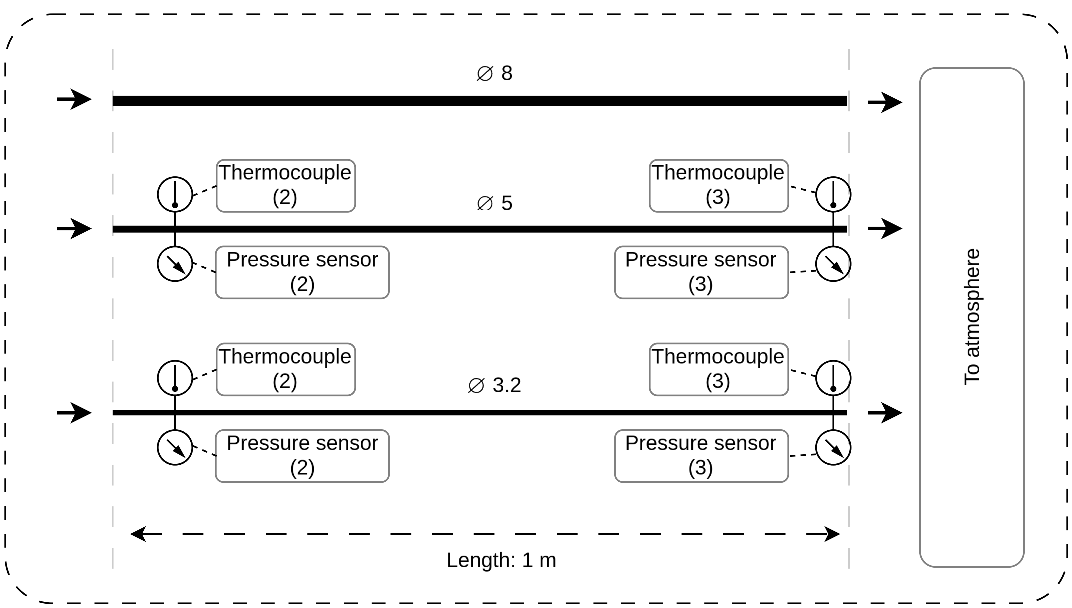

Figure 11: Test setup: test subjects to atmosphere

The full experimental setup is shown in Figure 12. The flow enters on the right hand side and exits on the left hand side. The part descriptions are given in Table 7

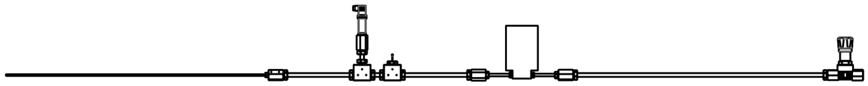

Figure 12: Technical drawing of test line

A close-up of the inlet section of the test setup is shown in Figure 13. The storage vessels are connected to the experimental setup via a flexible hose. From there, the hydrogen first passes through an adapter fitting that connects to the pressure regulator. The flow then continues through another adapter into a 1-meter-long pipe with an 8 mm diameter.
Next, it flows through a reducer fitting into a 10 cm long pipe with a 5 mm diameter, leading into the Coriolis mass flow meter. After the flow meter, the hydrogen exits through another 10 cm, 5 mm diameter pipe into an adapter fitting that connects to a 30 cm long, 8 mm diameter pipe.
This section includes temperature and pressure sensor bushings placed sequentially, with a 10 cm long, 8 mm diameter pipe between them. Finally, the flow continues through another 8 mm diameter pipe to the final adapter fitting, which leads into the test subjects.

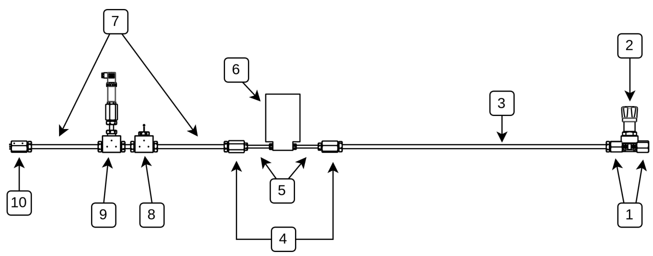

Figure 13: Close up from the supply line

To fascilitate a connection between the 8 mm piping and test subjects, a screw in fitting was connected to the adapter fitting, as shown in Figure 14.

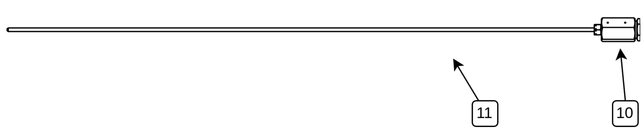

Figure 14: Close up from the test subjects and the reducer fitting

A schematic of the measurement locations is given in Figure 15.

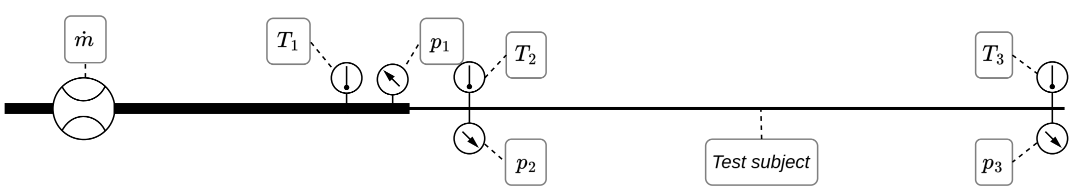

Figure 15: Test line including measurement locations

Item no.	Component Description
1	Adapter fittings
2	Pressure regulator
3	1 meter long 8 mm diameter pipe
4	Adapter fittings 8 mm to 5 mm diameter
5	20 cm long 5 mm pipes
6	Coriolis Mass Flow Meter - Rheonik RHM 03
7	30 cm long 8 mm diameter pipe
8	Thermocouple with housing
9	Pressure transmitter with housing
10	Adapter fitting
11	Test subject(s)

Table 7: Experimental setup components

Reducer fittings were placed for test subjects ∅ 5 and ∅ 3.2 as the upstream pipe was chosen to have an 8 mm diameter to minimise flow disturbance. The T2 test subjects were equipped with thermocouples and pressure sensors. Measurements were performed without and with the sensors to observe and minimise the flow disturbance by the sensors. The parts specifications are given in Table 7.

Designation	Internal diameter [mm]	Length $\pm 0.5mm$ [m]	Average roughness [μm]
∅ 3.2	3.2	0.997	0.5
∅ 5	5	0.995	0.4
∅ 8	8	0.970	1.2

Table 8: Test subjects

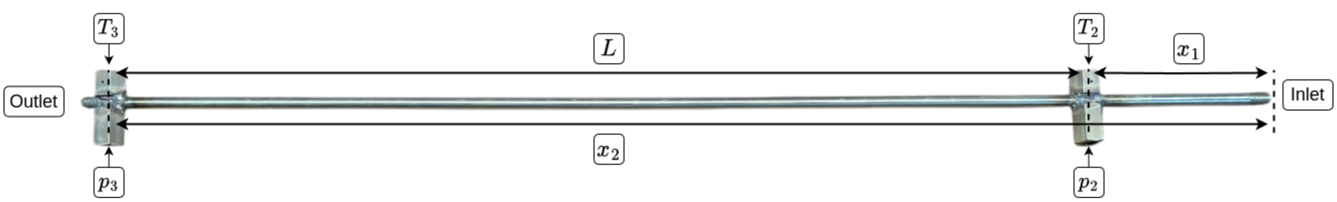

Figure 16: Measurement locations for 3.2 and 5 mm pipes

As shown in Figure 16, sockets were welded perpendicular to the pipe, The locations of these sockets are provided in Table 9:

Test subject	x_1	x_2	L
5 mm	0.150	0.972	0.822
3.2 mm	0.150	0.974	0.824

Table 9: Socket locations on 5 and 3.2 mm pipes

Instrument	Type	Fidelity	
Thermocouple(s)	Type-J	Tolerance of 0.4% of T, max. ± 1.5 K	
Pressure sensor(s)	1 MPa	Tolerance of ± 2.5 kPa	
Coriolis mass flow-meter	Rheonik RHM03	Flow-rate range $\frac{\text{g}}{\text{s}}$	Uncertainty %
		0 - 1.6	± 1.5
		1.6 - 3.3	± 0.6
		3.3 - 10.0	± 0.2

Table 10: Measurement equipment

4.1 Standardization of measurement values

Each instrument introduces a unique uncertainty into the measurement. The instrument uncertainty is derived from the manufacturer's specification. The thermocouples used in this setup were specified with a tolerance based on measured quantity, the pressure sensors were specified with a fixed tolerance, and the mass flow-rate sensor was specified with an uncertainty based on the measured rate. The latter are converted to a standard uncertainty. Standard uncertainties from tolerance-based instruments are treated with a rectangular distribution, viz. [41],

$$u = \frac{\text{tolerance}}{\sqrt{3}} \tag{4.1}$$

Uncertainties that vary with the measured quantity or rate are derived from the mean sample value over the measured period. The uncertainties from measurements are derived from the standard deviation of samples, i.e.,

$$u_{\text{test}} = \frac{\text{SD}}{\sqrt{N}} \tag{4.2}$$

where N denotes the number of samples, and SD the standard deviation. A combined uncertainty is derived from the instrument uncertainty u_{inst} and measurement uncertainty u_{test} for each experiment:

$$u_{\text{c}} = \sqrt{u_{\text{inst}}^2 + u_{\text{test}}^2}. \tag{4.3}$$

Finally, the expanded uncertainty is computed with

$$U = k u_{\text{c}} \tag{4.4}$$

where $k = 2$ to provide a confidence interval of 95%. The mean value of the measurement samples is presented along with an expanded uncertainty, presented in the format: (<mean value> ± <expanded uncertainty value>). The reported measurements are presented with a number of significant digits such that the final digit aligns with the least significant digit of the uncertainty, which is provided with two significant digits. In instances where there is a difference of two orders of magnitude between the uncertainties u_{inst} and u_{test}, the smallest uncertainty is neglected.

4.2 Optical Flow Visualisation

Gaseous hydrogen is a transparent, odourless, and tasteless gas. The only direct way to indicate its presence is inevitably the large noise production during a high pressure release. In addition to the latter being a challenge to safety principles, hydrogen and ambient air experience a large difference between density under normal conditions, where gaseous hydrogen is fourteen times lighter than air. Thereby, its buoyancy causes hydrogen to escape very rapidly, in turn being a favourable property in terms of safety.
Yet, this large difference between hydrogen and air allows for the visualisation of flow structures. Considering Gladstone - Dale's equation:

$$n - 1 = K\rho \tag{4.5}$$

where K is the *Gladstone - Dale constant* depending on the type of gas, n is the refractive index, and ρ is the gas density. Here, $K = 25.63 \times 10^{-4}$ m^3/kg for hydrogen [42]. This equation is clearly dependent on density, which (as seen before) becomes a function of the Mach number in compressible flow. Suppose a light source directed at an arbitrary plane, present in a confined vacuum in space. The rays emitted from the source propagate towards the plane, creating a projection of the light source.

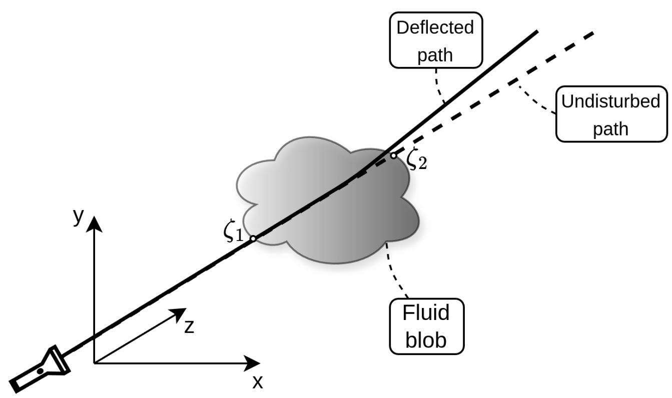

Figure 17: Light deflection by a blob of fluid

Now, a sudden high-pressure fluid release occurs in the confined space, creating all kinds of flow structures. The ray propagating through the field passes through this fluid. Furthermore, because of violent release, the fluid density is neither a constant field. A re-evaluation of the original projection on the plane shows a different image.
Looking back on Equation 4.5, the variable density field caused a change in the refractive index n, which deflected the ray emitted from the light source from its original path, resulting in a displacement Δx, Δy and an angle θ_x, θ_y. Based on these parameters, one can distinguish between different optical visualization methods: Shadowgraph and Schlieren imaging.

Figure 18: Shadow graph of a candle showing the hot air plume rising from the flame

4.2.1 Shadowgraph imaging

In everyday life, light rays emitted from the Sun create many shadowgraphs during the day. Examples in which actual flow structures are visualised include the shadow of air rising from hot asphalt, candles, or a campfire. Aside from more basic shadow-graphing, e.g. completely blocking a light ray's path, Figure 18 demonstrates that the rising air is not completely blocking light, rather changing its intensity. The changing density of air causes a change in the refractive index, which bends light again out of its original path. The relative changes light intensity in the plane, where high density obstacles cause low intensity. Through analysis, it can be derived that the relative variations in light intensity on the observation plane are as follows [43]

$$\frac{\Delta I}{I} = l \int_{\zeta_1}^{\zeta_2} \left(\frac{\partial^2}{\partial x^2} + \frac{\partial^2}{\partial y^2} \right) (\ln n) dz \tag{4.6}$$

where ζ_1 and ζ_2 are the inner and outer coordinates of the fluid blob, n is the refractive index. As n is a function of density, the intensity is proportional to the second derivative of density. As light is deflected by the blob, local spots become unfocused as a consequence. This is a spatial phenomenon, hence the second derivative.
This principle can be employed in research purposes to analyse flows. These setups typically include a point light source, lenses, a recording plane, and a camera. In such setups, the recording plane can be the actual camera sensor or a clear white background. The point light source emits a diverging beam, which is bundled via the magnifying glass. Optionally, an additional magnifying glass can be used to focus the beam back towards a camera after travelling through the obstacle. The camera lens is then used finally to focus the image on the recording plane (or sensor).

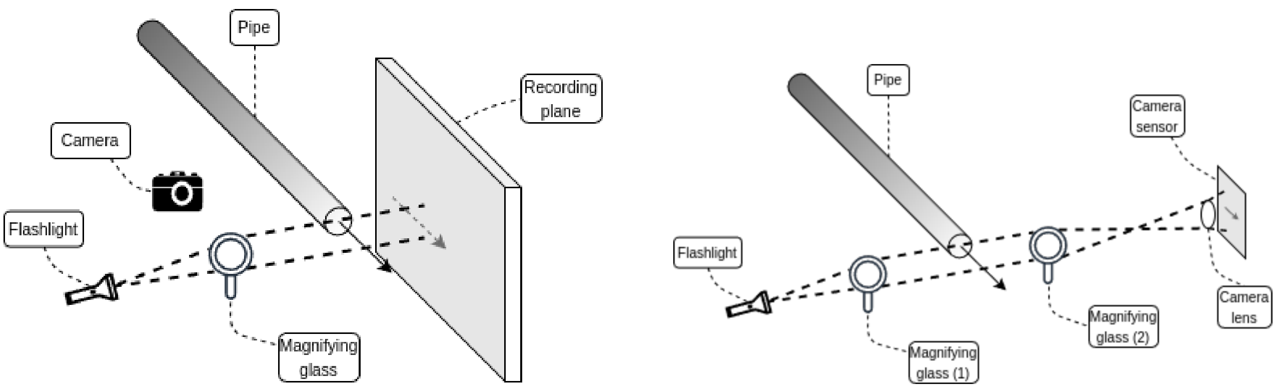

(a) Shadow graph setup with one magnifying lens

(b) Shadow graph setup with two magnifying lenses

Figure 19: Shadow graph setups

4.2.2 Schlieren imaging

Shadow graph imaging is easily accomplished and already shows insightful flow structures. If more features must be revealed, Schlieren imaging offers a solution. In this method, the edge of the knife plays an important role. It essentially acts as a filter by literally cutting off part of the light. Looking back on Figure 17, where the light ray was deflected by the blob of fluid, it would finally reach a plane in a different position compared to its undisturbed counterpart. By now introducing a knife edge in the right position, the deflected ray can be blocked from the recording plane. As the deflected components do not reach the recording plane, shadows are formed. The setup is arranged so that the focal point of the lens coincides with the tip of the knife edge. In a uniform medium, undisturbed light rays converge at this point. However, when a gradient occurs in the refractive index of a fluid - such as those caused by shockwaves - light rays are slightly deflected before reaching the knife. These deflected rays strike the knife edge at different positions; some may be blocked, others pass over the knife. Because these deflections occur in the direction of the refractive index gradient, the orientation of the knife edge (e.g., horizontal or vertical) determines which component of the gradient is visualised. A horizontal knife edge emphasises vertical gradients, while a vertical knife edge emphasizes horizontal gradients. In this way, the knife edge acts like a spatial filter, translating small optical deflections into visible contrast in the final image.

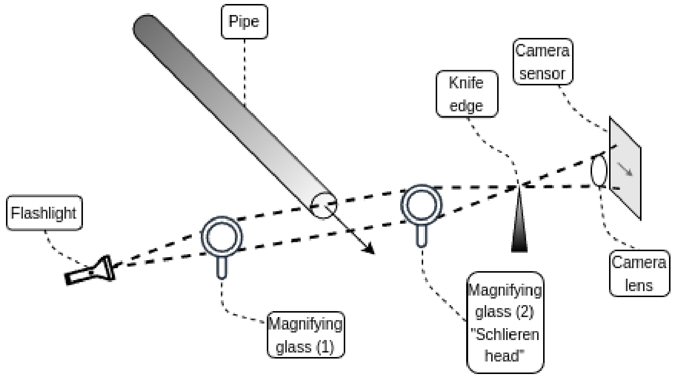

Figure 20: Schlieren imaging setup

The light intensity is thus governed by changes in the refractive index. Employing the Gladstone - Dale equation for this purpose again gives the following equation [43]:

$$\frac{\Delta I}{I} = \frac{K f_2}{H} \int_{\zeta_1}^{\zeta_2} \frac{\partial \rho}{\partial y} dz \tag{4.7}$$

New terms appear in this equation for the light intensity, such as f_2 is the distance towards the Schlieren head, as shown in Figure 20. Here, H is the slit height of the undisturbed image. This equation tells us that the light intensity variations are proportional to the gradients of density in one particular direction. Depending on the orientation of the knife, one can choose this direction. It is clear from this setup that the focal point and schlieren head must be carefully determined in order to make a qualitative image. Slight misalignment can ruin the picture.

4.3 Flow Features Observed in Optical Images: Shockwave Analysis

Abrupt changes in flow density become visible in the optical imaging techniques. All of these methods rely on a different order of derivative with respect to density, and a different projection shows the results. However, when dealing with shock waves, derivatives become *ill-defined* as large discontinuities appear. This leads to steep curves when viewing higher order terms. This is an important property when observing shockwaves with optical methods. Consider the following $step$ function:

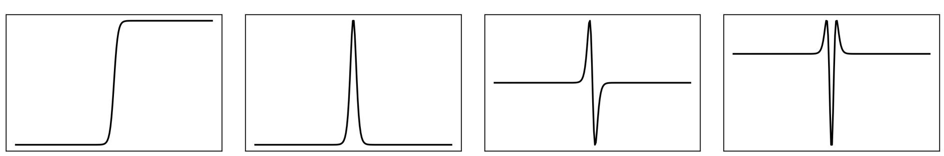

(a) Step function (b) First derivative (c) Second derivative (d) Third Derivative

Figure 21: Step function with derivatives

No matter the order of the derivative, the spontaneous *step* keeps reappearing in the same location. This useful property spoils the location of shockwaves even when capturing a simple shadow graph. The resulting images that contain shock waves can show a wide variety of flow structures. To analyse these structures, an overview of the main characterizing structures is provided next.

4.3.1 Shock Waves and Expansion Fans

Based on gas properties, such as their specific heats, a sufficient difference between static and total quantities can spoil the presence of sonic, or even supersonic, conditions. For example, the isentropic flow equation for pressure (eqs. 2.18) indicates that for a 52% difference between static and total pressure, a critical condition holds [16].

Looking back on the experimental configuration, a release of high pressure hydrogen gas might reach these conditions. Once sonic or supersonic flow is established, a range of distinct compressible flow structures may form. This depends on geometry, flow deflections, etc. These flow structures include normal shocks, oblique shocks, and bow shocks. These represent sudden compressive disturbances, as wel as Prandtl-Meyer expansion waves, which describe smooth, isentropic expansions around corners. Each of these features plays a fundamental role in shaping behavior of high-speed gas jets and will be discussed in the following sections.

4.3.1.1 Normal Shocks

A normal shock wave is by definition perpendicular to the flow direction. Upstream, the flow is supersonic, and downstream, the flow is subsonic, causing a rise in pressure, temperature, and density. The shock wave appears as a thin region in which a rapid disturbance takes place, sometimes to be seen as a blurry or obscured line. In steady flow conditions, shock waves are also a steady phenomena. They do not move or change, even when downstream conditions are changed.

4.3.1.2 Oblique Shocks

An oblique shock wave forms when a supersonic flow is deflected by a surface, such as a wedge or a corner. Unlike a normal shock, it meets the flow at an angle, causing both a sudden rise in pressure, temperature, density, and a change in flow direction. The flow remains supersonic after the shock, though at a lower Mach number. Oblique shocks are commonly observed as sharp, slanted lines extending from points of deflection. As with normal shocks, they are thin and steady in nature, maintaining their position as long as the flow conditions and deflection angle remain unchanged.

4.3.1.3 Bow Shocks

If a blunt object is encountered in supersonic flow, a bow shock can appear. These shockwaves are detached from the geometry with a curvature. As the flow cannot turn fast enough to follow the contour, a curved shock wave forms in front of the geometry. Bow shocks are typically stronger near the centreline, implying a bigger transition in pressure, temperature, velocity, etc. The flow behind these shocks slow down significantly, often becoming subsonic close to the geometry's surface. In steady flows, bow shocks are also a steady phenomena, seen in flow visualisations like curved wavefronts upstream of an obstacle.

4.3.1.4 Prandtl-Meyer Expansion Waves

The latter shocks described a compressive process, where Prandtl-Meyer expansion waves describe the opposite. When supersonic flow turns around a rounded corner, the flow gradually accelerates, and both pressure, temperature, and density drop. These regions are fan-shaped. These expansion waves appear as a series of infitesmall changes spread ofer an angle. They are commonly seen at the outlets of nozzles where the flow adjusts to ambient conditions. Like shocks, these too are for constant flow a steady phenomena.

4.3.2 Jet Flow Classifications and Structures

In case of the release of high pressure gas through a pipe leads to the formation of a jet at its outlet. These jets can be classified in two types: *Under-expanded* and *over-expanded* jets. In the right circumstances, these jets can form a phenomenon called shock diamonds.

4.3.2.1 Under-Expanded Jets

As the flow exits its channel but has not yet fully expanded to match the ambient pressure, the jet is said to be under-expanded. This occurs when the pressure at the nozzle exit is still higher than the surrounding atmosphere. The mismatch causes the jet to expand rapidly through a series of Prandtl–Meyer expansion waves, followed by compression (shock) waves that try to restore balance. These alternating expansion and compression regions can interact to form a repeating structure along the jet axis. Under-expanded jets are commonly observed in high-pressure gas releases, where the nozzle is too short or too narrow to allow full expansion inside the system.

4.3.2.2 Over-Expanded Jets

When the pressure at the nozzle exit is lower than the ambient pressure, the jet is said to be over-expanded. In this case, the external environment effectively "pushes back" on the jet, compressing it. This leads to the formation of oblique shock waves just outside the nozzle exit, which attempt to bring the flow back up to ambient pressure. If the pressure mismatch is too large, the shocks can induce flow separation near the nozzle walls, disrupting the jet's structure. Over-expanded jets are more sensitive to changes in back pressure and are commonly seen in altitude-varying conditions like rocket nozzles during ascent.

4.3.2.3 Shock Diamonds (Mach Disks)

When a jet exits into the ambient environment with a significant pressure mismatch—especially in under-expanded conditions—it can form a repeating pattern of bright and dark regions known as shock diamonds or Mach disks. These structures result from the complex interaction of expansion fans and shock waves as the jet tries to adjust to the surrounding pressure. The bright regions correspond to zones of compression and heating, while the dark regions indicate expansions and cooling. At the center of these structures, a Mach disk may form—a nearly normal shock that abruptly slows the supersonic core of the jet. Shock diamonds are often visible in optical imaging and are a classic indicator of high-speed jet flows.

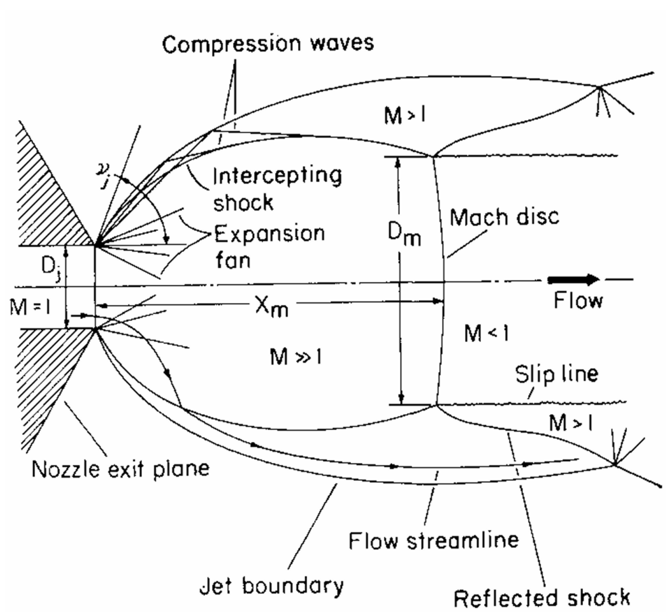

Figure 22: Highly under-expanded sonic jet structure [44]

Much information is revealed by the location of the Mach disk. The relation between the Mach number and the ratio of horizontal distance x_m and diameter of the outlet is described by Crist et. al. [44]. Here, the equation is rewritten to solve for M:

$$M \simeq \left\{ \frac{x_m}{D} \left[\left(\frac{\gamma - 1}{2} \right)^{\frac{\gamma}{\gamma-1}} \frac{\gamma + 1}{4.8\gamma} \right]^{-1/2} \right\}^{\gamma - 1} \tag{4.8}$$

This equation is used in Section 6.4 to determine the maximum Mach number in the under-expanded jets.

4.4 Experimental Procedure

This section demonstrates the strategy for collecting measurements. First, the procedure for collecting the pressure, temperature and mass flow rate is described. Secondly, the optical imaging strategy is demonstrated.

4.4.1 Test matrix

Each test subject is tested as follows: After throttling the inlet pressure to achieve the desired mass flow rate, the instruments were enabled to measure the flow properties over a time span of 30 seconds. After 30 seconds, the throttle was closed. In between measurements, the data was saved and shortly checked for completion. Next, the experiments were resumed for a total of three measurements per flow rate. The flow rates in Table 11 were based on preliminary calculations and adjusted during experiments based on the measured conditions to try to attempt an even spread over Mach numbers. Henceforth, smaller diameters were tested to a lower maximum mass flow rate as higher velocities were achieved far sooner.

Test subjects	∅ 8	∅ 5	∅ 3.2
Target $\dot{m}$ $\frac{g}{s}$	0.5	0.5	0.25
	1	1	0.5
	2	2	1
	3.5	3.5	1.5
	7	7	2

Table 11: Test matrix

The tests were conducted at the test site shown in Figure 23. The experimental setup, shown in Figure 24 was connected to the hydrogen storage vessel, shown in Figure 25.

Figure 23: Test site

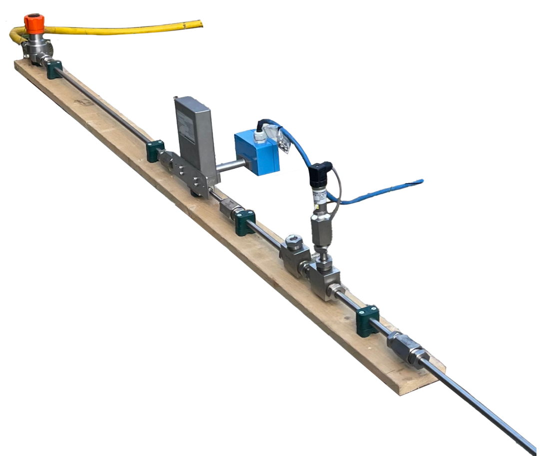

Figure 24: Test setup

Figure 25: Gaseous hydrogen storage container

4.4.2 Optical Imaging

As experiments were conducted outside and the experimental setup had to be rebuilt several times, a simple setup was preferred. As the main goal behind optical imaging was to get an impression of flow structures and verify the existence of sonic flows, shadow graphing already seemed to be a sufficient option. A complementary test set-up was constructed to capture shadow graphs.

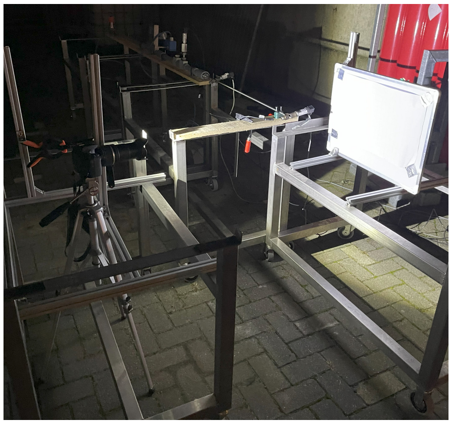

(a) Camera, experimental setup, and recording plane

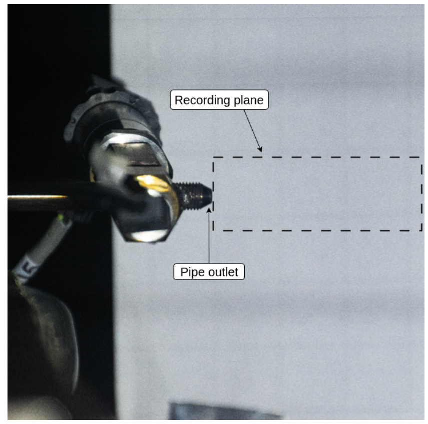

(b) Picture frame of the setup

Figure 26: Shadow graphing setup

An 800 lumen flash light with a single bright LED was aimed at the pipe outlet. A screen was placed close behind the pipe outlet. By moving the recording plane away from the pipe outlet, the sharpest image was iteratively found by observing the flow. Finally, a camera with adjustable shutter speed and a capable zooming lens was used to capture the image. Shadow graph images were captured using the ∅ 3.2 test subject's outlet.

5 Methodology

The previous sections have provided the relevant theory about modelling approaches and described the configuration of the experimental setup. This section presents their use and how they were compared with experimental measurements. Secondly, the implementation of empirical and analytical models is shown, subsequently followed by the comparative approach to the experimental data. In addition, correction methods are elaborated upon. Finally, the numerical modelling approach is shown, presenting the boundary conditions used and the initialisation of the solver.

5.1 Analytical and empirical modelling approach

After collecting the measurements as described in Section 4.4.1, the data was imported into a custom developed Python script, which contains the empirical and analytical model equations.
The models are used to compute the outlet conditions of gaseous hydrogen on given inlet conditions, in turn based on the measured inlet conditions. Empirical and analytical models are elaborated through flow charts, demonstrating the step-by-step solution procedure for obtaining the outlet state. Here, we demonstrate how the outlet temperature, pressure, and velocity are computed. Subsequently, these results are qualitatively presented in Section 6 and discussed in Section 7.

5.1.1 Darcy-Weisbach

The Darcy-Weisbach equation is straightforward to use, but does not provide a clear approach to compute the outlet temperature. To do so, we incorporate an energy equation for enthalpy:

$$h_1 + \frac{1}{2}u_1^2 = h_2 + \frac{1}{2}u_2^2 \tag{5.1}$$

By assuming an ideal gas, this equation becomes:

$$C_p T_1 + \frac{1}{2}u_1^2 = C_p T_2 + \frac{1}{2}u_2^2 \tag{5.2}$$

As both T_2 and u_2 are still unknown, proceed by reformulating u_2 by using the ideal gas law and the mass flow rate:

$$u_2 = \frac{\dot{m} R T_2}{p_2 A} \tag{5.3}$$

As p_2 can be derived using Darcy-Weisbach, this equation can be used to solve equation 5.2 for T_2:

$$C_p T_1 + \frac{1}{2}u_1^2 = T_2 \left(C_p + \frac{\dot{m} R}{p_2 A} \right) \tag{5.4}$$

Rewritten for T_2:

$$T_2 = \frac{C_p T_1 + \frac{1}{2}u_1^2}{C_p + \frac{\dot{m} R}{p_2 A}} \tag{5.5}$$

Thereby, this is solved by using C_p from inlet conditions, assuming constant specific heats. Furthermore, the temperature calculation relies here on the assumption of an adiabatic process and no work.

1. **Define pipe properties:** Diameter D, area A, length L, and roughness ϵ.
2. **Read measurement data:** pressures p_1, p_2, p_3; temperatures T_1, T_2, T_3; and mass flow rate $\dot{m}$.
3. **Compute thermophysical properties at p_2, T_2 using CoolProp:**
   - Density $\rho(p_2, T_2)$
   - Viscosity $\mu(p_2, T_2)$
   - Heat capacity $C_p(p_2, T_2)$
4. **Compute mass averaged flow velocity:**
$$\bar{u} = \frac{\dot{m}}{\rho A}$$
5. **Compute Reynolds number:**
$$Re = \frac{\rho \bar{u} D}{\mu}$$
6. **Determine the average friction factor f using the Haaland equation (Table 2).**
7. **Compute outlet pressure using Darcy-Weisbach (Eq. 2.15):** p_3
8. **Compute outlet temperature (Eq. 5.2):** T_3

Corrections on Darcy-Weisbach

As the Darcy-Weisbach equation is directly scaled by the friction factor, two different friction factor equations are compared. Here, the Churchill friction factor is chosen because it obtains higher values than the Haaland equation for the same arguments.
A quick estimate shows (See Table 2) for the friction factor equations:

$$Re = 10^5, \quad \varepsilon/D = 0.0002$$

$$f_{\text{Churchill}} \approx 0.0203, \quad f_{\text{Haaland}} \approx 0.0187$$

$$\text{Difference: } \frac{f_{\text{Churchill}} - f_{\text{Haaland}}}{f_{\text{Haaland}}} \times 100\% \approx 8.6\%$$

5.1.2 Weymouth and Panhandle equations

The Weymouth and Panhandle equations rely on the assumption of isothermal flow, thus $T_3 = T_2$.
Furthermore, the effects of gravity were neglected in the modelling approach as there were no elevation changes in the experimental setup.
These equations require an efficiency factor η, which is provided by Ouyang et. al. [22] as a function of the outlet pressure. As we wish to find the outlet pressure, this efficiency factor is to be corrected later.
Finally, temperature and pressure were required under standard conditions (T_{sc} and p_{sc}), which were based on ambient pressure and temperature, respectively.

1. **Define pipe properties:** Diameter D, length L.
2. **Define standard conditions: Pressure p_{sc} , temperature T_{sc}.**
3. **Read measurement data:** Pressures p_1, p_2, p_3; temperatures T_1, T_2, T_3; and mass flow rate $\dot{m}$.
4. **Compute thermophysical properties at p_2, T_2 using CoolProp:**
   - **Density** $\rho(p_2, T_2)$
   - **Compressibility factor** $Z(p_2, T_2)$
   - **Ratio of specific heats** $\gamma(p_2, T_2)$
5. **Compute volumetric flow-rate:**
$$Q = \dot{m}/\rho$$
6. **Define corresponding constants a_1, a_2, a_3, a_4, and a_5 from Table 4.**
7. **Compute Reynolds number:**
$$Re = \frac{\rho \bar{u} D}{\mu}$$
8. **Compute outlet pressure using Weymouth or Panhandle (Eq. 2.17):** p_3
9. **Assign outlet temperature:** $T_3 = T_2$

Corrections on Weymouth and Panhandle

The Weymouth and Panhandle equations contain an efficiency factor (η) in both formulations. Although there are correlations available for the Panhandle based on roughness and Reynolds numbers, the most direct approach to obtain this efficiency factor is to adjust it based on the difference between measured and predicted quantities [22]. In the results of these equations, it is chosen to retain $\eta = 1$ to observe how these equations perform in their most basic form. After all, the efficiency factor directly scales the flow rate as it is multiplied directly by the expression, so the gradient of these equations should already follow the curvature of the measurements obtained for good results. If this is not the case, adjustment of the efficiency factor would not drastically improve the performance of these equations over the full range of measurements.
The Weymouth and Panhandle equations contain a root in which a subtraction takes place between the inlet pressure and the volumetric flow rate. For invalid combinations of inlet pressure and flow rate, this root can obtain negative arguments. In such cases, it is chosen to reject the solution entirely and the calculation is advanced to the prediction of the next available measurement point. This process is continued until all measurement points have been evaluated. As will be shown in Section 6, an additional comparison is provided where the Weymouth and Panhandle equations are used to predict the mass flow rate. This comparison is provided to observe if these equations produce more results if they are used in their standard form, thereby computing a flow rate instead of an outlet pressure.

5.1.3 Fanno flow

The procedure to calculate the outlet pressure and velocities using the Fanno flow equation requires a few steps, presented next:

1. Find the average friction factor:
   (a) Find the Reynolds number.
   (b) Find the average roughness ϵ of the pipe (Table 3).
   (c) Calculate the friction factor using the Haaland equation (Table 2).
2. Find the ratio of specific heats using the CoolProp package.
3. Find the Mach number:
   (a) Find the local gas density using the given pressure, temperature, and NIST equation of state 2.36.
   (b) Find the average gas velocity using the mass flow-rate, the gas density, and the cross-sectional area of the pipe, viz.:
   $$\bar{u} = \frac{\dot{m}}{\rho A}. \tag{5.6}$$
   (c) Find the local speed of sound a using lookup tables.
   (d) Compute the Mach number.
4. Compute the critical Fanno number $\left(\frac{4\bar{f}L^*}{D}\right)_*$ by substituting the values found for M and γ into the right-hand side of equation 2.27.
5. Calculate the critical length by multiplying the right-hand side by $\frac{D}{4\bar{f}}$. If $L^* \geq L_{\text{pipe}}$, the flow becomes critical at the outlet of the pipe.
   (a) In case of critical flow, the outlet conditions can be found directly by substituting $M_{out} = 1$ into the Fanno property relations (Eqs. 2.31, 2.32).
6. Compute the inlet Fanno number $\left(\frac{4\bar{f}L}{D}\right)_1$ by substituting the values found for f, the pipe length L, and the pipe diameter D.
7. In case the outlet is not choked, the outlet conditions $\left(\frac{4\bar{f}L}{D}\right)_2$, are given by:
   $$\left(\frac{4\bar{f}L}{D}\right)_2 = \left(\frac{4\bar{f}L^*}{D}\right)_* - \left(\frac{4\bar{f}L}{D}\right)_1 \tag{5.7}$$
8. The outlet pressure, temperature, and density are subsequently found using the Fanno property relations (Eqs. 2.31, 2.32, and 2.33).

Further corrections on isentropic flow

As the mass flow rate increases, Fanno flow will eventually predict that the outlet will become critical ($M = 1$) under sufficient conditions, such as high roughness and fast inflow speeds. The correction procedure is to advance or postpone this critical point, thereby increasing or decreasing the critical length. This is accomplished by manipulating the friction factor. The Haaland and Churchill friction factors are employed for this purpose.

5.2 Numerical modelling approach

The CFD codes presented in this section are OpenFOAM and SU2. Firstly, OpenFOAM version 2312 was used with the rhoPIMPLEfoam solver, being a compressible solver that combines the SIMPLE and PISO algorithms.

Thus, being a segregated solver. Secondly, SU2 version 7.0.7 was used, offering a coupled solver. As analysed in Section 3, the $k-\omega$ SST model is most promising for wall-bounded flows, thus chosen to carry out the turbulence modelling.

5.2.1 Mesh generation

A structured mesh was created using SALOME, an open-source mesh generation tool. An unstructured mesh was avoided due to the predominantly axial flow expected in the pipe, which makes a structured mesh more suitable. To accommodate the required inflation layers, an OH-grid topology was selected. This configuration provided greater control over cell size, allowing coarser cells in the pipe centre while maintaining fine resolution near the walls. As a result, the structured OH-grid proved to be the optimal choice compared to the radial mesh.
In the first trail runs of the SU2 and OpenFOAM solvers, it was decided to assign a quarter OH-grid to OpenFOAM to decrease computational load and make use of a symmetry condition on the horizontal and vertical side walls.

Solver	Number of cells
OpenFOAM	1054812
SU2	1810432

Table 12: Mesh statistics

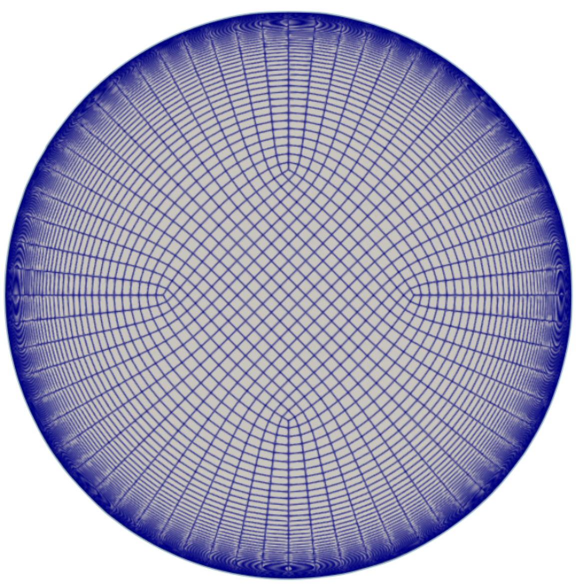

(a) Mesh used in SU2

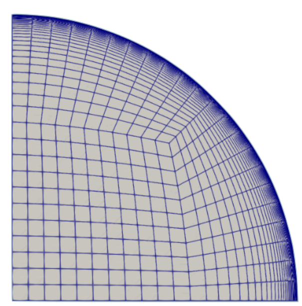

(b) Mesh used in OpenFOAM

Figure 27: Cross-section view of the meshes

5.2.2 Boundary Conditions

The outlet of the pipe is a boundary to the computational domain. Additionally, a CFD simulation requires specified boundary conditions, which makes the computation of the outlet conditions ambiguous. A different strategy is required to estimate the outlet conditions. Here, a total pressure and temperature are assigned to the inlet, and the outlet is fixed to a guessed static pressure. Upon solving the case, thereby reaching a steady state, the solver converges to a mass flow rate. Subsequently, this allows for a verification if the guessed static outlet pressure was, in fact, correct. The computational domain lies behind a series of pipes. The gaseous hydrogen passed from the storage vessels, through a flexible tubing, through the mass flow meter, the first thermocouple and pressure sensor, and finally through a reducer into the test subject. It is therefore not reasonable that the flow has not experienced any developments in turbulence.The pipe inlet turbulence is estimated using the following equation:

$$k = \frac{3}{2}u^2 I^2 \tag{5.8}$$

where the inlet turbulence is estimated with[45]:

$$I = 0.16 Re_D^{-\frac{1}{8}} \tag{5.9}$$

Furthermore, the turbulence intensity should typically be around 1-10% [45]. Making an initial guess of the flow at $\dot{m} = 7\ \frac{\mathrm{g}}{\mathrm{s}}$, a density of $1\ \frac{\mathrm{kg}}{\mathrm{m}^3}$, a viscosity of $\mu = 10^{-5}$ Pa s for $D = 5$ mm tubing, results in a turbulence intensity of 3.5%, being in line with the provided range. Consequently, the inlet turbulence kinetic energy can be estimated. Also, the dissipation rate ω should be estimated:

$$\omega = \frac{\epsilon}{C_\mu k} \tag{5.10}$$

Requiring the turbulent dissipation rate ϵ:

$$\epsilon = C_\mu \frac{k^{\frac{3}{2}}}{I} \tag{5.11}$$

Now we can solve ω. Whereas C_μ is the model constant for $k - \epsilon$ and $k - \omega$ turbulence models. For $k - \omega$ SST, $C_\mu = 0.09$ [35].

The boundary conditions for the remaining variables are given in Table 13. Here, the Neumann fields indicate that the gradient of the variable is zero at the considered boundary.

Variable	inlet	field	outlet
p_0 (Pa)	8.325e5	-	-
p (Pa)	-	8.325e5	477600
T_0 (K)	291	-	-
T (K)	-	291	Neumann
u (m/s)	Neumann	100 m/s	Neumann
k	234	0	0
ω	10	0	0
α_T	0.85	0	0

Table 13: Boundary conditions

5.2.3 Solver Setup

The openFoam solver required an initialisation procedure in order to maintain stability. By imposing a large pressure gradient right from the start, the solver would crash. To prevent this, the following actions were taken:

1. 0 - 10000 iterations: Do not incorporate turbulence models. Start with a slight pressure difference between inlet and outlet of about 10 kPa.

2. 10000 - 20000 iterations: Reduce the outlet pressure with 100 kPa. Monitor the residuals right after this step. If the simulation becomes unstable, start over and let the case initialise longer.

3. 20000 - stop condition: Enable the turbulence model.

5.3 Error Assessment

For each measurement point, either pressure or temperature, the models make a corresponding prediction. The difference is evaluated using the absolute difference:

$$e = \sum_{i=0}^{N} \left| \phi_{\text{exp},i} - \phi_{\text{model},i} \right| \tag{5.12}$$

where e is the total error for all data points, ϕ_{exp} is an arbitrary measurement data set, and ϕ_{model} is an arbitrary predicted data set.

This section outlined the methods used to perform calculations with both analytical and empirical models, as well as the setup of the CFD solver. The following section presents the results and predictions obtained from these approaches.

6 Results

The predictions of the outlet pressure and temperature are made using the configuration shown in Figure 28.

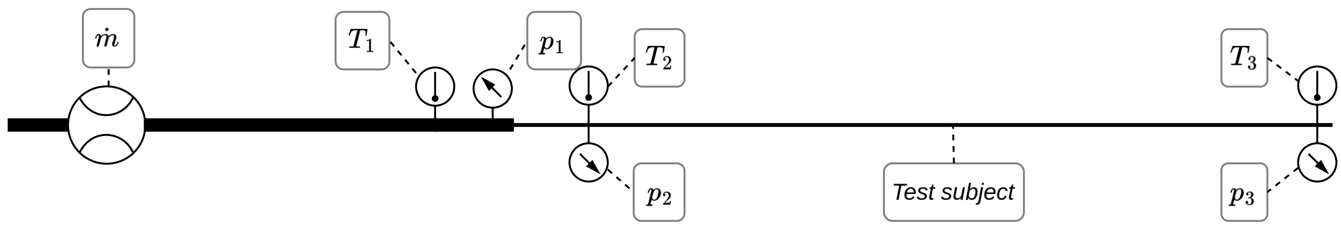

Figure 28: Sensor locations

The results are presented as follows. The test subjects ∅ 8, ∅ 5, and ∅ 3.2 are exchanged at the location of the "*test subject*". The following results were derived from measurements obtained using the mass flow rate sensor $\dot{m}$, pressure sensors (p_1 to p_3) and thermocouple sensors (T_1 to T_3):

1. The influence of diameter on pressure over an increasing mass flow rate.
2. The relation between Mach and Reynolds numbers over an increasing mass flow-rate

Using the measured mass flow rate $\dot{m}$, and test subject inlet conditions p_2 and T_2 to compute p_3 and T_3 using:

3. Darcy-Weisbach, with the Haaland and Churchill friction factor.
4. Weymouth and the Panhandle equations.
5. Fanno flow to compute the outlet velocity M_3, with the Haaland and Churchill friction factor, and using:
   (a) Fanno flow Equations 2.31 and 2.32.
   (b) Isentropic flow Equations 2.18 and 2.19.
   (c) Isentropic flow Equations with the SRK EOS from Equations 2.46 and 2.47.

Finally, the CFD results of the SU2 and OpenFOAM simulations are presented on the length of the pipe ∅ 5 and the measurements from thermocouple sensors T_2 to T_3, and pressure sensors p_2 to p_3. An overview of all individual measurements are given in Appendix E. Relevant results to describe research results are presented in this section.

6.1 Comparison between diameters

The first comparison is made using pressure sensor p_1, located before the test subjects in a fixed 8 mm pipe. Here, Figure 29 reflects the change in the mass flow rate - pressure relation when ∅ 8, ∅ 5, and ∅ 3.2 are interchangeably placed behind pressure sensor p_1.

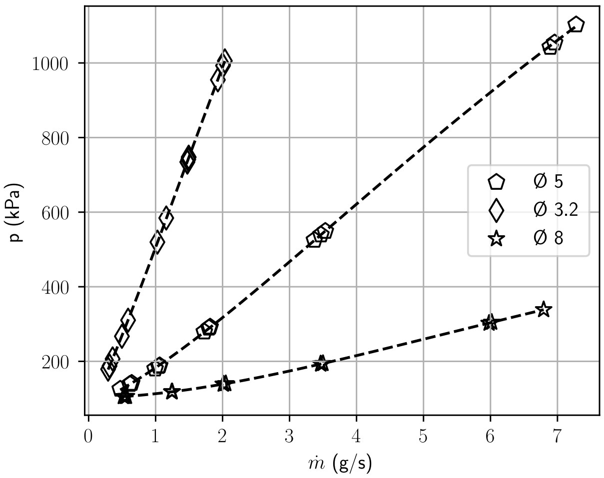

Figure 29: p_1 for ∅ 8, ∅ 5, and ∅ 3.2

Test subject	Gradient kPa/(g/s)
∅ 8	37.3
∅ 5	142.8
∅ 3.2	475.1

Table 14: Average slope of pressure to mass flow rate

As the flow must compensate for the smaller diameters of ∅ 5 and ∅ 3.2, it can be seen that a higher pressure is required to accommodate the same mass flow rate. The mass conservation equation (Eq. 2.7) therefore indicates that the density must have increased too. Furthermore, the mass flow rate - pressure relation show to obey a linear relation. Proceeding to pressure sensor p_2, located directly on ∅ 5 and ∅ 3.2.

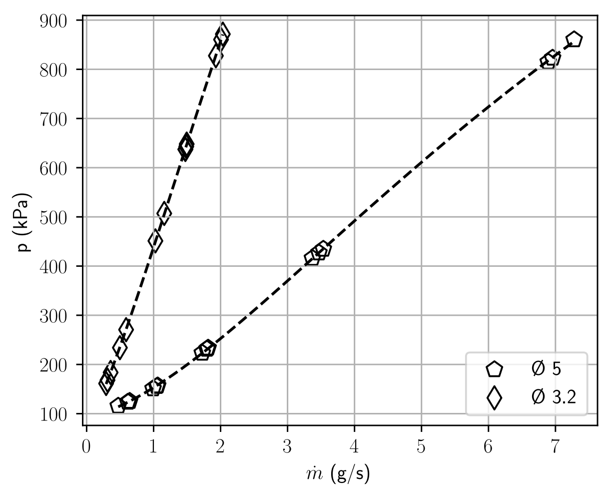

Figure 30: p_2 for ∅ 5 and ∅ 3.2

Test subject	Gradient kPa/(g/s)
∅ 5	108.9
∅ 3.2	408.5

Table 15: Average slope of pressure to mass flow rate

The pressure was slightly reduced, resulting in a reduction of the slopes shown in Table 15.
Finally, pressure sensor p_1, also located directly on ∅ 5 and ∅ 3.2.

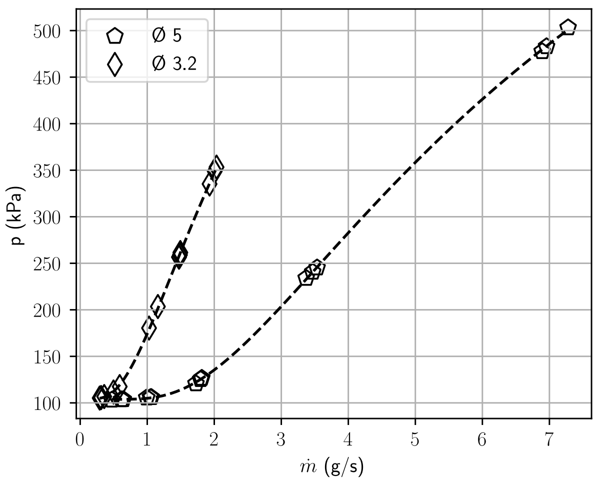

Figure 31: p_3

Test subject	Gradient kPa/(g/s)
∅ 5	58.3
∅ 3.2	143.8

Table 16: Average slope of pressure to mass flow rate

At the lower bound of the curves, p_3 remained close to atmospheric pressures for ∅ 5 at lower mass flow rates, eventually picking up after 1 g/s. Thereby, showing that no change in pressure was required for ∅ 5 to accommodate flow rates below 1 g/s.

The slope decreased for all test subjects when moving from p_1 to p_3. Table 17 lists the ratio between slopes for each pressure sensor per test subject. The ratio between the slopes of ∅ 5 and ∅ 3.2 remains on average 3.2.

Ratio of gradients	p_1	p_2	p_3
∅ 3.2 / ∅ 8	12.7	-	-
∅ 5 / ∅ 8	3.8	-	-
∅ 3.2 / ∅ 5	3.3	3.8	2.5

Table 17: Ratio of gradients kPa/(g/s) over different test subjects

Returning this analysis to the mass conservation equation reveals that the area ratio and the mass flow rate do not seem to be directly proportional. That is, the area ratio of ∅ 3.2 to ∅ 5 is approximately 2.44, while the pressure and mass flow rate slope between ∅ 3.2 and ∅ 5 was on average 3.2. Hence, either the density and the velocity also increased to compensate for the change in area to accommodate the same mass flow rate.

Changing the analysis by incorporating dimensionless quantities, the Mach and Reynolds numbers show a very different characteristic. A comparison is shown in Figures 32a and 32b, where test subjects are interchanged while observing the relation between Mach and Reynolds numbers. The Mach and Reynolds numbers are determined using p_1 and T_1, hence using $D = 8$ mm. Each test subject enters a steep asymptote, where the Mach number of the asymptote is advanced by reducing diameter. Comparison of the curves individually in Figure 32a shows that for a given Reynolds number, the Mach number grows nearly linearly with diameter. The Reynolds-Mach relation shows to be predominantly invariant at low Reynolds numbers and shows a rapid decrease that moves to $Re = 100000$.

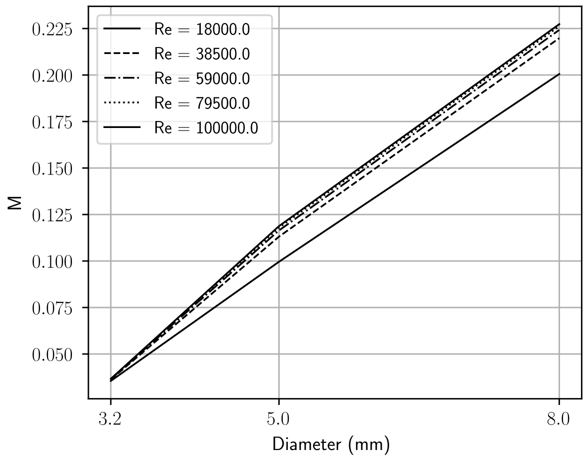

(a) Mach to Reynolds relation for varying diameter

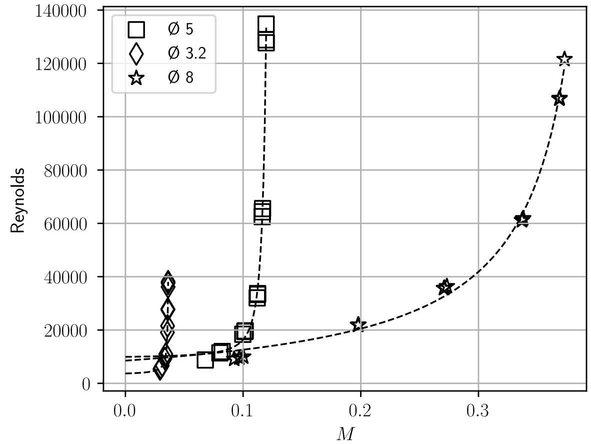

(b) Diameter to Mach relation for varying diameter

Figure 32: Flow characteristics for varying diameter at p_1 and T_1

6.2 Comparison of analytical and empirical models against measurements

The subsequent subsections present the results of both the analytical and empirical models. For each type of model, two tables are included for ∅ 5 and ∅ 3.2, providing the absolute errors between the measurements and the corresponding model.

6.2.1 Darcy-Weisbach

Viewing Tables 18a and 18b shows that the Churchill friction factor had the best agreement with measurements. However, the temperature deviations remained essentially unchanged by the friction factor.

Friction factor	Error p_3 (kPa)	Error T_3 (K)
Haaland	1807.0	122.0
Churchill	489.5	122.0

(a) ∅ 5

Friction factor	Error p_3 (kPa)	Error T_3 (K)
Haaland	3734.2	78.0
Churchill	2129.1	78.0

(b) ∅ 3.2

Table 18: Absolute errors in p_3 and T_3 for different friction factor models.

Although ∅ 3.2 had a larger error for pressure, its temperature error was comparatively lower. It can be seen from Figures 33a and 33c that the pressure error increases with the mass flow rate for Darcy-Weisbach equation. The Churchill friction factor not only better approximates the measurements, it also results in a decreased prediction of the pressure-mass flow rate gradient. This is a logical consequence from the definition of Darcy-Weisbach, where the friction factor is directly proportional to pressure loss. In terms of temperature predictions, Figures 33b and 33d show a disagreement in characteristics. The temperature measurements showed a slight decrease at lower mass flow rates. However, the variation remained within 1 K, which implies that the variation is below the thermocouple accuracy, as indicated in Table 10.

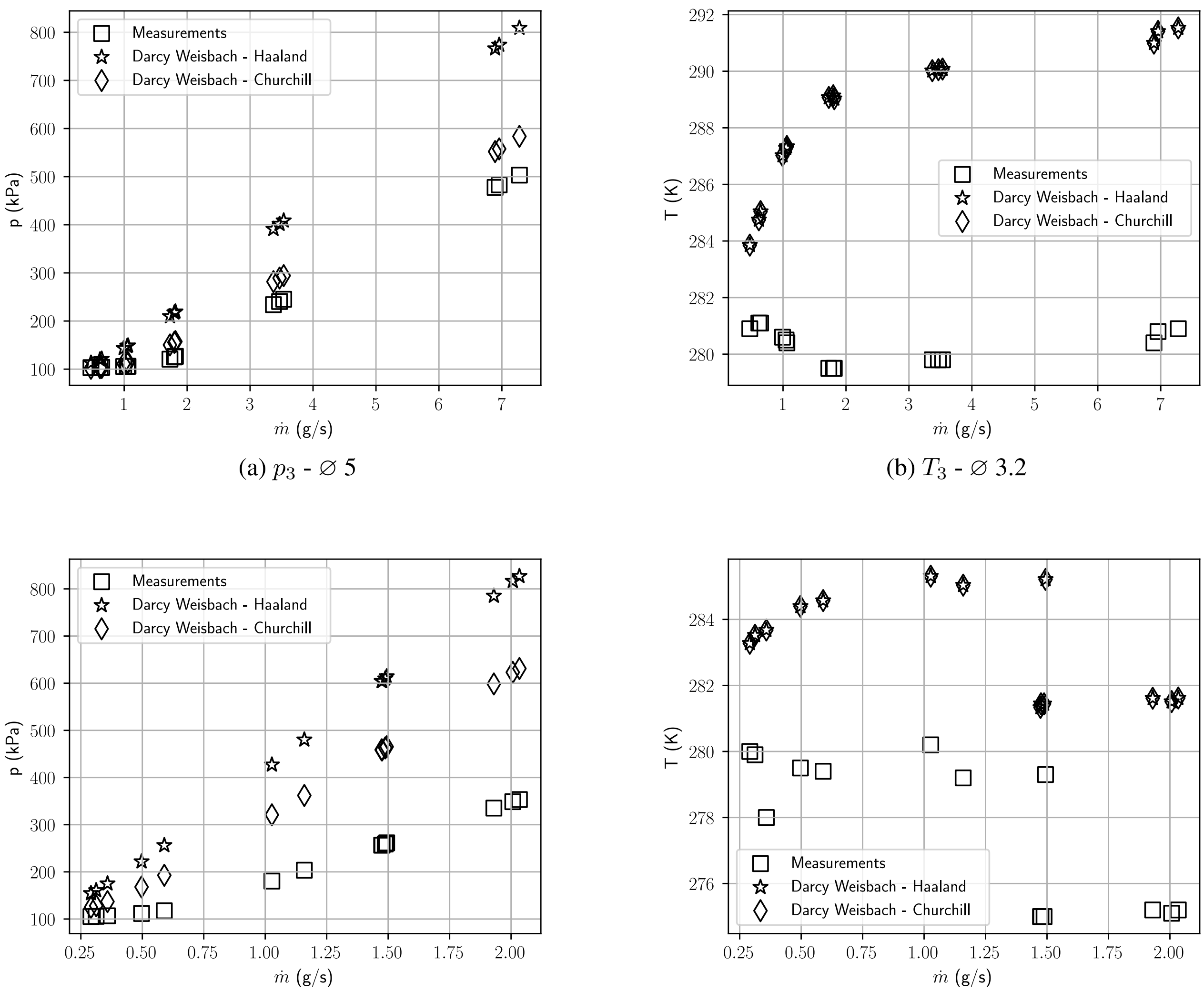

(a) p_3 - ∅ 5

(b) T_3 - ∅ 3.2

(c) p_3 - ∅ 3.2

(d) T_3 - ∅ 3.2

Figure 33: Comparison between measurements and Darcy-Weisbach predictions for p_3 and T_3.

6.2.2 Weymouth and Panhandle Equations

Solving the Weymouth and Panhandle equations for p_3 became rather problematic at low mass flow rate - inlet combinations. As indicated in section 2.5, the presence of a square root in these equations can result in negative arguments for invalid combinations of mass flow rate and inlet pressure. As a consequence, only higher mass flow rates allowed the prediction of p_3. Because these equations are based on the assumption of isothermal flow, these models cannot be used to determine the outlet temperature. Instead, the isothermal flow assumption is assessed by comparing T_2 to T_3. This subsection presents two approaches to broaden the analysis on the Weymouth and Panhandle equations. Namely, a traditional comparison to outlet pressure followed by an additional comparison to mass flow rate prediction.

Model	Error p_3 (kPa)	Error T_3 (K)
Weymouth	-	23.7
Panhandle	-	23.7

(a) ∅ 5

Model	Error p_3 (kPa)	Error T_3 (K)
Weymouth	-	28.7
Panhandle	-	28.7

(b) ∅ 3.2

Table 19: Absolute errors in p_3 and T_3 for Weymouth and Panhandle compared to the measurements

At the measurements where both the Weymouth and Panhandle equation produced results, the Weymouth equation had the best agreement. In contrast, the Panhandle equation provided more results, largely consisting of overestimations. From Tables 19a and 19b, it can be seen that the isothermal flow assumption provides only slight disagreement.

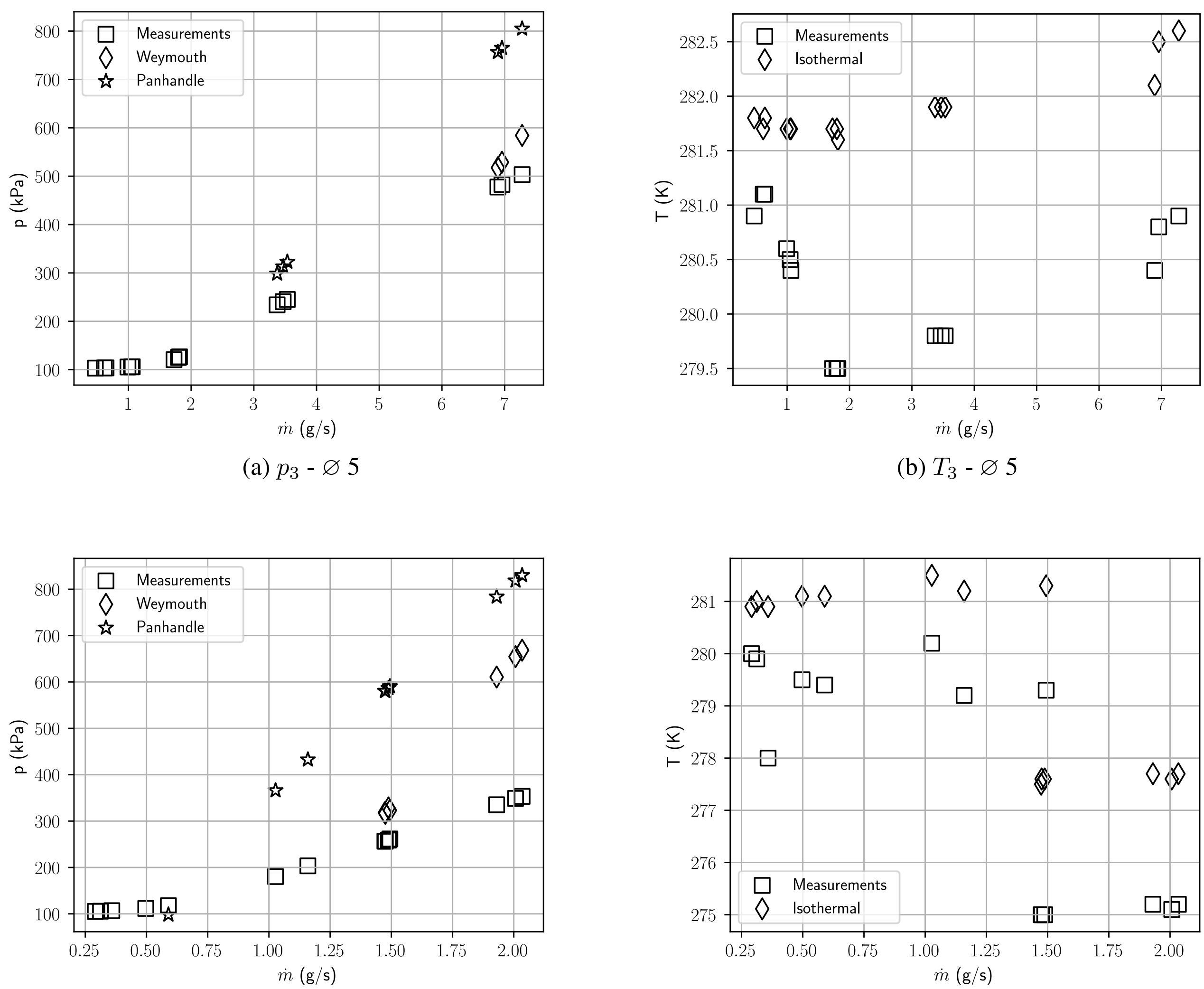

(a) p_3 - ∅ 5

(b) T_3 - ∅ 5

(c) p_3 - ∅ 3.2

(d) T_3 - ∅ 3.2

Figure 34: Comparison between measurements and Weymouth/Panhandle predictions for p_3 and T_3.

Despite poor pressure predictions, these models are well capable of providing mass flow rate predictions for the full measurement range. Furthermore, as can be seen in Tables 20a and 20b, the Weymouth equation provides accurate predictions below 1 g/s. Figures 35a and 35b show that the Weymouth equation predominantly underestimates the mass flow rate, whereas the Panhandle equation tends to overestimate the mass flow rate.

Model	Error $\dot{m}$ (g/s)
Weymouth	13.1475
Panhandle	35.9274

(a) ∅ 5

Model	Error $\dot{m}$ (g/s)
Weymouth	4.4548
Panhandle	23.3218

(b) ∅ 3.2

Table 20: Absolute errors in $\dot{m}$ for Weymouth and Panhandle compared to the measurements

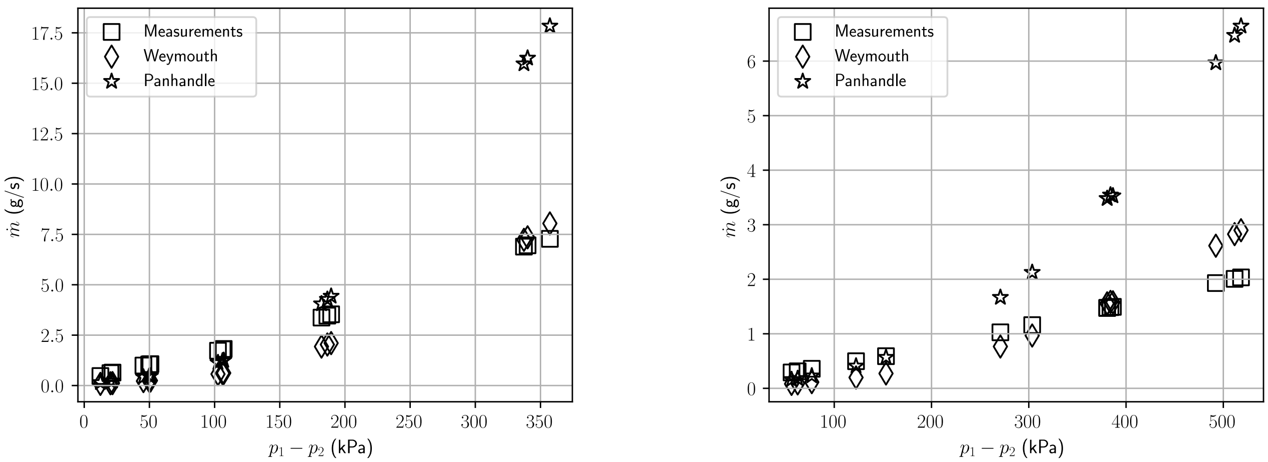

(a) ∅ 5

(b) ∅ 3.2

Figure 35: Mass flow rate predictions from Weymouth and Panhandle compared to measurements.

6.2.3 Fanno flow

The resulting Mach number M_3, computed by the Fanno flow equation, is treated in this section with the following models:

- The Fanno property relations,
- The standard isentropic flow equations,
- The modified isentropic flow equations with the SRK EOS.

The errors between the measured and predicted pressure p_3 and temperature T_3 are given in Tables 21 and 22 for ∅ 5 and ∅ 3.2.
Regarding ∅ 5, the Fanno property relations performed the best in the prediction of p_3 and T_3 with the Haaland friction factor. The addition of SRK did not make any significant difference, where only a slight improvement was made using SRK in the prediction of p_3 with the Haaland friction factor. The Haaland friction factor performed better with the Fanno property relations, whereas the isentropic flow equations, including SRK, performed better with the Churchill friction factor.

Model	Haaland		Churchill	
	Error p_3 (kPa)	Error T_3 (K)	Error p_3 (kPa)	Error T_3 (K)
Fanno	152.7	121.1	1096.7	612.1
Isentropic	1313.0	121.1	216.6	612.1
Isentropic SRK	1311.3	121.3	216.6	612.5

Table 21: Absolute errors of p_3 and T_3 predictions compared to measurements for ∅ 5

A different result is found for ∅ 3.2. The SRK isentropic flow equations performed better, although slightly, for the predictions of p_3. The Churchill friction factor performed overall better for the predictions of p_3, but the Haaland friction factor performed significantly better for the predictions of T_3.

Model	Haaland		Churchill	
	Error p_3 (kPa)	Error T_3 (K)	Error p_3 (kPa)	Error T_3 (K)
Fanno	2244.7	13.5	1025.8	595.6
Isentropic	3828.7	13.5	990.4	595.6
Isentropic SRK	3828.0	13.5	986.0	596.1

Table 22: Absolute errors of p_3 and T_3 predictions compared to measurements for ∅ 3.2

Moving on to Figure 36, the Fanno property relations overlap largely with the measurements of p_3 for ∅ 5 when using the Haaland friction factor. In contrast, the Churchill friction factor shows a linear characteristic, thereby underestimating p_3 over the whole measured range of mass flow rates. Similarly for ∅ 3.2, where p_3 is also underestimated.

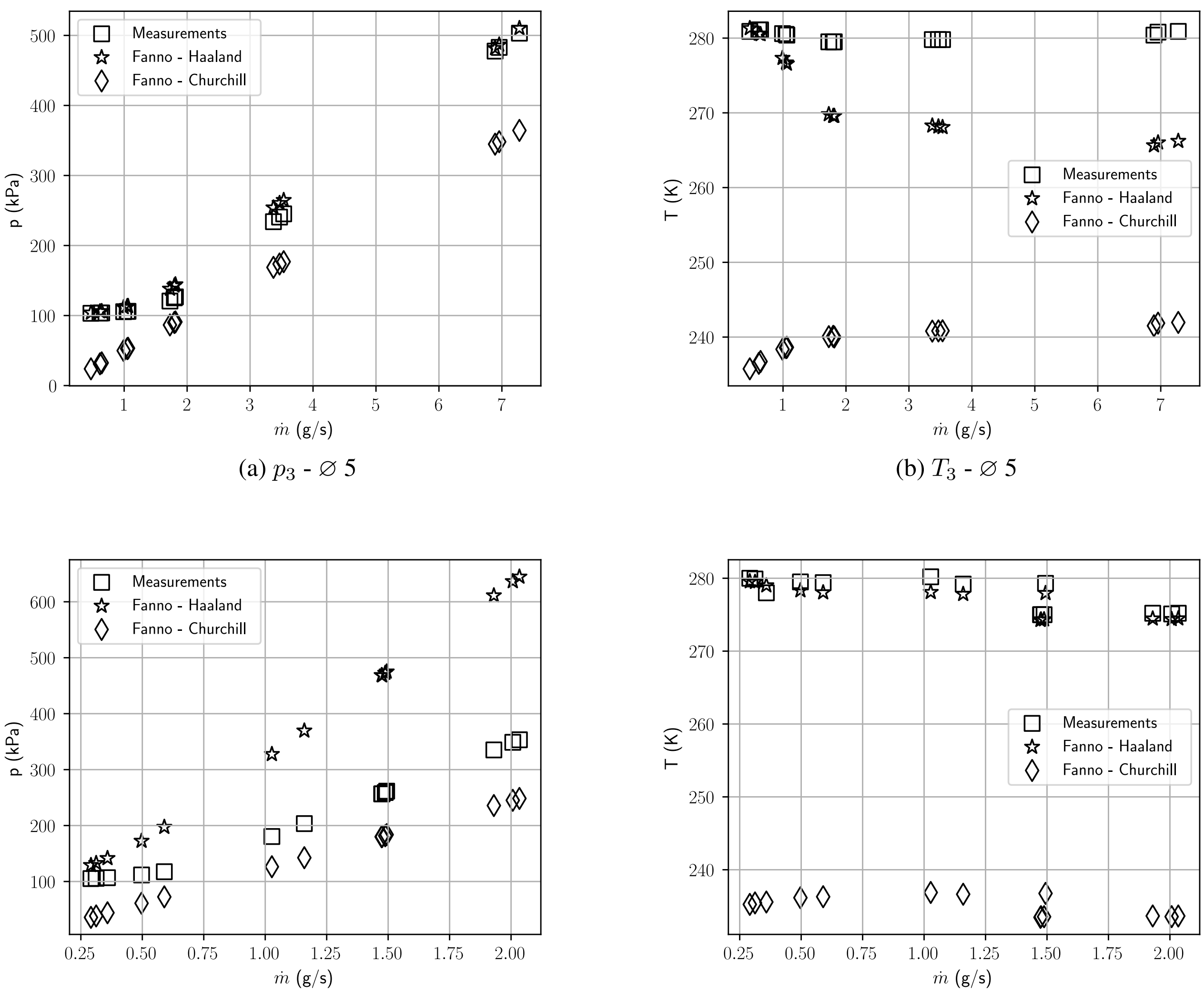

(a) p_3 - ∅ 5

(b) T_3 - ∅ 5

(c) p_3 - ∅ 3.2

(d) T_3 - ∅ 3.2

Figure 36: Comparison between measurements and the Fanno property relations for ∅ 5 and ∅ 3.2

Comparison of the results in Figures 36 and 37 reveals a new aspect of the Churchill friction factor. That is, the Churchill friction factor drastically decreased the critical length of the Fanno flow equation, thereby prematurely estimating a critical outlet state. Subsequently, p_3 and T_3 drastically reduce, also at low mass flow rates. However, this property is highly beneficial for isentropic flow equations, where the Churchill friction factor significantly improves the prediction of p_3. At the same time, this results in a drastic underestimation of T_3.

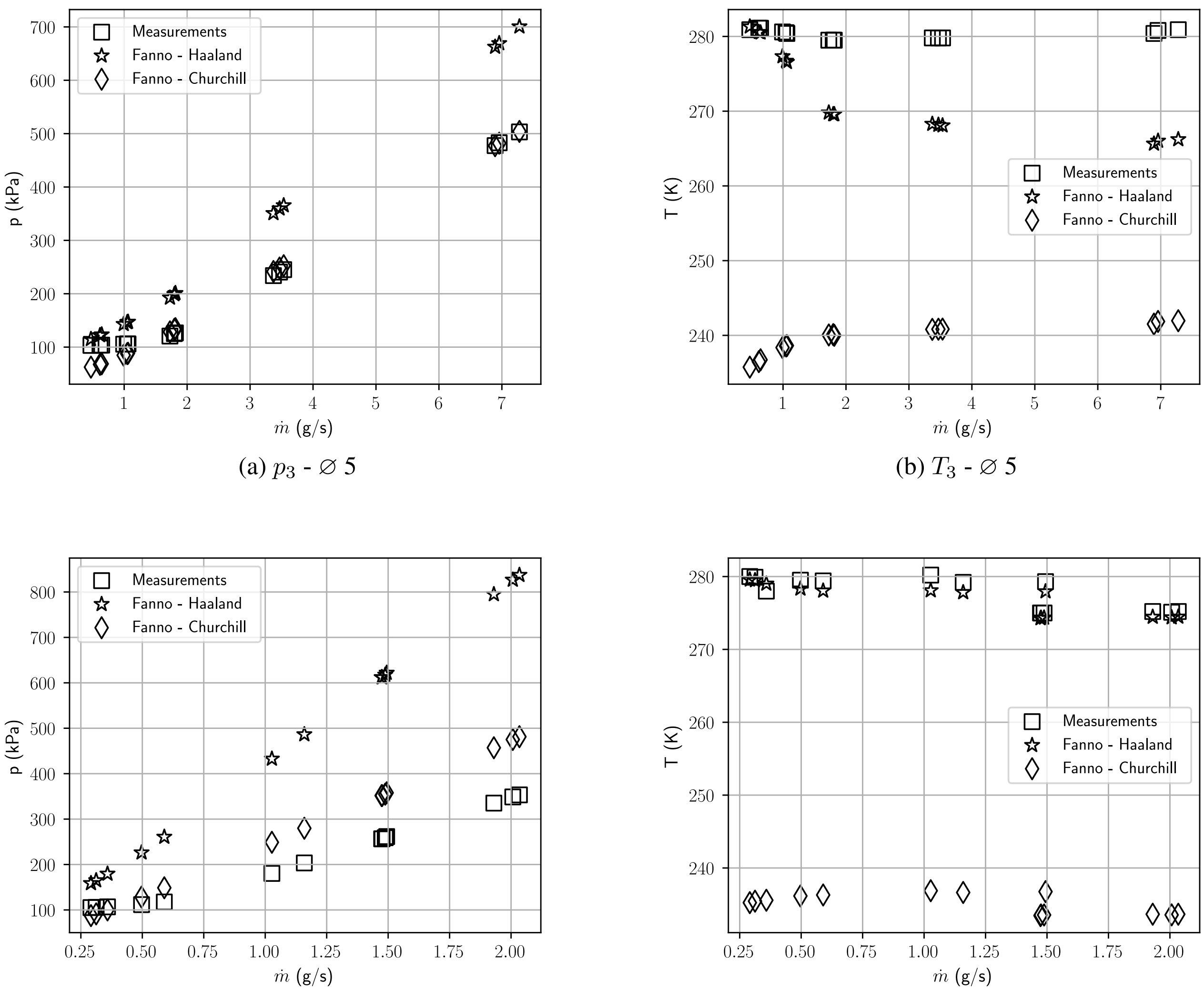

(a) p_3 - ∅ 5

(b) T_3 - ∅ 5

(c) p_3 - ∅ 3.2

(d) T_3 - ∅ 3.2

Figure 37: Comparison between measurements and the isentropic flow equations from Fanno flow for sensor location (3), using the Haaland–Churchill friction factor.

No further comparisons are provided for the measurements, the SRK model, and the standard isentropic flow equations. As shown in Tables 21 and 22, the predictions from both isentropic flow models differ only by a few Pascals and Kelvins. These differences are so small that the models appear nearly identical when plotted.

6.3 Numerical Models

A direct comparison between the numerical models and measurements is not straightforward. As both solvers relied on total inlet conditions for pressure and temperature, their respective static pressures reduced as the velocity increased over the iterations. The closest matching measurement is plotted along with the numerical models on the pipe length (x) to evaluate the flow characteristics in Figures 38, and 39.

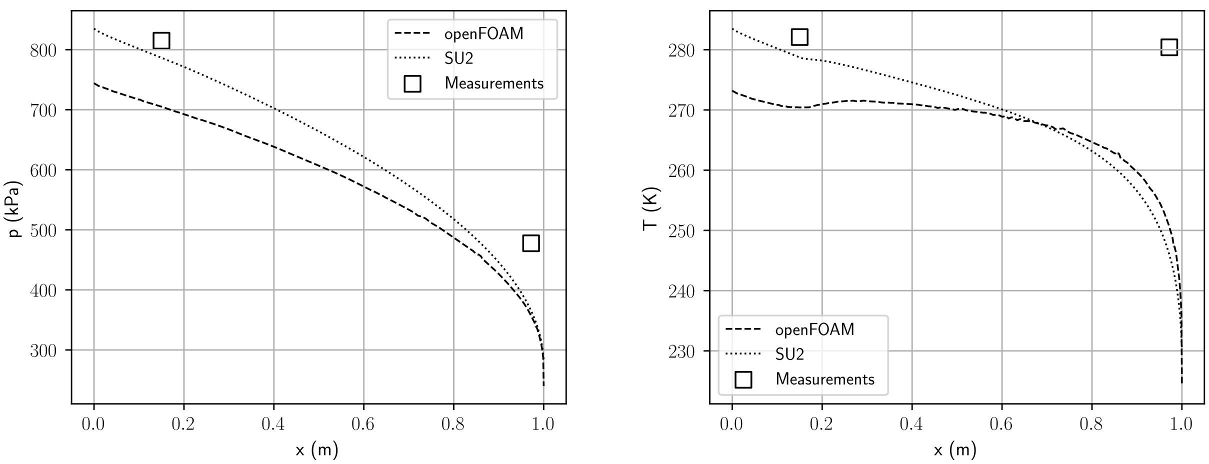

(a) Pressure over pipe length

(b) Temperature over pipe length

Figure 38: Comparison between openFOAM, SU2, and measurements

The pressure seems to agree to some extent with the numerical models, whereas the inlet temperature profile also aligns with the analytical models. However, the outlet temperature has shown major disagreement. Furthermore, the pressure profile appears to decay exponentially near the pipe outlet $x = 1$ m. Similar results were found for temperature measurements.
Continuing with the velocity profile along the pipe length:

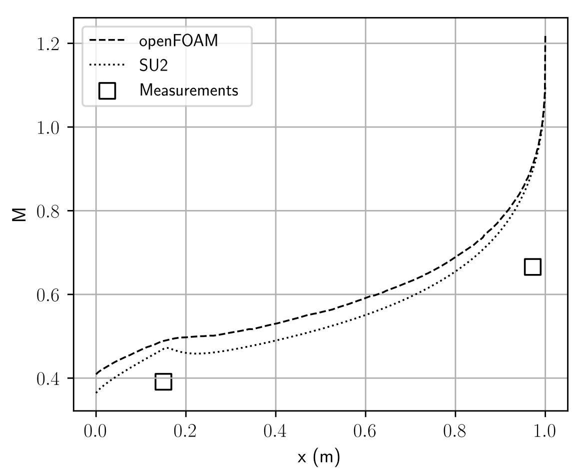

Figure 39: Mach number over pipe length

Both numerical models agree on a sonic condition at the pipe outlet. Furthermore, looking back at the results of Section 6.1, the steep asymptote seems to spoil its presence in measurements as well.

Finally, comparing the predicted mass flow rates of the numerical models, SU2 appears to show an overestimation of the mass flow rate, and OpenFOAM approaches closest to the measured values.

Model	Mass flow rate $\dot{m}$ g/s
openFOAM	6.744
SU2	7.799
Measurement	6.892

Table 23: Mass flow rate predictions of numerical models

Both solvers predicted a similar velocity profile over the length of the pipe, but SU2 computed both higher pressures and higher temperatures. Henceforth, the mass flow rate was also estimated to be higher.

6.4 Optical Imaging: Schadow Graphs

The following images were taken at the outlet of ∅ 3.2. The pressure throttle valve was gradually opened further in each image, thereby increasing the flow rate. There were no further sensor recorded during the capturing of these images.

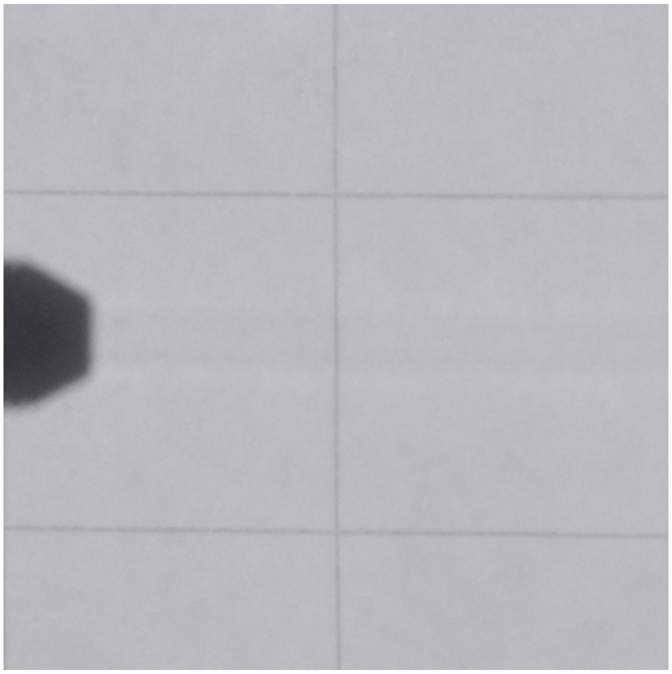

Figure 40: Regular outflow, no shocks present

Right after opening the throttling valve, a vague stream appears. A boundary emerges between the ambient air and gaseous hydrogen, exiting in a straight line before fading away.

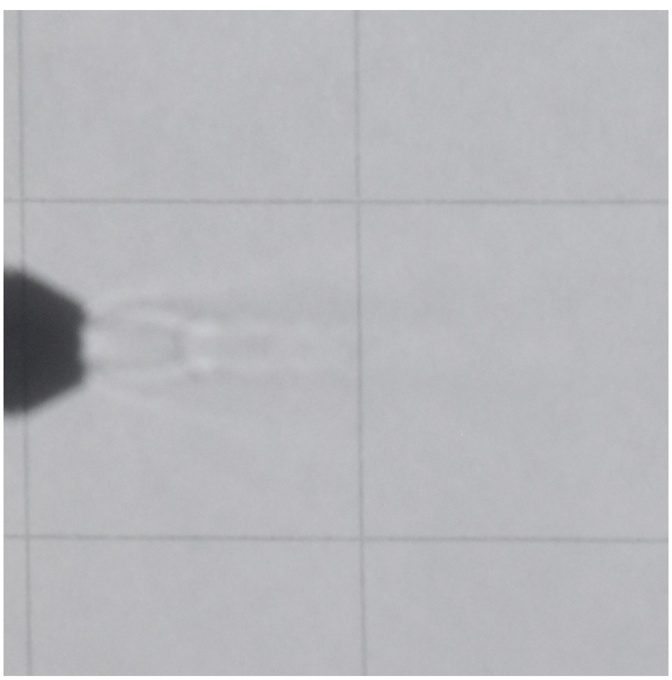

Figure 41: First barrel shock

Further opening the throttle results in the first appearance of a Mach disk, followed by a trail of pockets. Clear expansion waves show at the outer portion of the jet. In the inner jet, a similar picture as Figure 22 begins to show. The Mach number is computed using equation 4.8.

x_m	M
5.8 mm	4.8

Table 24: First barrel shock properties

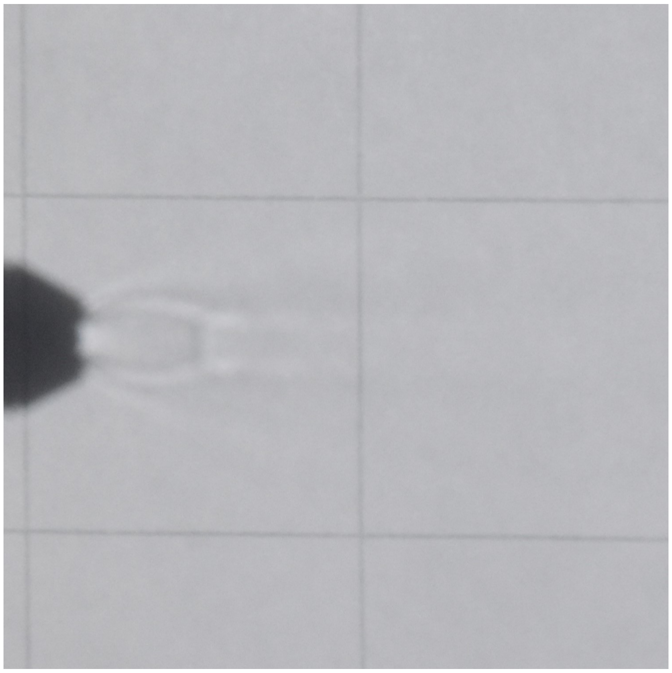

Figure 42: Second barrel shock

Nearing maximum flow, the Mach disk has moved further away from the pipe outlet, slightly steepening the angle of the expansion waves. The trail of the gas starts to fade sooner after the Mach disk

x_m	M
7.0 mm	5.2

Table 25: Second barrel shock properties

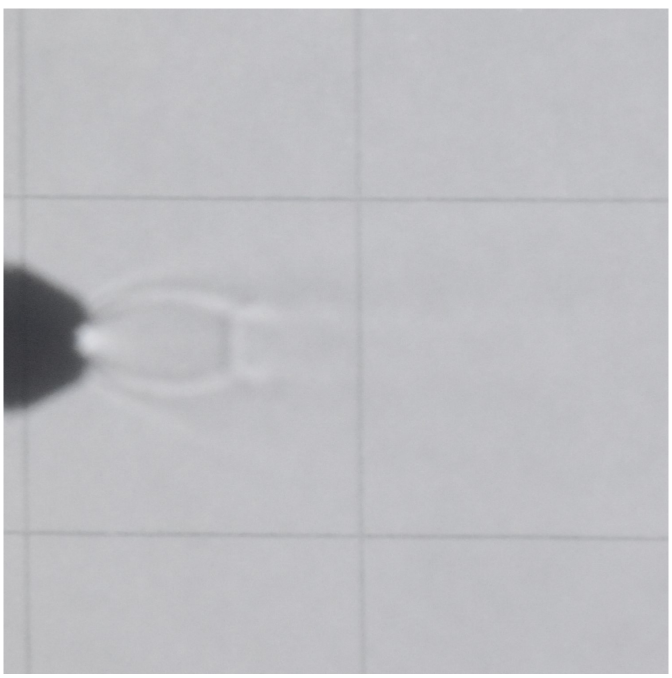

Figure 43: Third barrel shock

Maximum flow was achieved here, reaching 1 MPa at p_2. The Mach disk has moved slightly further from the outlet, and the trail has faded slightly further. Enormous flow velocities are found in the center of this bubble, reaching well beyond Mach 5.

x_m	M
9.3 mm	5.8

Table 26: Third barrel shock properties

7 Discussion

The main research question of this text is:

“How can analytical, empirical, and numerical models be used to approximate hydrogen flow in pipelines of varying diameter, and to what extent are they suitable to predict pressure and temperature under measured inlet conditions?”

To support the investigation of the main research question, the following conclusion on the sub-research questions were formulated:

1. ”What is the influence of pipeline diameter, and how do different diameters impact the performance of the modelling approaches?”

   Figures 29 to 31 have showed that the pressure and mass flow rate reflected a linear relationship in the experiments. Furthermore, the pressure-mass flow rate relation between $\varnothing$ 3.2 and $\varnothing$ 5 was on average 3.2, indicating that the pressure in a $\varnothing$ 5 pipe must increase approximately $3.2\times$ to accommodate the same mass flow rate in a $\varnothing$ 3.2 pipe.

   After converting the measurements to Mach and Reynolds numbers, an asymptotic relation was revealed in Figure 32b. Combining the results of the isentropic flow equations, optical images, and the asymptotic relations between Reynolds and Mach, the presence of this asymptote must have originated from the presence of a (close to) sonic outlet velocity.

   The measured outlet pressure and temperature showed more deviation from model predictions for $\varnothing$ 3.2 than for $\varnothing$ 5. Essentially, increasing the friction factor would be no use to improve predictions of the Fanno relation for $\varnothing$ 3.2. Also, including real gas effects made no significant improvement.

2. ”To what extent do analytical, empirical, and numerical models agree with experimentally measured outlet conditions, given known inlet conditions?”

   The Weymouth and Panhandle equations performed the worst from the considered models in prediction of the outlet pressure as they did not produce results for the considered range of mass flow rates.

   The Darcy-Weisbach equation is combination with the Churchill friction factor was the second best model for computing the outlet pressure.

   The Fanno property relations performed well overall. Here, the Chuchill friction factor underestimated the outlet pressure for the Fanno property relations, but gave noticeable improvement for the isentropic flow equations.

   Although there was no direct comparison between measurements and numerical models, they did provide a good impression for the investigated case of $\varnothing$ 5. As the numerical models were set up using total inlet boundary conditions, the static conditions were subjected to change as the velocity increased, leading to slight differences between the measurements and the CFD simulations.

3. ”How do analytical and empirical models compare with numerical models in predicting the outlet pressure and temperature of a pipe?”

   The use of CFD solvers was not straightforward in use for computing outlet conditions. Instead, a pressure difference was imposed at the pipe inlet and outlet, resulting in a mass flow rate. If the mass flow rate matches the desired conditions, the corresponding outlet pressure was found.

   The analytical and empirical models allowed for a simpler but accurate approach. Even though these models were implemented in Python scripts, the approach yielded results directly and showed satisfactory predictions.

   The Fanno property relations and the isentropic flow equations were in agreement with the CFD results regarding the outlet temperature. In the measurements, the thermocouple indicated only a slight difference when the mass flow rate was increased, whereas the models predicted a significant temperature drop.

The main research question is thereby concluded as follows:

Analytical, empirical, and numerical models each have their advantages in approximating hydrogen flow through pipelines of varying diameter. Their suitability for predicting pressure and temperature under known inlet conditions depends strongly on the experienced friction and flow velocity.
Empirical models such as the Weymouth and Panhandle equations showed limited predictions of the outlet pressure of the considered mass flow rates. Analytical models, particularly the Fanno property relations and isentropic flow equations combined with appropriate friction factor correlations (like Churchill or Haaland), provided significantly better agreement with experimental results. The Fanno model demonstrated reliable pressure predictions over the considered mass flow rates, especially for $\varnothing$ 5. For smaller diameters, such as $\varnothing$ 3.2, deviations between the model and measurements remained. This deviation could not be resolved by adjusting the friction factor or incorporating real gas effects, suggesting limitations in assumptions when non-ideal effects become even more dominant.
Numerical models offered more detailed insights, where the $\varnothing$ 5 pipe was investigated. Although no direct comparison was made with measurements due to differences in boundary conditions, the CFD simulations were in agreement with analytical predictions in terms of outlet temperature. However, the CFD approach required significantly more work to prepare.
In conclusion, analytical and empirical models offer a fast and reasonably accurate means of estimating outlet conditions in many practical scenarios, particularly when applying Fanno and isentropic formulations. Although the numerical models did not provide a direct method for predicting outlet conditions in the cases considered, they yielded deeper insights into the overall flow behaviour within the pipe.

8 Recommendations

Some recommendations are provided in this section on topic-specific topics. Firstly, regarding the use of real gas models:

1. Assessing the compressibility factor of gaseous hydrogen can offer preliminary insight into the need to use real gas models. As the conditions of this research had little to no deviations from the ideal gas law, thus $Z \approx 1$, there was no need to implement a real gas model.

2. During the investigation of real gas corrections for the isentropic flow equations, it was of interest to implement the Leachmann EOS instead of SRK. The Leachmann EOS is, as mentioned before, not very convenient to use, as it contains multiple summation terms and does not offer direct evaluation of pressure, temperature, or density. As the results pointed out that a real gas EOS did not make significant improvements over the ideal gas law for the considered pressures, it was abandoned. However, when facing significant non-ideal effects, it is recommended to implement the SRK EOS in the isentropic flow equations.

3. If SRK proves to be insufficient, the Leachmann EOS can also be implemented for this purpose, although it requires a more complex derivation due to the lengthiness of the expression.

Regarding recommendations on CFD:

1. For future work in CFD for similar cases, SU2 is recommended. It showed during simulations to be much more stable then openFOAM.

2. This work did not include mesh refinements due to time constraints, which is highly recommended to further investigate the accuracy of CFD solvers and hydrogen flows.

3. At this moment, SU2 does not offer an EOS specifically for gaseous hydrogen. For cases where gaseous hydrogen is studied at higher pressures and high velocities, it is recommended to investigate the implementation of the Leachmann EOS in SU2.

4. The Kolmogorov length scale indicated a requirement of one-order finer inflation layers. As a result, the mesh obtains a large amount of extra cells to retain appropriate growth ratio's between cells. Although it requires more computational load, a DNS simulation could be performed on slightly smaller pipes to properly assess the velocity profile. In turn, the velocity profile can be used to analyse the validity of friction factors, hydrodynamical smoothness, and many other aspects. Furthermore, outlet pressure predictions for $\varnothing$ 3.2 remained overestimated, which could be investigated further with more advanced CFD approaches like DNS.

Recommendations on conduction measurements with an experimental set-up and gaseous hydrogen:

1. In this experimental setup, thermocouples were placed on the side of the test subjects with diameters $\varnothing$ 3.2 and $\varnothing$ 5. Since CFD simulations, isentropic flow equations, and Fanno flow relations all predicted noticeably lower outlet temperatures, it is recommended that future temperature measurements are evaluated at both the pipe wall and taken directly within the gas stream to assess the temperature profile.

2. The thermocouples used in this study had a stated accuracy of ± 1.4 K. If future investigations confirm that the temperature profile within the pipe is uniform, it will be necessary to use thermocouples with tighter tolerances, as the current sensors were operating at the limits of their specified accuracy.

References

[1] General Secretariat of the Council of the EU. Alternative fuels infrastructure: Council adopts new law for more recharging and refuelling stations across europe. *European Council*, Jul 2023. URL https://www.consilium.europa.eu/en/press/press-releases/2023/07/25/alternative-fuels-infrastructure-council-adopts-new-law-for-more-recharging-and-refuelling-sta pdf/.

[2] European Commission. TEN-T Schematic Map. https://transport.ec.europa.eu/document/download/3f55bcf7-d2cf-4244-bbf1-fc4f132115ad_en?filename=TEN_T_Schematic_map.pdf, 2024. Directorate-General for Mobility and Transport.

[3] Hydrogen refuelling stations | European Hydrogen Observatory, 2024. URL https://observatory.clean-hydrogen.europa.eu/hydrogen-landscape/distribution-and-storage/hydrogen-refuelling-stations.

[4] M. Genovese and P. Fragiacomo. Hydrogen refueling station: Overview of the technological status and research enhancement. *Journal of Energy Storage*, 61:106758, 2023. ISSN 2352-152X. doi: https://doi.org/10.1016/j.est.2023.106758. URL https://www.sciencedirect.com/science/article/pii/S2352152X2300155X.

[5] MobilityPlaza. A new dawn for hydrogen mobility in europe. https://www.mobilityplaza.org/news/32614, April 2023. URL https://www.mobilityplaza.org/news/32614. Published ca. April 2023; Europe had 254 hydrogen stations in 2022, etc.

[6] Hydrogen Europe. A new dawn for H_2 mobility in eu. https://hydrogeneurope.eu/a-new-dawn-for-h2-mobility-in-eu/, April 2023. URL https://hydrogeneurope.eu/a-new-dawn-for-h2-mobility-in-eu/. Published ca. April 2023; "around 700 more stations will have to be introduced… according to Hydrogen Europe.".

[7] H2.LIVE. Hydrogen stations in germany & europe – h2.live. https://h2.live/en/, 2025. URL https://h2.live/en/. Real-time map and live data of public hydrogen refuelling stations in Europe. Accessed June 2025.

[8] Pobitra Halder, Meisam Babaie, Farhad Salek, Nawshad Haque, Russell Savage, Svetlana Stevanovic, Timothy A. Bodisco, and Ali Zare. Advancements in hydrogen production, storage, distribution and refuelling for a sustainable transport sector: Hydrogen fuel cell vehicles. *International Journal of Hydrogen Energy*, 52:973–1004, 2024. ISSN 0360-3199. doi: https://doi.org/10.1016/j.ijhydene.2023.07.204. URL https://www.sciencedirect.com/science/article/pii/S0360319923036868.

[9] T. Bourgeois, F. Ammouri, D. Baraldi, and P. Moretto. The temperature evolution in compressed gas filling processes: A review. *International Journal of Hydrogen Energy*, 43(4):2268–2292, 2018. ISSN 0360-3199. doi: https://doi.org/10.1016/j.ijhydene.2017.11.068. URL https://www.sciencedirect.com/science/article/pii/S0360319917343860.

[10] Taichi Kuroki, Kazunori Nagasawa, Michael Peters, Daniel Leighton, Jennifer Kurtz, Naoya Sakoda, Masanori Monde, and Yasuyuki Takata. Thermodynamic modeling of hydrogen fueling process from high-pressure storage tank to vehicle tank. *International Journal of Hydrogen Energy*, 46(42):22004–22017, 2021. ISSN 0360-3199. doi: https://doi.org/10.1016/j.ijhydene.2021.04.037. URL https://www.sciencedirect.com/science/article/pii/S0360319921013410.

[11] H. Ebne-Abbasi, D. Makarov, and V. Molkov. Cfd model of refuelling through the entire equipment of a hydrogen refuelling station. *International Journal of Hydrogen Energy*, 53:200–207, 2024. ISSN 0360-3199. doi: https://doi.org/10.1016/j.ijhydene.2023.12.056. URL https://www.sciencedirect.com/science/article/pii/S0360319923063565.

[12] Aashna Raj, I.A. Sofia Larsson, Anna-Lena Ljung, Tobias Forslund, Robin Andersson, Joel Sundström, and T.Staffan Lundström. Evaluating hydrogen gas transport in pipelines: Current state of numerical and experimental methodologies. *International Journal of Hydrogen Energy*, 67:136–149, 2024. ISSN 0360-3199. doi: https://doi.org/10.1016/j.ijhydene.2024.04.140. URL https://www.sciencedirect.com/science/article/pii/S0360319924014137.

[13] B. Thawani, R. Hazael, and R. Critchley. Assessing the pressure losses during hydrogen transport in the current natural gas infrastructure using numerical modelling. *International Journal of Hydrogen Energy*, 48(88):34463–34475, 2023. ISSN 0360-3199. doi: https://doi.org/10.1016/j.ijhydene.2023.05.208. URL https://www.sciencedirect.com/science/article/pii/S036031992302548X.

[14] SAE International. SAE J2601: Fueling Protocols for Light Duty Gaseous Hydrogen Surface Vehicles. https://www.sae.org/standards/content/j2601/, February 2024. Issued February 2024.

[15] Resato High Pressure Technology. Resato headquarters in assen, 2024. URL https://www.resato.com. Accessed: 2025-06-08.

[16] John D. Anderson, Jr. *Modern compressible flow: with historical perspective*. McGraw-Hill Education, 7 2002.

[17] Johann Nikuradse et al. Laws of flow in rough pipes. 1950.

[18] Robert P. Benedict. *Fundamentals of pipe flow*. 1 1980. URL http://ci.nii.ac.jp/ncid/BA03041788.

[19] Srbislav Genic, Ivan Aranđelović, Petar Kolendić, Marko Jarić, Nikola Budimir, and Vojislav Genić. A review of explicit approximations of colebrook's equation. 06 2011.

[20] Thomas Adams, Christopher Grant, and Heather Watson. A Simple Algorithm to Relate Measured Surface Roughness to Equivalent Sand-grain Roughness. *International Journal of Mechanical Engineering and Mechatronics*, 1 2012. doi: 10.11159/ijmem.2012.008. URL https://doi.org/10.11159/ijmem.2012.008.

[21] Crane Co. *Flow of Fluids Through Valves, Fittings, and Pipe*. Crane Co., 300 Park Avenue, New York, N.Y. 10022, metric edition, 1982. Metric Edition.

[22] Liang biao Ouyang and Khalid Aziz. Steady-state gas flow in pipes. *Journal of Petroleum Science and Engineering*, 14(3):137–158, 1996. ISSN 0920-4105. doi: https://doi.org/10.1016/0920-4105(95)00042-9. URL https://www.sciencedirect.com/science/article/pii/0920410595000429.

[23] R. Hagmeijer. Fluid mechanics i, March 2021. Lecture notes.

[24] Yunus A. Çengel and John M. Cimbala. *Fluid Mechanics: Fundamentals and Applications*. McGraw-Hill Education, New York, 3 edition, 2014. ISBN 978-0-07-338032-2.

[25] Sun Bai-gang, Zhang Dong-sheng, and Liu Fu-shui. A new equation of state for hydrogen gas. *International Journal of Hydrogen Energy*, 37(1):932–935, 2012. ISSN 0360-3199. doi: https://doi.org/10.1016/j.ijhydene.2011.03.157. URL https://www.sciencedirect.com/science/article/pii/S036031991100783X. 11th China Hydrogen Energy Conference.

[26] Jacob Leachman, Bryce Jacobson, Steven Penoncello, and Eric Lemmon. Fundamental equations of state for parahydrogen, normal hydrogen, and orthohydrogen, 2009-09-04 00:09:00 2009. URL https://tsapps.nist.gov/publication/get_pdf.cfm?pub_id=832374.

[27] Eric W. Lemmon, Marcia L. Huber, Jacob W. Leachman, National Institute of Standards, Technology, and University of Wisconsin-Madison Cryogenics Lab. Revised Standardized Equation for Hydrogen Gas Densities for Fuel Consumption Applications. Technical Report 6, 11 2008. URL `https://nvlpubs.nist.gov/nistpubs/jres%5C113%5C6%5CV113.N06.A05.pdf`.

[28] N. Diepstraten, L.M.T. Somers, and J.A. van Oijen. Numerical characterization of high-pressure hydrogen jets for compression–ignition engines applying real gas thermodynamics. *International Journal of Hydrogen Energy*, 79:22–35, 2024. ISSN 0360-3199. doi: https://doi.org/10.1016/j.ijhydene.2024.06.325. URL `https://www.sciencedirect.com/science/article/pii/S0360319924025643`.

[29] Giorgio Soave. Equilibrium constants from a modified redlich–kwong equation of state. *Chemical Engineering Science*, 27(6):1197–1203, 1972. doi: 10.1016/0009-2509(72)80096-4.

[30] D. A. Kouremenos and K. A. Antonopoulos. Isentropic exponents of real gases and application for the air at temperatures from 150 k to 450 k. *Acta Mechanica*, 65:81–99, 1986. Received January 20, 1986.

[31] Hermann Schlichting. *Boundary-Layer Theory*. McGraw-Hill Book Company, New York, 7th edition, 1979.

[32] David C. Wilcox. *Turbulence Modeling for CFD*. DCW Industries, Inc., La Cañada, California, 3rd edition, 2006. ISBN 978-1-928729-08-2.

[33] B. E. Launder and D. B. Spalding. The numerical computation of turbulent flows. *Computer Methods in Applied Mechanics and Engineering*, 3:269–289, 1974.

[34] David C. Wilcox. Reassessment of the scale-determining equation for advanced turbulence models. *AIAA Journal*, 26(11):1299–1310, 1988.

[35] Florian R. Menter. Two-equation eddy-viscosity turbulence models for engineering applications. *AIAA Journal*, 32(8):1598–1605, 1994. doi: 10.2514/3.12149.

[36] Joel H. Ferziger and Milovan Perić. *Computational Methods for Fluid Dynamics*. Springer, Berlin, Heidelberg, 3rd edition, 2002. ISBN 978-3-540-42074-3.

[37] S. V. Patankar and D. B. Spalding. A calculation procedure for heat, mass and momentum transfer in three-dimensional parabolic flows. *International Journal of Heat and Mass Transfer*, 15(10):1787–1806, 1972. doi: 10.1016/0017-9310(72)90054-3.

[38] R. I. Issa. Solution of the implicitly discretized fluid flow equations by operator-splitting. *Journal of Computational Physics*, 62(1):40–65, 1986.

[39] F. Moukalled, L. Mangani, and M. Darwish. *The Finite Volume Method in Computational Fluid Dynamics: An Advanced Introduction with OpenFOAM and Matlab*, volume 113 of *Fluid Mechanics and Its Applications*. Springer, Cham, 2016. ISBN 978-3-319-16874-6. doi: 10.1007/978-3-319-16874-6.

[40] Christopher J. Greenshields and Henry G. Weller. *Notes on Computational Fluid Dynamics: General Principles*. CFD Direct Ltd, Reading, UK, 2022. ISBN 978-1-3999-2078-0.

[41] S. L. R. Ellison and A. Williams, editors. *Quantifying Uncertainty in Analytical Measurement*. Eurachem/CITAC, United Kingdom, 3rd edition, 2012. CITAC Guide Number 4.

[42] Xiao Qin, Xudong Xiao, Ishwar K. Puri, and Suresh K. Aggarwal. Effect of varying composition on temperature reconstructions obtained from refractive index measurements in flames. *Combustion and Flame*, 128:121–132, 2002. doi: 10.1016/S0010-2180(01)00338-8.

[43] Cameron Tropea, Alexander L. Yarin, and John F. Foss, editors. *Handbook of Experimental Fluid Mechanics*. Springer, Berlin, Heidelberg, 2007. ISBN 978-3-540-25141-5. doi: 10.1007/978-3-540-30299-5.

[44] S. Crist, D. R. Glass, and P. M. Sherman. Study of the highly underexpanded sonic jet. *AIAA Journal*, 4(1): 68–71, 1966. doi: 10.2514/3.3386.

[45] ANSYS, Inc. *ANSYS Fluent User's Guide, Release 2024 R1*. ANSYS, Inc., 2024. URL https://ansyshelp.ansys.com/public/account/secured?returnurl=/Views/Secured/corp/v251/en/flu_ug/flu_ug_sec_turb_setup_init.html. Equation 15-6, accessed on June 2, 2025.

A TEN-T Network

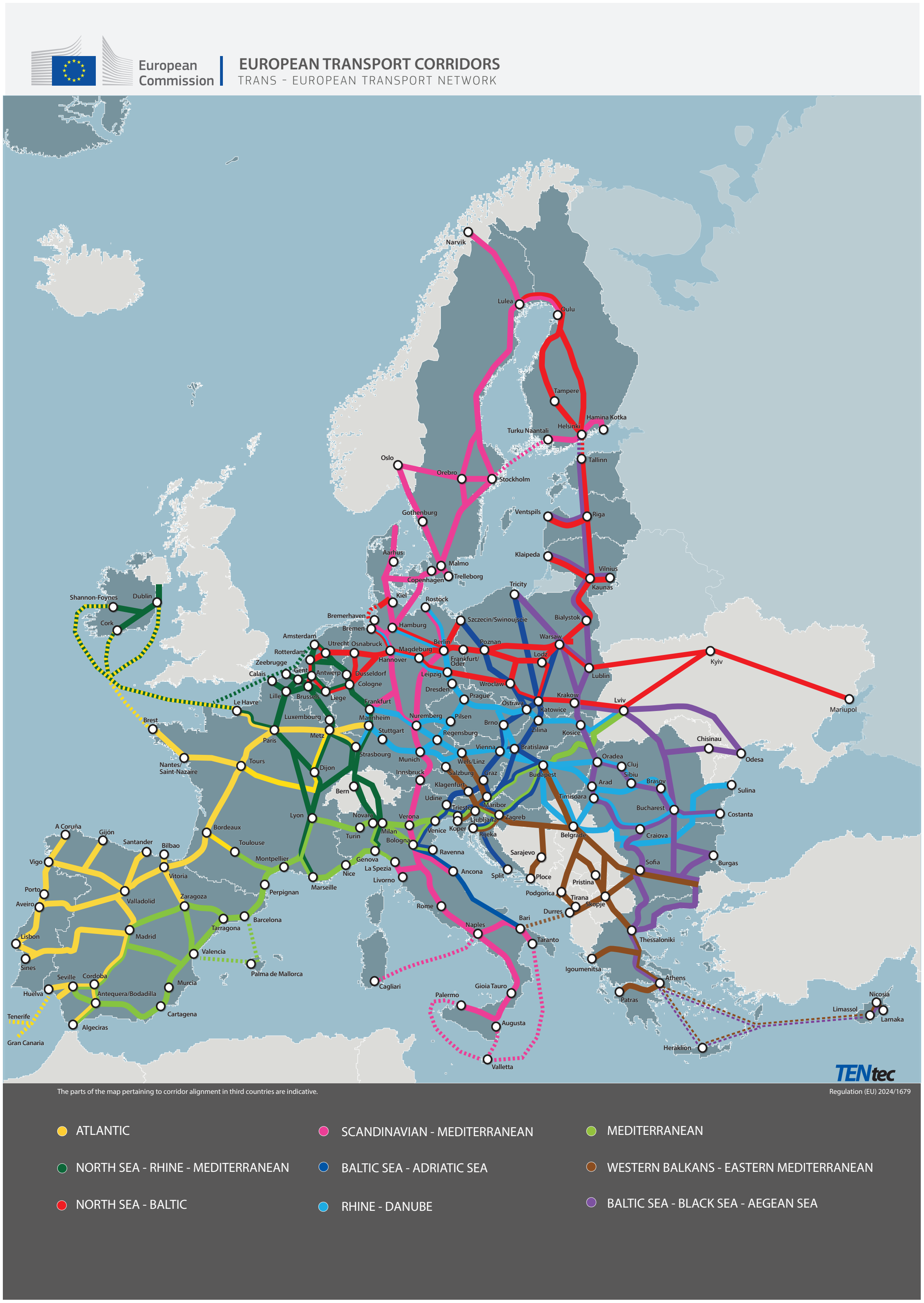

Figure 44: TEN-T Schematic Map [2].

B Order analysis

Before continuing to analytical, empirical, and numerical methods to model the flow for the geometries mentioned previously, it is insightful to preform a order analysis on the governing equations. As will be shown in this section, an order analysis demonstrates with minimal information what quantities dominate the flow characteristics. Firstly, the justification of diameter dominance is presented, next, the energy equation is analyzed on the assumption of adiabatic flow. Finally, a conclusion is made on the relevant methods required to do a qualitative modeling approach.
Consider the continuity equation:

$$\frac{\partial \rho}{\partial t} + \frac{\partial \rho u_j}{\partial x_j} = 0 \tag{B.1}$$

This analysis is scoped to a steady flow. Furthermore, consider that the flow is moving with a velocity below $M < 0.3$. Hence, the density fluctuations are neglected, and the incompressible Navier-Stokes equations are found for steady flow.

$$\frac{\partial u}{\partial x} + \frac{\partial v}{\partial y} = 0 \tag{B.2}$$

The cautious reader might argue why an analysis with constant density is relevant. To answer this question, consider that the density gradient over a complete (hydrogen refueling) system is in fact large, but if we only consider a single component, the density gradient is much smaller. Additionally, at low velocities, the same assumption holds. For the remainder of this subsection, introduce the following dimensionless quantities:

$$x = x^* L, \qquad y = y^* D, \qquad u = u^* U_\infty, \qquad v = v^* V_\infty, \qquad p = p^* \rho U^2 \tag{B.3}$$

Here, L represents the length of the pipe, and D the diameter. Furthermore, the velocities U_∞ and V_∞ represent the velocity of the fluid at the center-line through a pipe. Substituting these expressions into the continuity equation gives:

$$\frac{\partial u^* U_\infty}{\partial x^* L} + \frac{\partial v^* V_\infty}{\partial y^* D} = 0 \tag{B.4}$$

Rearranging this equation:

$$\boxed{\frac{U_\infty D}{V_\infty L}\frac{\partial u^*}{\partial x^*} + \frac{\partial v^*}{\partial y^*} = 0} \tag{B.5}$$

This equations shows an important result. Namely, the continuity equation can only hold if the terms $\frac{\partial u^*}{\partial x^*}$ and $\frac{\partial v^*}{\partial y^*}$ are in the same order. Henceforth, so should the constants that appear in front of the term ($\frac{U_\infty}{L}$ and $\frac{V_\infty}{D}$). This indicates that the term $\frac{U_\infty D}{V_\infty L} \simeq 1$.
Continuing the analysis with the Navier-Stokes equations:

$$\frac{\partial \rho u_i}{\partial t} + \frac{\partial}{\partial x_j}(\rho u_i u_j) - \frac{\partial \sigma_{ij}}{\partial x_j} - \rho g_i = 0 \tag{B.6}$$

The Navier-Stokes equations are reduced with the same assumptions introduced previously (steady, two-dimensional):

$$\rho u_j \frac{\partial u_i}{\partial x_j} - \frac{\partial \sigma_{ij}}{\partial x_j} - \rho g_i = 0 \tag{B.7}$$

The stress tensor, σ_{ij} is defined as:

$$\sigma_{ij} = -p\delta_{ij} + \tau_{ij} \tag{B.8}$$

The δ_{ij} is the Kronecker delta. The viscous stress tensor, τ_{ij}, is defined as:

$$\tau_{ij} = \mu(\frac{\partial u_i}{\partial x_j} + \frac{\partial u_j}{\partial x_i}) \tag{B.9}$$

Now, reduce the stress tensor σ_{ij} with the assumptions made (incompressible):

$$\frac{\partial \sigma_{ij}}{\partial x_j} = -\frac{\partial p \delta_{ij}}{\partial x_j} + \frac{\partial}{\partial x_j}\left[\mu\left(\frac{\partial u_j}{\partial x_i} + \frac{\partial u_i}{\partial x_j}\right)\right] = -\frac{\partial p}{\partial x_i} + \mu\left[\frac{\partial^2 u_i}{\partial x_j \partial x_j} + \frac{\partial}{\partial x_i}\left(\frac{\partial u_j}{\partial x_j}\right)\right] \tag{B.10}$$

Hence, we can recognize mass conservation in the last term, ultimately reducing the equation to:

$$\frac{\partial u_i u_j}{\partial x_j} + \frac{1}{\rho}\frac{\partial p}{\partial x_i} + \nu\frac{\partial^2 u_i}{\partial x_j \partial x_j} - g_i = 0 \tag{B.11}$$

And expanding the derivatives,

$$u_i\frac{\partial u_j}{\partial x_j} + u_j\frac{\partial u_i}{\partial x_j} + \frac{1}{\rho}\frac{\partial p}{\partial x_i} + \nu\frac{\partial^2 u_i}{\partial x_j \partial x_j} - g_i = 0 \tag{B.12}$$

For ease of explanation, only consider the x-direction and two-dimensional flow,

$$u\left[\frac{\partial u}{\partial x} + \frac{\partial v}{\partial y}\right] + u\frac{\partial u}{\partial x} + v\frac{\partial u}{\partial y} + \frac{1}{\rho}\frac{\partial p}{\partial x} + \nu\left[\frac{\partial^2 u}{\partial x \partial x} + \frac{\partial^2 u}{\partial y \partial y}\right] + g_x = 0 \tag{B.13}$$

Hence, the gravity term leaves the equation due to the choice of direction. Furthermore, the steady and incompressible continuity equation can be recognized in the first term, also leaving the equation.

$$u\frac{\partial u}{\partial x} + v\frac{\partial u}{\partial y} + \frac{1}{\rho}\frac{\partial p}{\partial x} + \nu\left[\frac{\partial^2 u}{\partial x \partial x} + \frac{\partial^2 u}{\partial y \partial y}\right] = 0 \tag{B.14}$$

Next, substitute the relations for the dimensionless quantities (equation B.3):

$$u^* U_\infty \frac{\partial u^* U_\infty}{\partial x^* L} + v^* V_\infty \frac{\partial u^* U_\infty}{y^* D} + \frac{1}{\rho}\frac{\partial p^* \rho U_\infty^2}{\partial x^* L} + \nu\left[\frac{\partial^2 u^* U_\infty}{\partial x * L \partial x * L} + \frac{\partial^2 u^* U_\infty}{\partial y^* D \partial y^* D}\right] = 0 \tag{B.15}$$

Rewriting this equation gives:

$$u^* \frac{U_\infty^2}{L}\frac{\partial u^*}{\partial x^*} + v^* \frac{V_\infty U_\infty}{D}\frac{\partial u^*}{\partial y^*} + \frac{U_\infty^2}{L}\frac{\partial p^*}{\partial x^*} + \nu\left[\frac{U_\infty}{L^2}\frac{\partial^2 u^*}{\partial x^{*2}} + \frac{U_\infty}{D^2}\frac{\partial^2 u^*}{\partial y^{*2}}\right] = 0 \tag{B.16}$$

Multiplying the entire equation with $\frac{L}{U_\infty^2}$ simplifies the equation to

$$u^* \frac{\partial u^*}{\partial x^*} + v^* \frac{V_\infty L}{U_\infty D}\frac{\partial u^*}{\partial y^*} + \frac{\partial p^*}{\partial x^*} + \nu\left[\frac{1}{UL}\frac{\partial^2 u^*}{\partial x^{*2}} + \frac{L}{U_\infty D^2}\frac{\partial^2 u^*}{\partial y^{*2}}\right] = 0 \tag{B.17}$$

Recognizing the term $\frac{V_\infty L}{U_\infty D} \simeq 1$ as found in the analysis of the continuity equation, and regrouping the right hand side terms,

$$\boxed{u^* \frac{\partial u^*}{\partial x^*} + v^* \frac{\partial u^*}{\partial y^*} + \frac{\partial p^*}{\partial x^*} + \underbrace{\frac{\nu}{U_\infty D}}_{\frac{1}{Re}}\left[\underbrace{\frac{D}{L}}_{<<1}\frac{\partial^2 u^*}{\partial x^{*2}} + \underbrace{\frac{L}{D}}_{>>1}\frac{\partial^2 u^*}{\partial y^{*2}}\right] = 0} \tag{B.18}$$

This is an important result, namely, simply inserting the chosen expressions with dimensionless quantities shows that the Navier-Stokes equations reduce to an expression containing the Reynolds number ($\frac{U_\infty D}{\nu}$). The Reynolds term contains a characteristic length, which in this analysis is indicated (as widely known) as the diameter D for a pipe flow. Hence, the flow is characterized by its diameter.

C Leachman's Equation of State

The Leachmann equation of state (EoS) is a reduced Helmholtz free energy model. The NIST EoS referenced earlier (equation 2.36) is essentially a simplified approximation of the Leachmann EoS, reformulated in terms of the compressibility factor for ease of use. However, the NIST EoS is less suitable for analytical derivation of thermodynamic derivatives such as $\gamma_{T\nu}$ and $\gamma_{p\nu}$. Therefore, in this analysis, we adopt the Leachmann EoS.
The roadmap for the derivation is as follows:

1. Derive an expression for pressure from the Leachmann EoS.
2. From this pressure expression, derive the partial derivatives $\left(\frac{\partial p}{\partial \nu}\right)_T$ and $\left(\frac{\partial p}{\partial T}\right)_\nu$

The Leachmann EoS is divided into an ideal gas and a residual contribution, given by $\alpha = \alpha^0 + \alpha^r$.

$$\alpha^0(\tau, \delta) = \ln \delta + 1.5 \ln \tau + a_1 + a_2 \tau + \sum_{k=3}^{N} a_k \ln \left[1 - e^{-b_k^{p_i}}\right] \tag{C.1}$$

$$\alpha^r(\tau, \delta) = \sum_{i=1}^{l} N_i \delta^{d_i} \tau^{t_i} + \sum_{i=l+1}^{m} N_i \delta^{d_i} \tau^{t_i} e^{-\delta^{p_i}} + \sum_{i=m+1}^{n} N_i \delta^{d_i} \tau^{t_i} e^{\varphi_i (\delta - D_i)^2 + \beta_i (\tau - \gamma_i)^2} \tag{C.2}$$

The constants N_i, t_i, d_i, and p_i are specified by Leachman et al. [26] for para-, ortho-, and normal-hydrogen. For details on these constants and the equation of state, please refer to the publicly accessible publication. Furthermore, δ and τ are the reduced density and temperature:

$$\delta = \frac{\rho}{\rho_c}, \quad \tau = \frac{T_c}{T} \tag{C.3}$$

The following steps must be undertaken to implement it in the isentropic flow equations:

- As the Leachmann EOS is a Helmholtz free energy formulation, derive the pressure by using the thermodynamic relation:

$$p = -\left(\frac{\partial A}{\partial V}\right)_T \tag{C.4}$$

- The expression found for p can now be used to derive $\gamma_{p\nu}$ and $\gamma_{T\nu}$:

$$\gamma_{T\nu} = 1 + \frac{\nu}{c_v} \left(\frac{\partial p}{\partial T}\right)_\nu \tag{C.5}$$

$$\gamma_{p\nu} = 1 + \frac{\nu}{c_v} \left(\frac{\partial p}{\partial \nu}\right)_\nu = 1 - \frac{\rho}{c_v} \left(\frac{\partial p}{\partial \rho}\right)_T \tag{C.6}$$

Finally, subsitute the expressions found for γ_{T_ν} and γ_{p_ν} into Equations 2.46 2.47 2.48.

D Favre and Reynolds-Averaging in compressible flow

To investigate how Favre averaging can be beneficial to Reynolds averaging, this appendix provides an example in which both averaging techniques are used on the Navier-Stokes equations.

$$\frac{\partial \rho u_i}{\partial t} + \frac{\partial \rho u_i u_j}{\partial x_j} - \frac{\partial \sigma_{ij}}{\partial x_j} - \rho g_j = 0 \tag{D.1}$$

where $\sigma_{ij} = -p\delta_{ij} + S_{ij}$. Neglecting gravity and rearranging the terms yields

$$\frac{\partial \rho u_i}{\partial t} + \frac{\partial \rho u_i u_j}{\partial x_j} = -\frac{\partial p}{\partial x_i} + \frac{\partial}{\partial x_j}\left(2\mu S_{ij}\right) \tag{D.2}$$

where $S_{ij} = \frac{1}{2}\left(\frac{\partial u_j}{\partial x_j} + \frac{\partial u_i}{\partial x_j}\right)$. Starting with Reynolds decomposition:

$$\phi = \bar{\phi} + \phi' \tag{D.3}$$

where ϕ is an arbitrary flow property, $\bar{\phi}$ is an averaged flow property, and ϕ' is the Reynolds fluctuating property.

Starting with an incompressible case with constant density and viscosity, the Navier-Stokes equations reduce to:

$$\rho\frac{\partial u_i}{\partial t} + \rho\frac{\partial}{\partial x_j}(u_j u_i) = -\frac{\partial p}{\partial x_i} + \frac{\partial}{\partial x_j}(2\mu S_{ji}) \tag{D.4}$$

Subsequently, Reynolds-Averaging this equation using the decompositions $u = \bar{u} + u'$ and $p = \bar{p} + p'$:

$$\rho\frac{\partial \bar{u}_i}{\partial t} + \rho\frac{\partial}{\partial x_j}(\overline{u_i u_j}) + \underbrace{\frac{\partial}{\partial x_j}(\rho\overline{u_j' u_i'})}_{\text{Reynolds stress tensor}} = -\frac{\partial \bar{p}}{\partial x_i} + \frac{\partial}{\partial x_j}(2\mu S_{ji}) \tag{D.5}$$

If compressibility effects are encountered, the density should also be treated with Reynolds decomposition ($\rho = \bar{\rho} + \rho'$).

$$\frac{\partial}{\partial t}(\overline{\rho u_i} + \overline{\rho' u_i'}) + \frac{\partial}{\partial x_j}(\bar{\rho}\bar{u}_i\bar{u}_j + \bar{\rho}\overline{u_i' u_j'} + \overline{\rho' u_i'}\bar{u}_j + \overline{\rho'}\bar{u}_i\bar{u}_i + \underbrace{\overline{\rho' u_i' u_j'}}_{\text{Reynolds stress tensor}}) = -\frac{\partial \bar{p}}{\partial x_i} + \frac{\partial}{\partial x_j}(2\mu S_{ji}) \tag{D.6}$$

A direct comparison between equations D.5 and D.6 shows many additional terms due to the consideration of compressibility. One term in particular: $\overline{\rho' u_i' u_j'}$ requires special attention. In turbulence modelling, a correlation must be sought for this term that relates density fluctuations to velocity fluctuations; a triple correlation. This is adds much complexity viewing the incompressible definition found before. Furthermore, in context of CFD, this term can slow down *convergence*, requiring more computational time and possibly numerical instabilities.

Convergence in CFD codes

Consider a simple example of a 3x3 system of equations in matrix format:

$$\begin{bmatrix} A_{11} & A_{12} & A_{13} \\ A_{21} & A_{22} & A_{23} \\ A_{31} & A_{32} & A_{33} \end{bmatrix} \begin{bmatrix} x \\ y \\ z \end{bmatrix} = \begin{bmatrix} b_x \\ b_y \\ b_z \end{bmatrix} \tag{D.7}$$

The objective is to find a solution for x, y and z. This is accomplished by minimizing the off-diagonal entries, leading to A_{11}, A_{22} and A_{33} as the dominant matrix elements. This progression is monitored in CFD codes via a comparison on the basis of off- and on-diagonal elements:

$$|A_{i,i}| \geq \sum_{j=1}^{N} |A_{i,j}| \text{ for all } i, \tag{D.8}$$

which basically checks if the diagonal value is greater than the off-diagonal entries. If this is the case, and the diagonal entry is much larger, the solution is said to be converged.
The Reynolds stress tensor from equation D.6 is a cross-coupling term. The density fluctuation ρ' couples into velocity fluctuations u_i', u_j' and vice versa. Although not an exact formulation in CFD codes, equation $D.7$ symbolizes for such cross-coupling terms that changes in off-diagonal elements result in changes of the others. These cross-coupling terms should therefore be modelled to find appropriate results for ρ', u_i' and u_j' individually.

Favre-Averaging

In Favre-averaging, the flow properties are mass-averaged:

$$\tilde{\phi} = \frac{\overline{\rho\phi}}{\rho} \tag{D.9}$$

and

$$\phi = \tilde{\phi} + \phi'' \tag{D.10}$$

where $\tilde{\phi}$ is the Favre-averaged quantity and ϕ'' is the Favre-fluctuating quantity. Note here that the double prime is just to indicate that this is a Favre-averaged property, not a Reynolds-averaged property.
The Favre-averaged properties are slightly different, whereas the Reynolds average $u_i'' \neq 0$, but $\overline{\rho u_i''} = 0$. Additionally, note in the following equations that density is Reynolds-averaged and the velocity components are Reynolds-averaged. The averaged Navier-Stokes equations now become:

$$\frac{\partial}{\partial t}\left((\overline{\rho + \rho'})(\overline{\tilde{u}_i + u_i''})\right) + \frac{\partial}{\partial x_j}\left((\overline{\rho + \rho'})(\overline{\tilde{u}_i + u_i''})(\overline{\tilde{u}_j + u_j''})\right) = -\frac{\partial \bar{p}}{\partial x_j} + \frac{\partial}{\partial x_j}\left(\overline{S_{ji}}\right) \tag{D.11}$$

Simplifying the left-hand side expressions with the properties of Favre-averaging and Reynolds-averaging, the equation reduces to:

$$\frac{\partial}{\partial t}\left(\bar{\rho}\tilde{u}_i\right) + \frac{\partial}{\partial x_j}\left(\bar{\rho}\overline{u_i'' u_j''} + \bar{\rho}\tilde{u}_i\tilde{u}_j\right) = -\frac{\partial \bar{p}}{\partial x_j} + \frac{\partial}{\partial x_j}\left(\overline{S_{ji}}\right) \tag{D.12}$$

Comparing equations D.12 to D.6 shows that the Reynolds stress term no longer contains density fluctuations, hence dropping the requirement to model triple fluctuating components. Furthermore, comparing D.12 to D.5 shows that the Reynolds stress term is very much the same. Hence, the modelling approach is drastically decreased in complexity, showing that Favre averaging is a favourable mathematical simplification when experiencing compressibility effects in CFD codes.

E Measurements

This appendix lists the measurements for the individual test subjects: ∅ 8, ∅ 5, and ∅ 3.2. The pressure, thermocouple, and mass flow rate sensor locations are indicated in Figure 45:

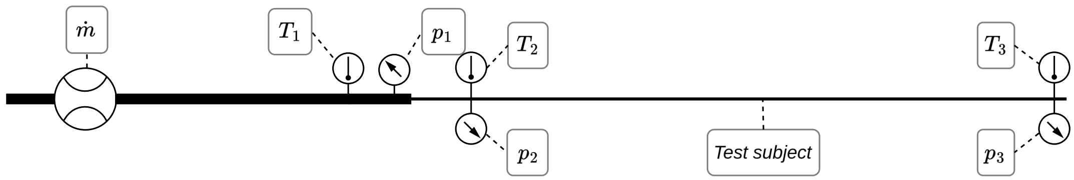

Figure 45: Test line including measurement locations

E.1 Pressure and temperature in ∅ 8 vs. mass Flow

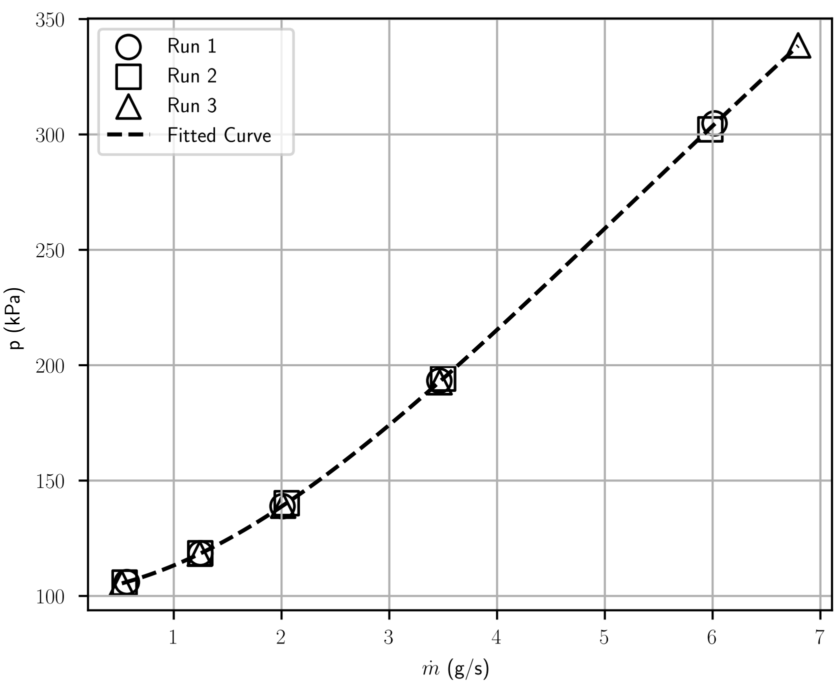

Figure 46: Measurements of T3 - 8 mm tube with fitted curve

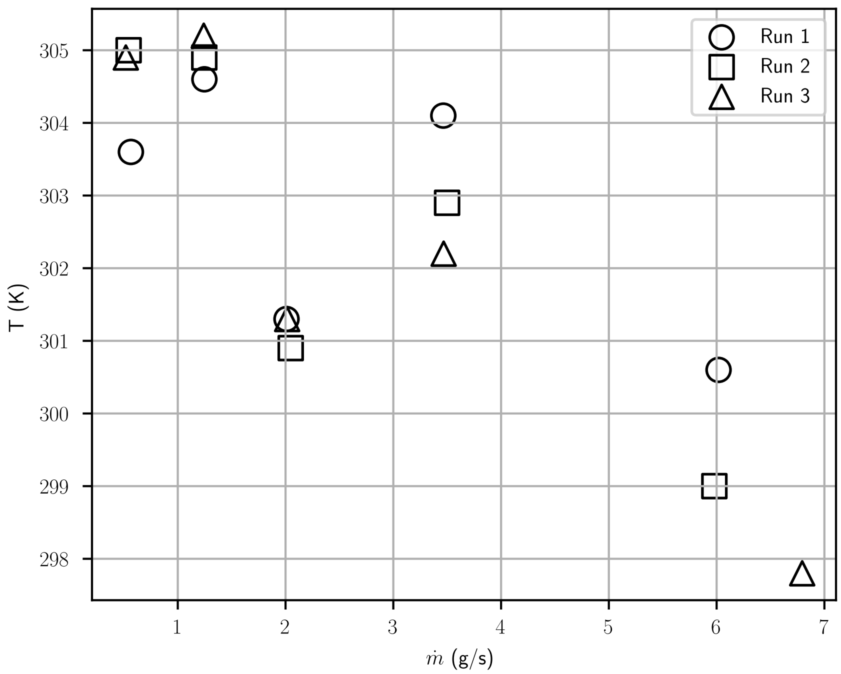

Figure 47: Caption

Pressure and temperature in ∅ 8 at a mass flow of 0.5 $\frac{g}{s}$

Run nr.	u_{inst}	u_{test}	$\dot{m}$
Run 1	0.0085 $\frac{g}{s}$	0.00024 $\frac{g}{s}$	(0.5650 ± 0.017) $\frac{g}{s}$
Run 2	0.0082 $\frac{g}{s}$	0.00024 $\frac{g}{s}$	(0.5439 ± 0.016) $\frac{g}{s}$
Run 3	0.0078 $\frac{g}{s}$	0.00024 $\frac{g}{s}$	(0.5179 ± 0.016) $\frac{g}{s}$

Table 27: Mass Flow Rate

Run nr.	u_{inst}	u_{test}	p_1
Run 1	1.4 kPa	0.0024 kPa	(106.0 ± 2.8) kPa
Run 2	1.4 kPa	0.0027 kPa	(105.8 ± 2.8) kPa
Run 3	1.4 kPa	0.0021 kPa	(105.5 ± 2.8) kPa

Table 28: Pressure p_1

Run nr.	u_{inst}	u_{test}	T_1
Run 1	0.70 K	0.0050 K	(303.6 ± 1.4) K
Run 2	0.70 K	0.0025 K	(305.0 ± 1.4) K
Run 3	0.70 K	0.0022 K	(304.9 ± 1.4) K

Table 29: Temperature T_1

Pressure and temperature in ∅ 8 at a mass flow of 1 $\frac{g}{s}$

Run nr.	u_{inst}	u_{test}	$\dot{m}$
Run 1	0.019 $\frac{g}{s}$	0.00039 $\frac{g}{s}$	(1.247 ± 0.038) $\frac{g}{s}$
Run 2	0.019 $\frac{g}{s}$	0.00052 $\frac{g}{s}$	(1.246 ± 0.038) $\frac{g}{s}$
Run 3	0.019 $\frac{g}{s}$	0.00046 $\frac{g}{s}$	(1.241 ± 0.038) $\frac{g}{s}$

Table 30: Mass Flow Rate

Run nr.	u_{inst}	u_{test}	p_1
Run 1	1.4 kPa	0.0032 kPa	(118.5 ± 2.8) kPa
Run 2	1.4 kPa	0.0030 kPa	(118.5 ± 2.8) kPa
Run 3	1.4 kPa	0.0033 kPa	(118.3 ± 2.8) kPa

Table 31: Pressure

Run nr.	u_{inst}	u_{test}	T_1
Run 1	0.70 K	0.0042 K	(304.6 ± 1.4) K
Run 2	0.70 K	0.0032 K	(304.9 ± 1.4) K
Run 3	0.70 K	0.0029 K	(305.2 ± 1.4) K

Table 32: Temperature

Pressure and temperature in ∅ 8 at a mass flow of 2 $\frac{g}{s}$

Run nr.	u_{inst}	u_{test}	$\dot{m}$
Run 1	0.012 $\frac{g}{s}$	0.00065 $\frac{g}{s}$	(2.009 ± 0.024) $\frac{g}{s}$
Run 2	0.012 $\frac{g}{s}$	0.00070 $\frac{g}{s}$	(2.048 ± 0.024) $\frac{g}{s}$
Run 3	0.012 $\frac{g}{s}$	0.00066 $\frac{g}{s}$	(2.015 ± 0.024) $\frac{g}{s}$

Table 33: Mass Flow Rate

Run nr.	u_{inst}	u_{test}	p_1
Run 1	1.4 kPa	0.005868 kPa	(138.9 ± 2.8) kPa
Run 2	1.4 kPa	0.005871 kPa	(140.2 ± 2.8) kPa
Run 3	1.4 kPa	0.008694 kPa	(139.1 ± 2.8) kPa

Table 34: Pressure

Run nr.	u_{inst}	u_{test}	T_1
Run 1	0.70 K	0.0022 K	(301.3 ± 1.4) K
Run 2	0.70 K	0.0081 K	(300.9 ± 1.4) K
Run 3	0.70 K	0.0020 K	(301.3 ± 1.4) K

Table 35: Temperature

Pressure and temperature in ∅ 8 at a mass flow of 3.5 $\frac{g}{s}$

Run nr.	u_{inst}	u_{test}	$\dot{m}$
Run 1	0.0069 $\frac{g}{s}$	0.0015 $\frac{g}{s}$	(3.464 ± 0.014) $\frac{g}{s}$
Run 2	0.0070 $\frac{g}{s}$	0.0015 $\frac{g}{s}$	(3.499 ± 0.014) $\frac{g}{s}$
Run 3	0.0070 $\frac{g}{s}$	0.0017 $\frac{g}{s}$	(3.467 ± 0.014) $\frac{g}{s}$

Table 36: Mass Flow Rate

Run nr.	u_{inst}	u_{test}	p_1
Run 1	1.4	0.014	(193.3 ± 2.8) kPa
Run 2	1.4	0.010	(194.2 ± 2.8) kPa
Run 3	1.4	0.018	(192.6 ± 2.8) kPa

Table 37: Pressure

Run nr.	u_{inst}	u_{test}	T_1
Run 1	0.70 K	0.0089 K	(304.1 ± 1.4) K
Run 2	0.70 K	0.0063 K	(302.9 ± 1.4) K
Run 3	0.70 K	0.0043 K	(302.2 ± 1.4) K

Table 38: Temperature

Pressure and temperature in ∅ 8 at a mass flow of 7 $\frac{g}{s}$

Run nr.	u_{inst}	u_{test}	$\dot{m}$
Run 1	0.012	0.0022	(6.018 ± 0.024) $\frac{g}{s}$
Run 2	0.012	0.0022	(5.979 ± 0.024) $\frac{g}{s}$
Run 3	0.014	0.0039	(6.794 ± 0.029) $\frac{g}{s}$

Table 39: Mass Flow Rate

Run nr.	u_{inst}	u_{test}	p_1
Run 1	1.4 kPa	0.035 kPa	(304.8 ± 2.8) kPa
Run 2	1.4 kPa	0.033 kPa	(302.2 ± 2.8) kPa
Run 3	1.4 kPa	0.18 kPa	(338.6 ± 2.8) kPa

Table 40: Pressure

Run nr.	u_{inst}	u_{test}	T_1
Run 1	0.70 K	0.0078 K	(300.6 ± 1.4) K
Run 2	0.70 K	0.0090 K	(299.0 ± 1.4) K
Run 3	0.69 K	0.010 K	(297.8 ± 1.4) K

Table 41: Temperature

E.2 Pressure and temperature in ∅ 5 vs. mass flow

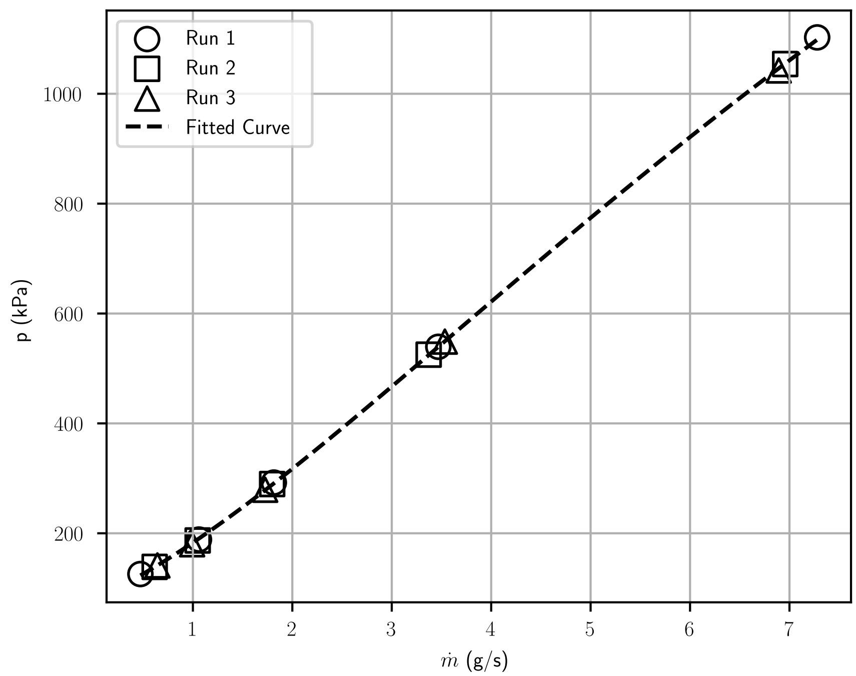

Figure 48: Pressure sensor (1)

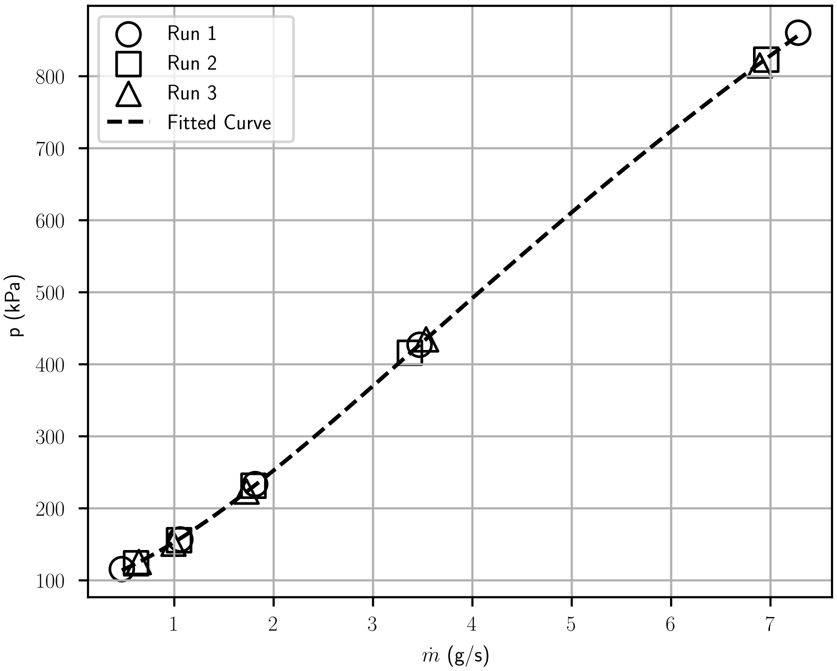

Figure 49: Pressure sensor (2)

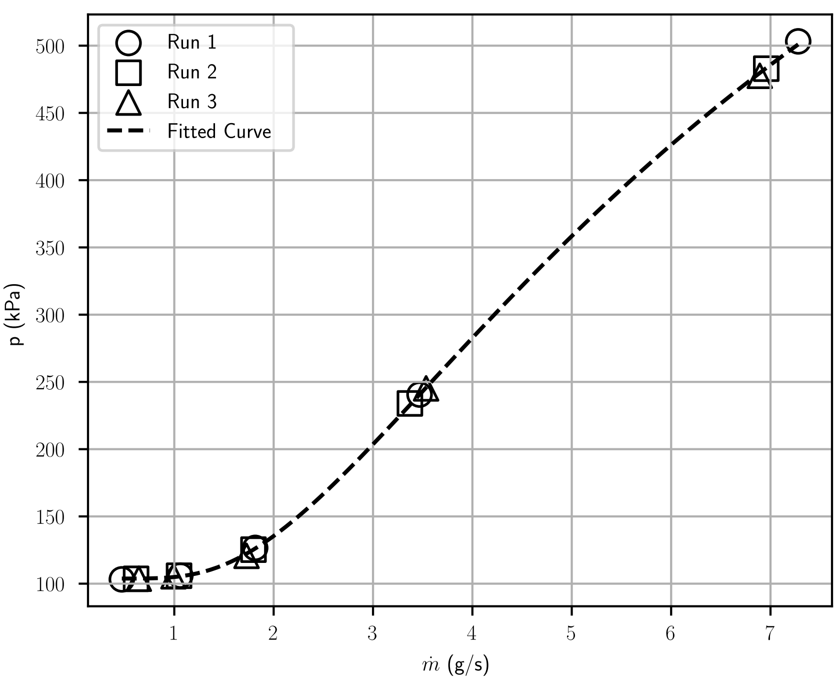

Figure 50: Pressure sensor (3)

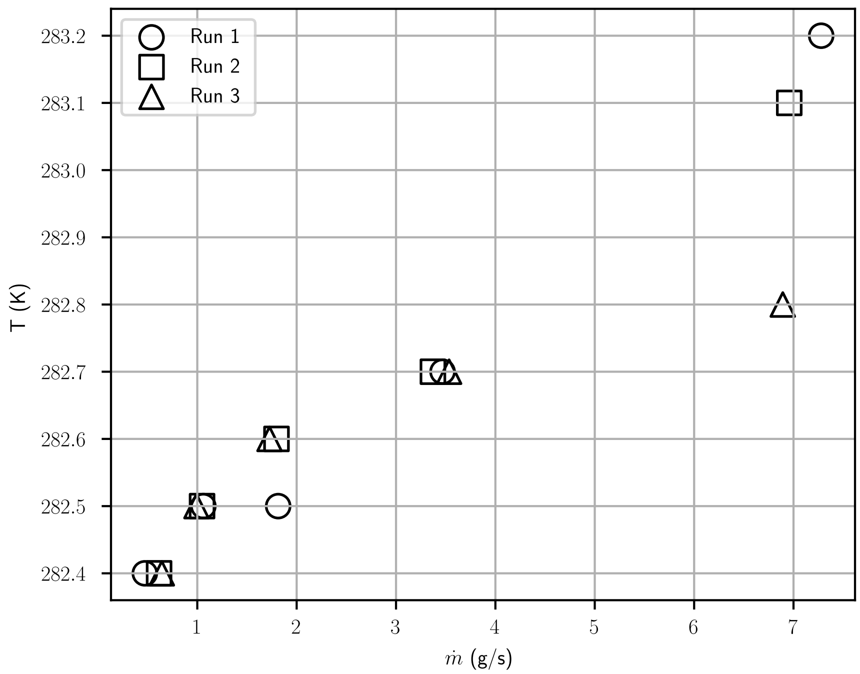

Figure 51: Thermocouple (1)

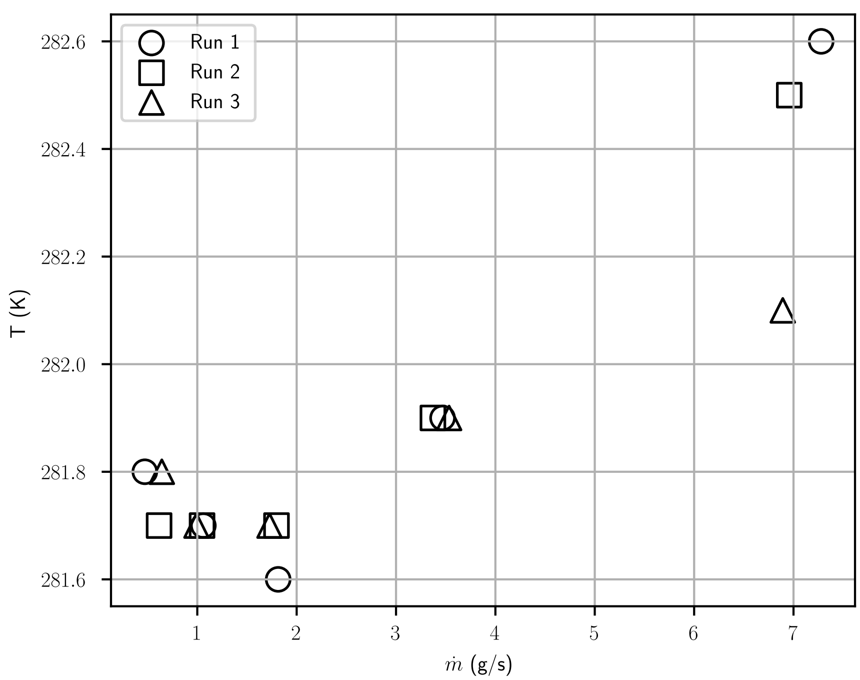

Figure 52: Thermocouple (2)

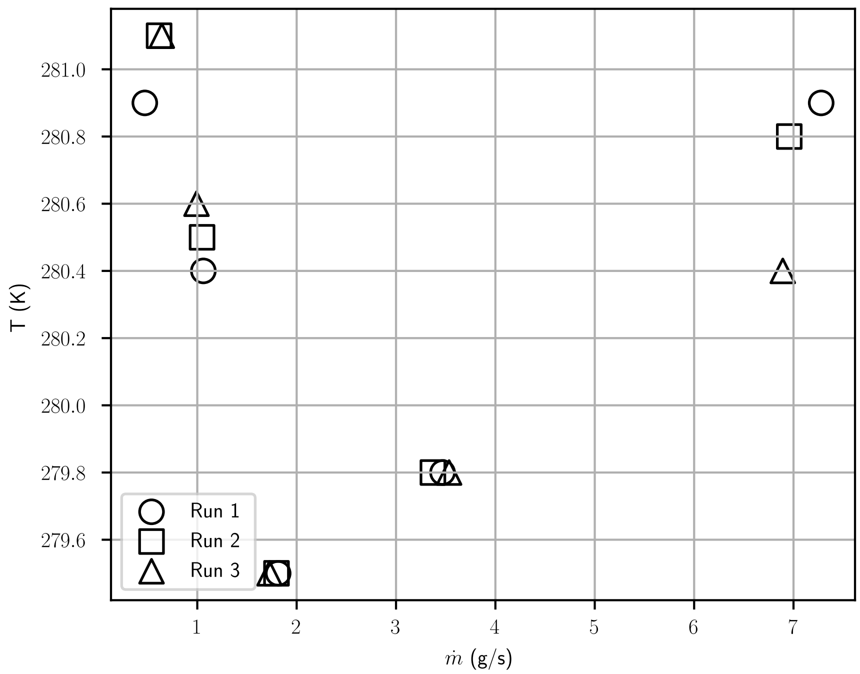

Figure 53: Thermocouple (3)

Pressure and temperature in ∅ 5 at a mass flow of 0.5 $\frac{g}{s}$

Run nr.	u_{inst}	u_{test}	p_1
Run 1	1.4 kPa	0.0048 kPa	(125.8 ± 2.8) kPa
Run 2	1.4 kPa	0.0064 kPa	(138.8 ± 2.8) kPa
Run 3	1.4 kPa	0.0081 kPa	(141.5 ± 2.8) kPa

Table 42: Pressure sensor (1)

Run nr.	u_{inst}	u_{test}	p_2
Run 1	1.4 kPa	0.0027 kPa	(115.6 ± 2.8) kPa
Run 2	1.4 kPa	0.0038 kPa	(123.7 ± 2.8) kPa
Run 3	1.4 kPa	0.0048 kPa	(125.4 ± 2.8) kPa

Table 43: Pressure sensor (2)

Run nr.	u_{inst}	u_{test}	p_3
Run 1	1.4 kPa	0.0018 kPa	(103.2 ± 2.8) kPa
Run 2	1.4 kPa	0.0028 kPa	(103.6 ± 2.8) kPa
Run 3	1.4 kPa	0.0029 kPa	(103.7 ± 2.8) kPa

Table 44: Pressure sensor (3)

Run nr.	u_{inst}	u_{test}	T_3
Run 1	0.65 K	0.0019 K	(282.4 ± 1.3) K
Run 2	0.65 K	0.0023 K	(282.4 ± 1.3) K
Run 3	0.65 K	0.0023 K	(282.4 ± 1.3) K

Table 45: Thermocouple (1)

Run nr.	u_{inst}	u_{test}	T_2
Run 1	0.65 K	0.0022 K	(281.8 ± 1.3) K
Run 2	0.65 K	0.0026 K	(281.7 ± 1.3) K
Run 3	0.65 K	0.0024 K	(281.8 ± 1.3) K

Table 46: Thermocouple (2)

Run nr.	u_{inst}	u_{test}	T_3
Run 1	0.65 K	0.0048 K	(280.9 ± 1.3) K
Run 2	0.65 K	0.0029 K	(281.1 ± 1.3) K
Run 3	0.65 K	0.0032 K	(281.1 ± 1.3) K

Table 47: Thermocouple (3)

Run nr.	u_{inst}	u_{test}	$\dot{m}$
Run 1	0.0071 $\frac{\text{g}}{\text{s}}$	0.00020 $\frac{\text{g}}{\text{s}}$	(0.4720 ± 0.014) $\frac{\text{g}}{\text{s}}$
Run 2	0.0092 $\frac{\text{g}}{\text{s}}$	0.00022 $\frac{\text{g}}{\text{s}}$	(0.6156 ± 0.018) $\frac{\text{g}}{\text{s}}$
Run 3	0.0096 $\frac{\text{g}}{\text{s}}$	0.00022 $\frac{\text{g}}{\text{s}}$	(0.6430 ± 0.019) $\frac{\text{g}}{\text{s}}$

Table 48: Mass flow-rate

Pressure and temperature in ∅ 5 at a mass flow of 1 $\frac{\text{g}}{\text{s}}$

Run nr.	u_{inst}	u_{test}	p_1
Run 1	1.4	0.016	(188.6 ± 2.8) kPa
Run 2	1.4	0.018	(186.9 ± 2.8) kPa
Run 3	1.4	0.012	(180.0 ± 2.8) kPa

Table 49: Pressure sensor (1)

Run nr.	u_{inst}	u_{test}	p_2
Run 1	1.4 kPa	0.011 kPa	(156.8 ± 2.8) kPa
Run 2	1.4 kPa	0.013 kPa	(155.7 ± 2.8) kPa
Run 3	1.4 kPa	0.0073 kPa	(150.9 ± 2.8) kPa

Table 50: Pressure sensor (2)

Run nr.	u_{inst}	u_{test}	p_3
Run 1	1.4 kPa	0.0028 kPa	(106.0 ± 2.8) kPa
Run 2	1.4 kPa	0.0029 kPa	(105.9 ± 2.8) kPa
Run 3	1.4 kPa	0.0026 kPa	(105.5 ± 2.8) kPa

Table 51: Pressure sensor (3)

Run nr.	u_{inst}	u_{test}	T_1
Run 1	0.65	0.0023	(282.5 ± 1.3) K
Run 2	0.65	0.0024	(282.5 ± 1.3) K
Run 3	0.65	0.0021	(282.5 ± 1.3) K

Table 52: Thermocouple (1)

Run nr.	u_{inst}	u_{test}	T_2
Run 1	0.65	0.0024	(281.7 ± 1.3) K
Run 2	0.65	0.0046	(281.7 ± 1.3) K
Run 3	0.65	0.0026	(281.7 ± 1.3) K

Table 53: Thermocouple (2)

Run nr.	u_{inst}	u_{test}	T_3
Run 1	0.65	0.0029	(280.4 ± 1.3) K
Run 2	0.65	0.0025	(280.5 ± 1.3) K
Run 3	0.65	0.0039	(280.6 ± 1.3) K

Table 54: Thermocouple (3)

Run nr.	u_{inst}	u_{test}	$\dot{m}$
Run 1	0.016	0.00034	$(1.061 \pm 0.032)\ \frac{g}{s}$
Run 2	0.016	0.00039	$(1.048 \pm 0.032)\ \frac{g}{s}$
Run 3	0.015	0.00030	$(0.992 \pm 0.030\ )\ \frac{g}{s}$

Table 55: Mass flow-rate

Pressure and temperature in ∅ 5 at a mass flow of 1.75 $\frac{g}{s}$

Run nr.	u_{inst}	u_{test}	p_1
Run 1	1.4	0.038	(292.3 ± 2.8) kPa
Run 2	1.4	0.033	(289.6 ± 2.8) kPa
Run 3	1.4	0.026	(279.2 ± 2.8) kPa

Table 56: Pressure sensor (1)

Run nr.	u_{inst}	u_{test}	p_2
Run 1	1.4	0.029	(233.6 ± 2.8) kPa
Run 2	1.4	0.027	(231.4 ± 2.8) kPa
Run 3	1.4	0.021	(223.3 ± 2.8) kPa

Table 57: Pressure sensor (2)

Run nr.	u_{inst}	u_{test}	p_3
Run 1	1.4	0.017	(126.6 ± 2.8) kPa
Run 2	1.4	0.015	(125.3 ± 2.8) kPa
Run 3	1.4	0.011	(120.7 ± 2.8) kPa

Table 58: Pressure sensor (3)

Run nr.	u_{inst}	u_{test}	T_1
Run 1	0.65	0.0028	(282.5 ± 1.3) K
Run 2	0.65	0.0022	(282.6 ± 1.3) K
Run 3	0.65	0.0023	(282.6 ± 1.3) K

Table 59: Thermocouple (1)

Run nr.	u_{inst}	u_{test}	T_2
Run 1	0.65	0.0028	(281.6 ± 1.3) K
Run 2	0.65	0.0025	(281.7 ± 1.3) K
Run 3	0.65	0.0022	(281.7 ± 1.3) K

Table 60: Thermocouple (2)

Run nr.	u_{inst}	u_{test}	T_3
Run 1	0.65	0.0046	$279.5 \pm 1.3)$ K
Run 2	0.65	0.0071	$279.5 \pm 1.3)$ K
Run 3	0.65	0.0022	$279.5 \pm 1.3)$ K

Table 61: Thermocouple (3)

Run nr.	u_{inst}	u_{test}	$\dot{m}$
Run 1	0.011	0.00058	$(1.814 \pm 0.022)\ \frac{g}{s}$
Run 2	0.011	0.00056	$(1.797 \pm 0.022)\ \frac{g}{s}$
Run 3	0.010	0.00055	$(1.727 \pm 0.020)\ \frac{g}{s}$

Table 62: Mass flow-rate

3.5 $\frac{g}{s}$

Run nr.	u_{inst}	u_{test}	p_1
Run 1	1.4 kPa	0.035 kPa	(539.4 ± 2.8) kPa
Run 2	1.4 kPa	0.053 kPa	(525.1 ± 2.8) kPa
Run 3	1.4 kPa	0.055 kPa	(548.9 ± 2.8) kPa

Table 63: Pressure sensor (1)

Run nr.	u_{inst}	u_{test}	p_2
Run 1	1.4 kPa	0.029 kPa	(427.1 ± 2.8) kPa
Run 2	1.4 kPa	0.040 kPa	(416.0 ± 2.8) kPa
Run 3	1.4 kPa	0.043 kPa	(434.6 ± 2.8) kPa

Table 64: Pressure sensor (2)

Run nr.	u_{inst}	u_{test}	p_3
Run 1	1.4 kPa	0.017 kPa	240.6 ± 2.8) kPa
Run 2	1.4 kPa	0.024 kPa	234.0 ± 2.8) kPa
Run 3	1.4 kPa	0.025 kPa	245.2 ± 2.8) kPa

Table 65: Pressure sensor (3)

Run nr.	u_{inst}	u_{test}	T_1
Run 1	0.65 K	0.0029 K	282.7 ± 1.3) K
Run 2	0.65 K	0.0018 K	282.7 ± 1.3) K
Run 3	0.65 K	0.0021 K	282.7 ± 1.3) K

Table 66: Thermocouple (1)

Run nr.	u_{inst}	u_{test}	T_2
Run 1	0.65 K	0.0037 K	(281.9 ± 1.3) K
Run 2	0.65 K	0.0024 K	(281.9 ± 1.3) K
Run 3	0.65 K	0.0024 K	(281.9 ± 1.3) K

Table 67: Thermocouple (2)

Run nr.	u_{inst}	u_{test}	T_3
Run 1	0.65 K	0.0027 K	(279.8 ± 1.3) K
Run 2	0.65 K	0.0023 K	(279.8 ± 1.3) K
Run 3	0.65 K	0.0025 K	(279.8 ± 1.3) K

Table 68: Thermocouple (3)

Run nr.	u_{inst}	u_{test}	$\dot{m}$
Run 1	0.0069 $\frac{g}{s}$	0.0011 $\frac{g}{s}$	(3.4682 ± 0.0138) $\frac{g}{s}$
Run 2	0.0067 $\frac{g}{s}$	0.0010 $\frac{g}{s}$	(3.3711 ± 0.0134) $\frac{g}{s}$
Run 3	0.0071 $\frac{g}{s}$	0.0011 $\frac{g}{s}$	(3.5340 ± 0.0142) $\frac{g}{s}$

Table 69: Mass flow-rate

7 $\frac{g}{s}$

The first run was taken over a period of 20 seconds as pressure sensors were lagging behind each other.

Run nr.	u_{inst}	u_{test}	p_1
Run 1	1.4 kPa	0.17 kPa	(1102.6 ± 2.8) kPa
Run 2	1.4 kPa	0.26 kPa	(1054.1 ± 2.8) kPa
Run 3	1.4 kPa	0.28 kPa	(1042.4 ± 2.8) kPa

Table 70: Pressure sensor (1)

Run nr.	u_{inst}	u_{test}	p_2
Run 1	1.4 kPa	0.12 kPa	(860.4 ± 2.8) kPa
Run 2	1.4 kPa	0.20 kPa	(823.0 ± 2.8) kPa
Run 3	1.4 kPa	0.21 kPa	(814.9 ± 2.8) kPa

Table 71: Pressure sensor (2)

Run nr.	u_{inst}	u_{test}	p_3
Run 1	1.4	0.076	(503.2 ± 2.8) kPa
Run 2	1.4	0.13	(482.9 ± 2.8) kPa
Run 3	1.4	0.13	(477.6 ± 2.8) kPa

Table 72: Pressure sensor (3)

Run nr.	u_{inst}	u_{test}	T_1
Run 1	0.65 K	0.0085 K	(283.2 ± 1.3) K
Run 2	0.65 K	0.0033 K	(283.1 ± 1.3) K
Run 3	0.65 K	0.0045 K	(282.8 ± 1.3) K

Table 73: Thermocouple (1)

Run nr.	u_{inst}	u_{test}	T_2
Run 1	0.65 K	0.0057 K	(282.6 ± 1.3) K
Run 2	0.65 K	0.0036 K	(282.5 ± 1.3) K
Run 3	0.65 K	0.0072 K	(282.1 ± 1.3) K

Table 74: Thermocouple (2)

Run nr.	u_{inst}	u_{test}	T_3
Run 1	0.65 K	0.0077 K	(280.9 ± 1.3)K
Run 2	0.65 K	0.0036 K	(280.8 ± 1.3)K
Run 3	0.65 K	0.0044 K	(280.4 ± 1.3)K

Table 75: Thermocouple (3)

Run nr.	u_{inst}	u_{test}	$\dot{m}$
Run 1	0.015 $\frac{\text{g}}{\text{s}}$	0.0036 $\frac{\text{g}}{\text{s}}$	(7.278675 ± 0.031) $\frac{\text{g}}{\text{s}}$
Run 2	0.014 $\frac{\text{g}}{\text{s}}$	0.0025 $\frac{\text{g}}{\text{s}}$	(6.957225 ± 0.028) $\frac{\text{g}}{\text{s}}$
Run 3	0.014 $\frac{\text{g}}{\text{s}}$	0.0026 $\frac{\text{g}}{\text{s}}$	(6.892106 ± 0.028) $\frac{\text{g}}{\text{s}}$

Table 76: Mass flow-rate

E.3 Pressure and temperature in ∅ 3.2 vs. mass flow

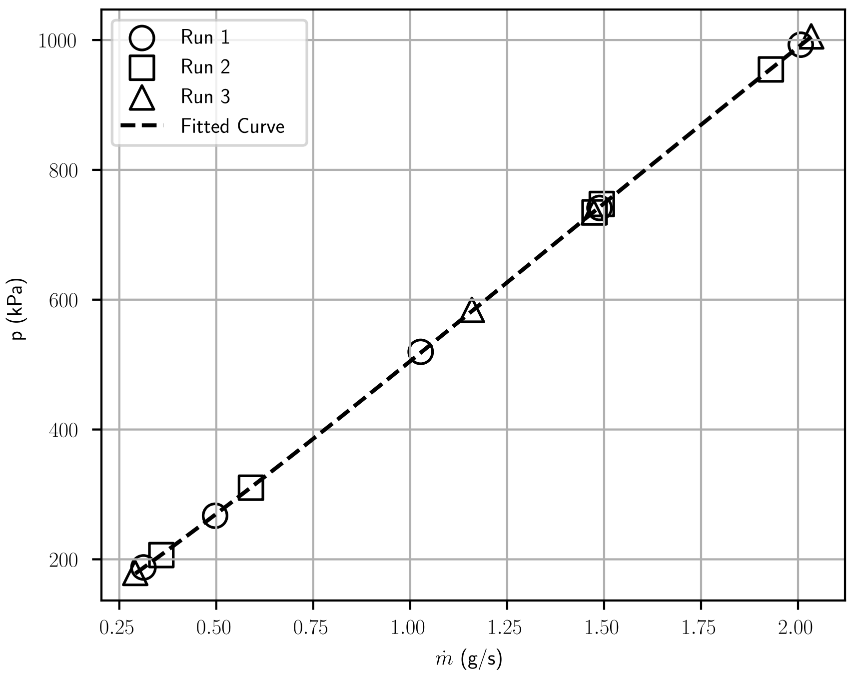

Figure 54: Pressure sensor (1)

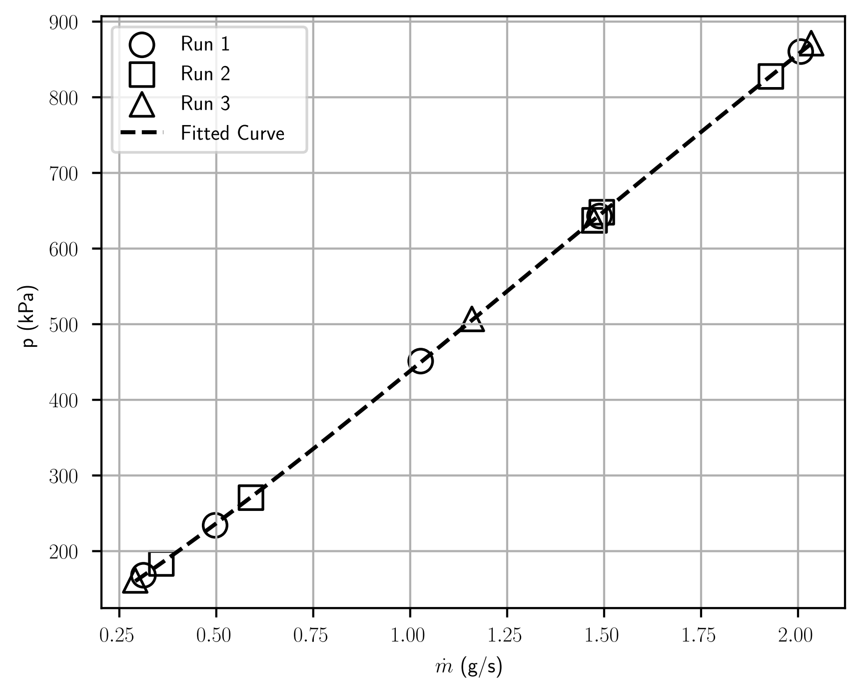

Figure 55: Pressure sensor (2)

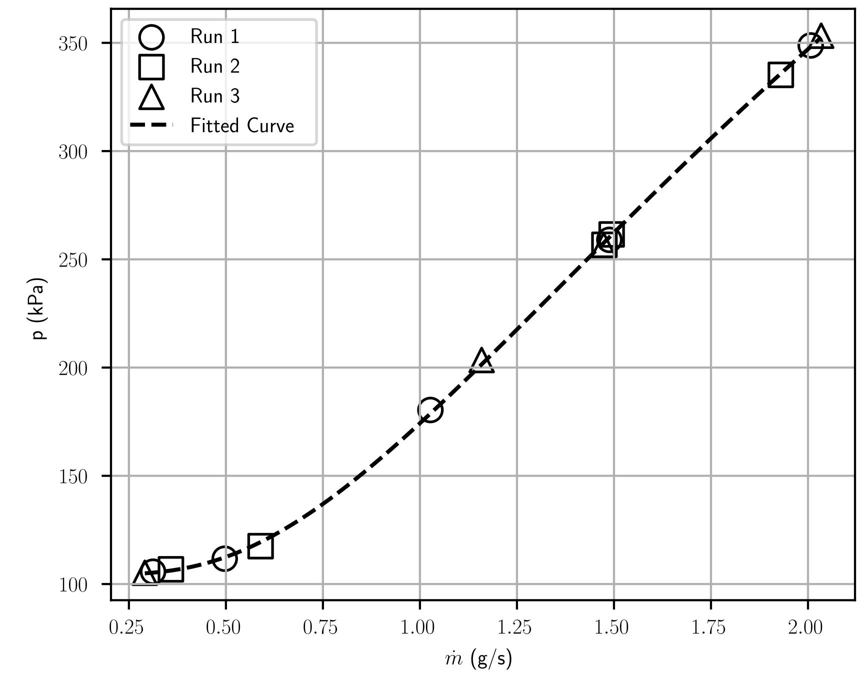

Figure 56: Pressure sensor (3)

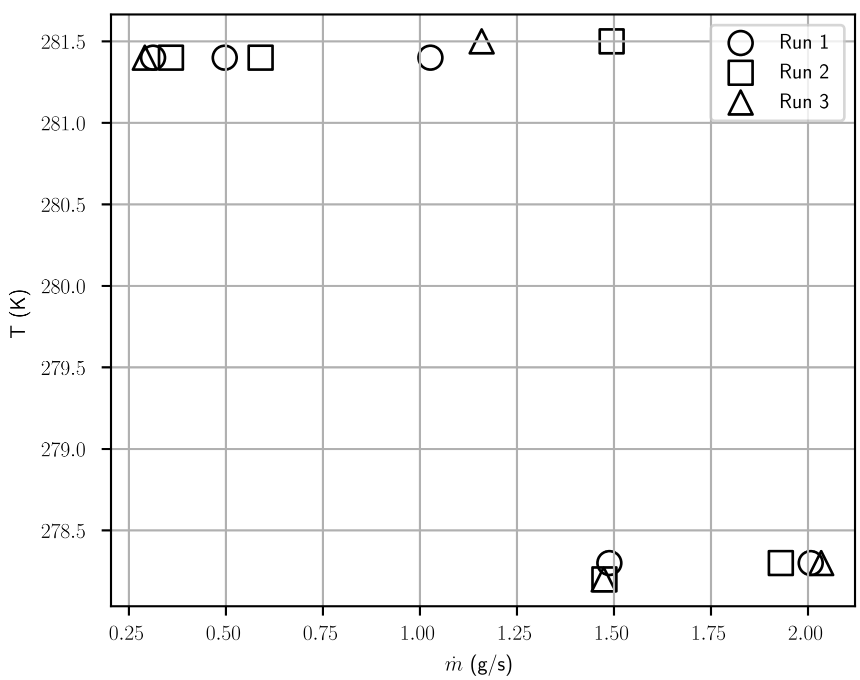

Figure 57: Thermocouple (1)

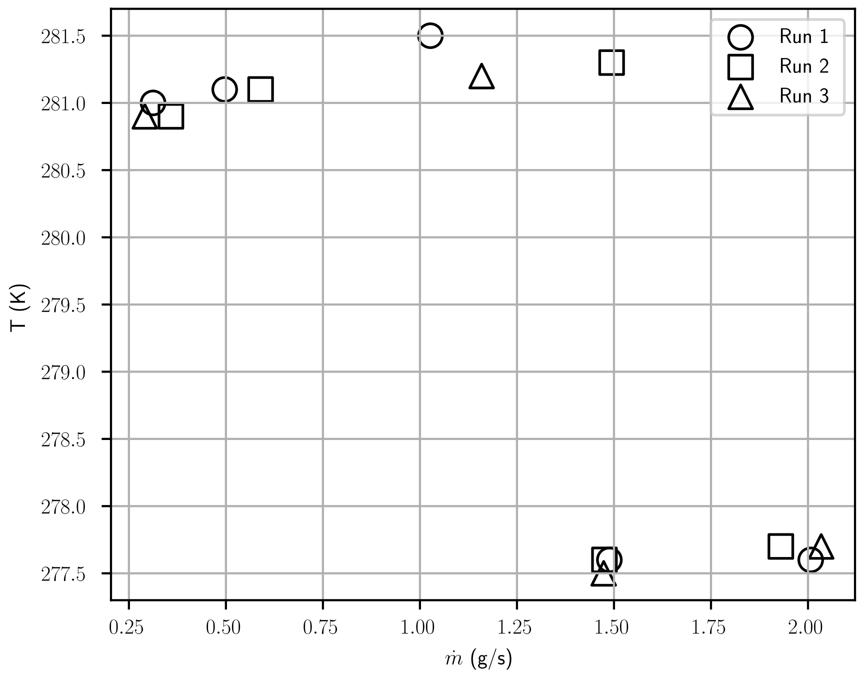

Figure 58: Thermocouple (2)

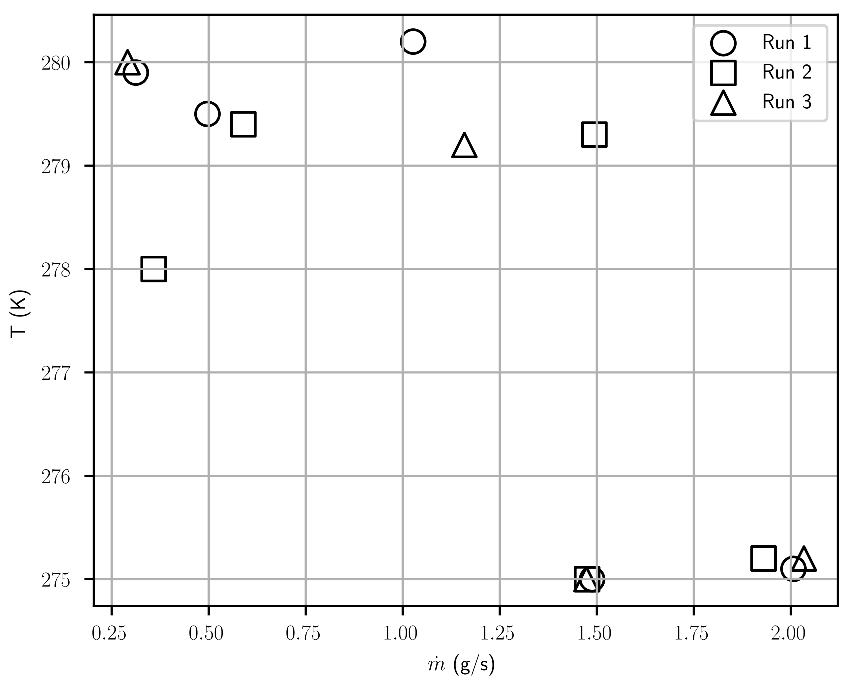

Figure 59: Thermocouple (3)

Pressure and temperature in ∅ 3.2 at a mass flow of 0.25 $\frac{g}{s}$

Run nr.	u_{inst}	u_{test}	p_1
Run 1	1.4 kPa	0.0051 kPa	(187.5 ± 2.8) kPa
Run 2	1.4 kPa	0.013 kPa	(206.5 ± 2.8) kPa
Run 3	1.4 kPa	0.091 kPa	(179.0 ± 2.8) kPa

Table 77: Pressure sensor (1)

Run nr.	u_{inst}	u_{test}	p_2
Run 1	1.4 kPa	0.002846 kPa	(168.1 ± 2.8) kPa
Run 2	1.4 kPa	0.008119 kPa	(183.7 ± 2.8) kPa
Run 3	1.4 kPa	0.005009 kPa	(161.3 ± 2.8) kPa

Table 78: Pressure sensor (2)

Run nr.	u_{inst}	u_{test}	p_3
Run 1	1.4 kPa	0.0028 kPa	(105.7 ± 2.8) kPa
Run 2	1.4 kPa	0.0035 kPa	(106.8 ± 2.8) kPa
Run 3	1.4 kPa	0.0018 kPa	(105.2 ± 2.8) kPa

Table 79: Pressure sensor (3)

Run nr.	u_{inst}	u_{test}	T_1
Run 1	0.65 K	0.0022 K	(281.4 ± 1.3) K
Run 2	0.65 K	0.0021 K	(281.4 ± 1.3) K
Run 3	0.65 K	0.0021 K	(281.4 ± 1.3) K

Table 80: Thermocouple (1)

Run nr.	u_{inst}	u_{test}	T_2
Run 1	0.65 K	0.0024 K	(281.0 ± 1.3) K
Run 2	0.65 K	0.0027 K	(280.9 ± 1.3) K
Run 3	0.65 K	0.0027 K	(280.9 ± 1.3) K

Table 81: Thermocouple (2)

Run nr.	u_{inst}	u_{test}	T_3
Run 1	0.65 K	0.0024 K	(279.9 ± 1.3) K
Run 2	0.65 K	0.0026 K	(278.0 ± 1.3) K
Run 3	0.65 K	0.0021 K	(280.0 ± 1.3) K

Table 82: Thermocouple (3)

Run nr.	u_{inst}	u_{test}	$\dot{m}$
Run 1	0.0047 $\frac{g}{s}$	0.00016 $\frac{g}{s}$	(0.3122 ± 0.0094) $\frac{g}{s}$
Run 2	0.0054 $\frac{g}{s}$	0.00022 $\frac{g}{s}$	(0.3583 ± 0.0108) $\frac{g}{s}$
Run 3	0.0044 $\frac{g}{s}$	0.00018 $\frac{g}{s}$	(0.2910 ± 0.0088) $\frac{g}{s}$

Table 83: Mass flow-rate

Pressure and temperature in ∅ 3.2 at a mass flow of 0.5 $\frac{g}{s}$

Run nr.	u_{inst}	u_{test}	p_1
Run 1	1.4 kPa	0.024 kPa	(267.1 ± 2.8) kPa
Run 2	1.4 kPa	0.031 kPa	(310.3 ± 2.8) kPa

Table 84: Pressure sensor (1)

Run nr.	u_{inst}	u_{test}	p_2
Run 1	1.4 kPa	0.019 kPa	(234.1 ± 2.8) kPa
Run 2	1.4 kPa	0.026 kPa	(270.7 ± 2.8) kPa

Table 85: Pressure sensor (2)

Run nr.	u_{inst}	u_{test}	p_3
Run 1	1.4 kPa	0.0021 kPa	(111.7 ± 2.8) kPa
Run 2	1.4 kPa	0.0056 kPa	(117.5 ± 2.8) kPa

Table 86: Pressure sensor (3)

Run nr.	u_{inst}	u_{test}	T_1
Run 1	0.65 K	0.0019 K	(281.4 ± 1.3) K
Run 2	0.65 K	0.0018 K	(281.4 ± 1.3) K

Table 87: Thermocouple (1)

Run nr.	u_{inst}	u_{test}	T_2
Run 1	0.65 K	0.0033 K	(281.1 ± 1.3) K
Run 2	0.65 K	0.0030 K	(281.1 ± 1.3) K

Table 88: Thermocouple (2)

Run nr.	u_{inst}	u_{test}	T_3
Run 1	0.65 K	0.0030 K	(279.5 ± 1.3) K
Run 2	0.65 K	0.0064 K	(279.4 ± 1.3) K

Table 89: Thermocouple (3)

Run nr.	u_{inst}	u_{test}	$\dot{m}$
Run 1	0.0075 $\frac{\text{g}}{\text{s}}$	0.000227 $\frac{\text{g}}{\text{s}}$	(0.4969 ± 0.0150) $\frac{\text{g}}{\text{s}}$
Run 2	0.0088 $\frac{\text{g}}{\text{s}}$	0.000195 $\frac{\text{g}}{\text{s}}$	(0.5894 ± 0.0166) $\frac{\text{g}}{\text{s}}$

Table 90: Mass flow-rate

Pressure and temperature in ∅ 3.2 at a mass flow of 1 $\frac{\text{g}}{\text{s}}$

Run nr.	u_{inst}	u_{test}	p_1
Run 1	1.4 kPa	0.040 kPa	(519.6 ± 2.8) kPa
Run 2	1.4 kPa	0.073 kPa	(747.4 ± 2.8) kPa
Run 3	1.4 kPa	0.085 kPa	(584.3 ± 2.8) kPa

Table 91: Pressure sensor (1)

Run nr.	u_{inst}	u_{test}	p_2
Run 1	1.4 kPa	0.038 kPa	(451.2 ± 2.8) kPa
Run 2	1.4 kPa	0.061 kPa	(648.0 ± 2.8) kPa
Run 3	1.4 kPa	0.075 kPa	(507.0 ± 2.8) kPa

Table 92: Pressure sensor (2)

Run nr.	u_{inst}	u_{test}	p_3
Run 1	1.4 kPa	0.017 kPa	(180.4 ± 2.8) kPa
Run 2	1.4 kPa	0.026 kPa	(261.5 ± 2.8) kPa
Run 3	1.4 kPa	0.031 kPa	(203.5 ± 2.8) kPa

Table 93: Pressure sensor (3)

Run nr.	u_{inst}	u_{test}	T_1
Run 1	0.65 K	0.0026 K	(281.4 ± 1.3) K
Run 2	0.65 K	0.0022 K	(281.5 ± 1.3) K
Run 3	0.65 K	0.0019 K	(281.5 ± 1.3) K

Table 94: Thermocouple (1)

Run nr.	u_{inst}	u_{test}	T_2
Run 1	0.65 K	0.0038 K	(281.5 ± 1.3) K
Run 2	0.65 K	0.0024 K	(281.3 ± 1.3) K
Run 3	0.65 K	0.0035 K	(281.2 ± 1.3) K

Table 95: Thermocouple (2)

Run nr.	u_{inst}	u_{test}	T_3
Run 1	0.65 K	0.020 K	(280.2 ± 1.3) K
Run 2	0.65 K	0.0037 K	(279.3 ± 1.3) K
Run 3	0.65 K	0.0078 K	(279.2 ± 1.3) K

Table 96: Thermocouple (3)

Run nr.	u_{inst}	u_{test}	$\dot{m}$
Run 1	0.015 $\frac{g}{s}$	0.00030 $\frac{g}{s}$	(1.027 ± 0.030) $\frac{g}{s}$
Run 2	0.022 $\frac{g}{s}$	0.00043 $\frac{g}{s}$	(1.494 ± 0.044) $\frac{g}{s}$
Run 3	0.017 $\frac{g}{s}$	0.00035 $\frac{g}{s}$	(1.159 ± 0.034) $\frac{g}{s}$

Table 97: Mass flow-rate

Pressure and temperature in ∅ 3.2 at a mass flow of 1.5 $\frac{g}{s}$

Run nr.	u_{inst}	u_{test}	p_1
Run 1	1.4 kPa	0.074805 kPa	(741.3 ± 2.8) kPa
Run 2	1.4 kPa	0.03286 kPa	(734.6 ± 2.8) kPa
Run 3	1.4 kPa	0.101996 kPa	(734.4 ± 2.8) kPa

Table 98: Pressure sensor (1)

Run nr.	u_{inst}	u_{test}	p_2
Run 1	1.4 kPa	0.064 kPa	(643.0 ± 2.8) kPa
Run 2	1.4 kPa	0.028 kPa	(637.3 ± 2.8) kPa
Run 3	1.4 kPa	0.12 kPa	(637.2 ± 2.8) kPa

Table 99: Pressure sensor (2)

Run nr.	u_{inst}	u_{test}	p_3
Run 1	1.4 kPa	0.027 kPa	(259.0 ± 2.8) kPa
Run 2	1.4 kPa	0.013 kPa	(256.7 ± 2.8) kPa
Run 3	1.4 kPa	0.049 kPa	(256.6 ± 2.8) kPa

Table 100: Pressure sensor (3)

Run nr.	u_{inst}	u_{test}	T_1
Run 1	0.64 kPa	0.002217 kPa	(278.3 ± 1.3) kPa
Run 2	0.64 kPa	0.002099 kPa	(278.2 ± 1.3) kPa
Run 3	0.64 kPa	0.002031 kPa	(278.2 ± 1.3) kPa

Table 101: Thermocouple (1)

Run nr.	u_{inst}	u_{test}	T_2
Run 1	0.64 K	0.0024 K	(277.6 ± 1.3) K
Run 2	0.64 K	0.0020 K	(277.6 ± 1.3) K
Run 3	0.64 K	0.0024 K	(277.5 ± 1.3) K

Table 102: Thermocouple (2)

Run nr.	u_{inst}	u_{test}	T_3
Run 1	0.64 K	0.0021 K	(275.0 ± 1.3) K
Run 2	0.64 K	0.0020 K	(275.0 ± 1.3) K
Run 3	0.64 K	0.0024 K	(275.0 ± 1.3) K

Table 103: Thermocouple (3)

Run nr.	u_{inst}	u_{test}	$\dot{m}$
Run 1	0.022 $\frac{g}{s}$	0.00054 $\frac{g}{s}$	(1.4881 ± 0.044) $\frac{g}{s}$
Run 2	0.022 $\frac{g}{s}$	0.00043 $\frac{g}{s}$	(1.4754 ± 0.044) $\frac{g}{s}$
Run 3	0.022 $\frac{g}{s}$	0.00046 $\frac{g}{s}$	(1.4735 ± 0.044) $\frac{g}{s}$

Table 104: Mass flow-rate

Pressure and temperature in ∅ 3.2 at a mass flow of 2 $\frac{g}{s}$

Run nr.	u_{inst}	u_{test}	p_1
Run 1	1.4 kPa	0.073 kPa	992.8 ± 2.8 kPa
Run 2	1.4 kPa	0.061 kPa	954.7 ± 2.8 kPa
Run 3	1.4 kPa	0.091 kPa	1005.6 ± 2.8 kPa

Table 105: Pressure sensor (1)

Run nr.	u_{inst}	u_{test}	p_2
Run 1	1.4 kPa	0.061 kPa	(860.4 ± 2.8) kPa
Run 2	1.4 kPa	0.052 kPa	(827.5 ± 2.8) kPa
Run 3	1.4 kPa	0.077 kPa	(871.5 ± 2.8) kPa

Table 106: Pressure sensor (2)

Run nr.	u_{inst}	u_{test}	p_3
Run 1	1.4 kPa	0.027 kPa	348.8 ± 2.8 kPa
Run 2	1.4 kPa	0.022 kPa	335.2 ± 2.8 kPa
Run 3	1.4 kPa	0.033 kPa	353.3 ± 2.8 kPa

Table 107: Pressure sensor (3)

Run nr.	u_{inst}	u_{test}	T_1
Run 1	0.64 K	0.0027 K	(278.3 ± 1.3) K
Run 2	0.64 K	0.0023 K	(278.3 ± 1.3) K
Run 3	0.64 K	0.0020 K	(278.3 ± 1.3) K

Table 108: Thermocouple (1)

Run nr.	u_{inst}	u_{test}	T_2
Run 1	0.64 K	0.0036 K	277.6 ± 1.3 K
Run 2	0.64 K	0.0027 K	277.7 ± 1.3 K
Run 3	0.64 K	0.0024 K	277.7 ± 1.3 K

Table 109: Thermocouple (2)

Run nr.	u_{inst}	u_{test}	T_3
Run 1	0.64 K	0.0034 K	(275.1 ± 1.3) K
Run 2	0.64 K	0.0022 K	(275.2 ± 1.3) K
Run 3	0.64 K	0.0022 K	(275.2 ± 1.3) K

Table 110: Thermocouple (3)

Run nr.	u_{inst}	u_{test}	$\dot{m}$
Run 1	0.012 $\frac{g}{s}$	0.00063 $\frac{g}{s}$	(2.007 ± 0.024) $\frac{g}{s}$
Run 2	0.012 $\frac{g}{s}$	0.00051 $\frac{g}{s}$	(1.930 ± 0.024) $\frac{g}{s}$
Run 3	0.012 $\frac{g}{s}$	0.00068 $\frac{g}{s}$	(2.034 ± 0.024) $\frac{g}{s}$

Table 111: Mass flow-rate

F Roughness measurements

T1

Mitutoyo Surftest SJ-400

DATE 28-03-2008
TIME 02:17:39

R-PROFILE
EVA-L 1.25mm
λc 0.25mmX5

Ra 1.396µm
Rz 6.08µm
Rq 1.665µm
Rt 8.49µm

R-PROFILE
EVA-L 1.25mm
λc=0.25mmX5

×2K
×100

Ver. 5.0µm/cm
Hor. 100.0µm/cm

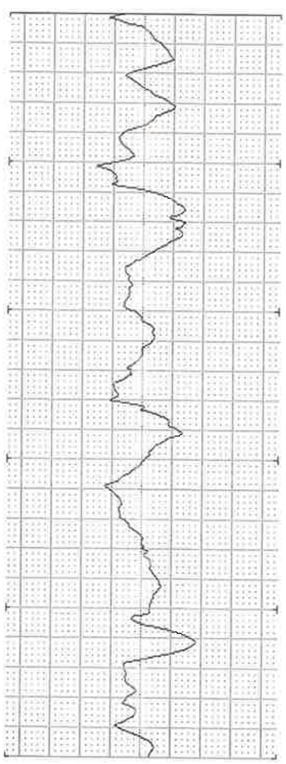

T1

Mitutoyo Surftest SJ-400

DATE 28-03-2008
TIME 02:16:20

R-PROFILE
EVA-L 1.25mm
λc 0.25mmX5

Ra 1.182µm
Rz 5.73µm
Rq 1.505µm
Rt 9.93µm

R-PROFILE
EVA-L 1.25mm
λc=0.25mmX5

×2K
×100

Ver. 5.0µm/cm
Hor. 100.0µm/cm

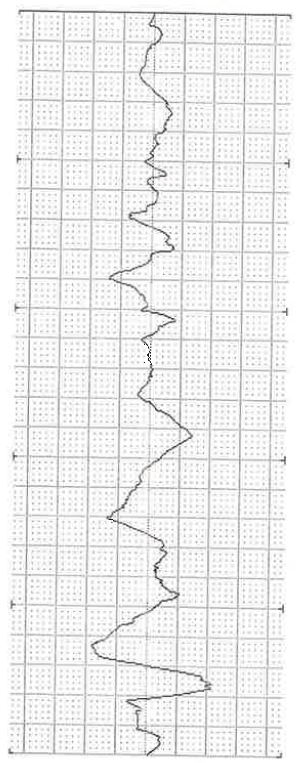

T1

Mitutoyo Surftest SJ-400

DATE 28-03-2008
TIME 02:19:01

R-PROFILE
EVA-L 1.25mm
λc 0.25mmX5

Ra 1.402µm
Rz 5.58µm
Rq 1.642µm
Rt 7.03µm

R-PROFILE
EVA-L 1.25mm
λc=0.25mmX5

×5K
×100

Ver. 2.0µm/cm
Hor. 100.0µm/cm

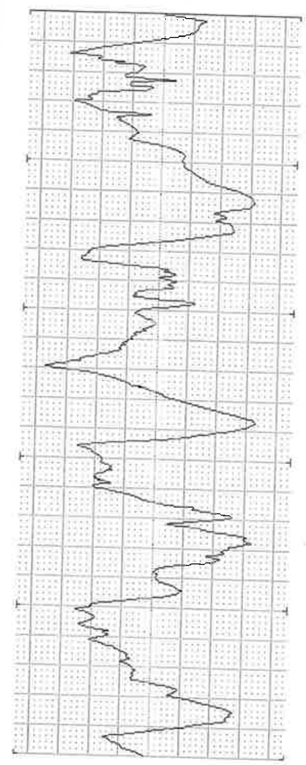

T2

Mitutoyo SurftestSJ-400

DATE 28-03-2008
TIME 02:23:23

R-PROFILE

EVA-L 1.25mm
λc 0.25mmX5

Ra 0.283μm
Rz 1.46μm
Rq 0.363μm
Rt 2.64μm

R-PROFILE

EVA-L 1.25mm
λc=0.25mmX5

×10K

×100

Ver. 1.0μm/cm
Hor. 100.0μm/cm

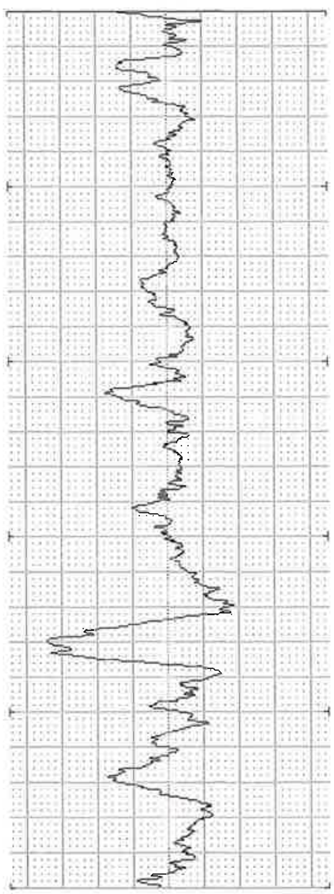

T2

Mitutoyo SurftestSJ-400

DATE 28-03-2008
TIME 02:21:11

R-PROFILE

EVA-L 1.25mm
λc 0.25mmX5

Ra 0.382μm
Rz 1.96μm
Rq 0.474μm
Rt 2.65μm

R-PROFILE

EVA-L 1.25mm
λc=0.25mmX5

×10K

×100

Ver. 1.0μm/cm
Hor. 100.0μm/cm

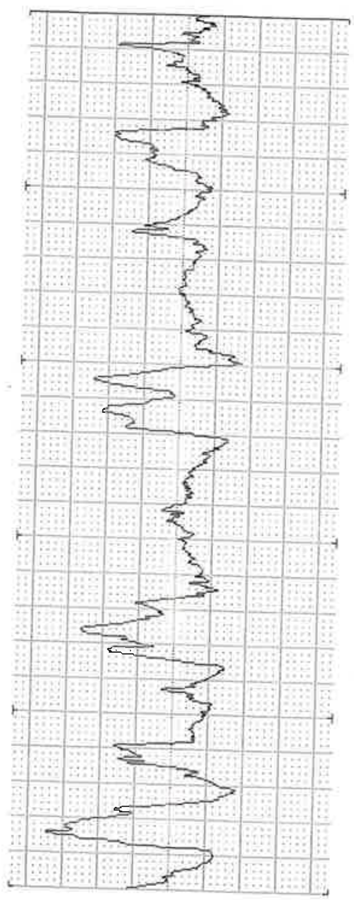

T2

Mitutoyo SurftestSJ-400

DATE 28-03-2008
TIME 02:22:09

R-PROFILE

EVA-L 1.25mm
λc 0.25mmX5

Ra 0.408μm
Rz 2.00μm
Rq 0.503μm
Rt 2.77μm

R-PROFILE

EVA-L 1.25mm
λc=0.25mmX5

×10K

×100

Ver. 1.0μm/cm
Hor. 100.0μm/cm

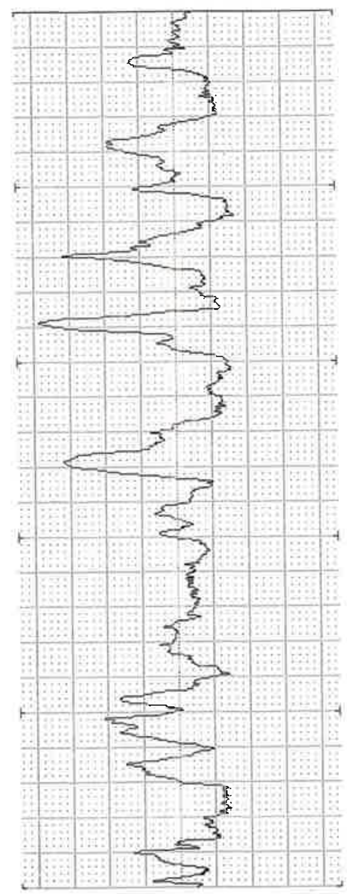

T3 - 140 80

Mitutoyo Surftest SJ-400

DATE 28-03-2008
TIME 02:11:15

R-PROFILE
EVA-L 1.25mm
λc 0.25mmX5

Ra 0.984µm
Rz 4.58µm
Rq 1.168µm
Rt 6.04µm

R-PROFILE
EVA-L 1.25mm
λc=0.25mmX5

×5K
×100

Ver. 2.0µm/cm
Hor. 100.0µm/cm

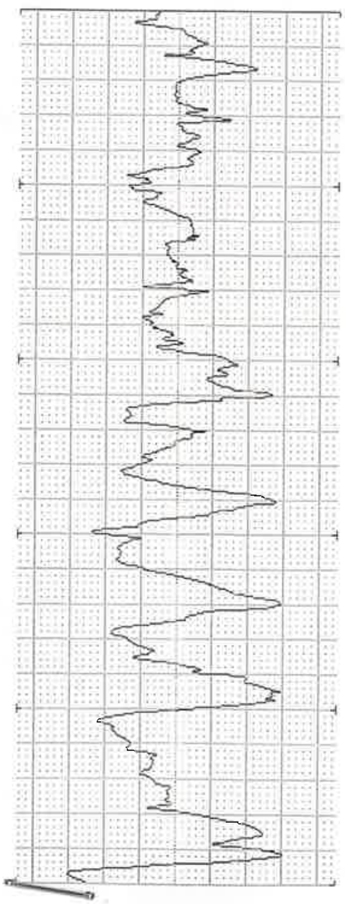

T3 140/80

Mitutoyo Surftest SJ-400

DATE 28-03-2008
TIME 02:25:06

R-PROFILE
EVA-L 1.25mm
λc 0.25mmX5

Ra 0.788µm
Rz 4.38µm
Rq 0.995µm
Rt 6.23µm

R-PROFILE
EVA-L 1.25mm
λc=0.25mmX5

×5K
×100

Ver. 2.0µm/cm
Hor. 100.0µm/cm

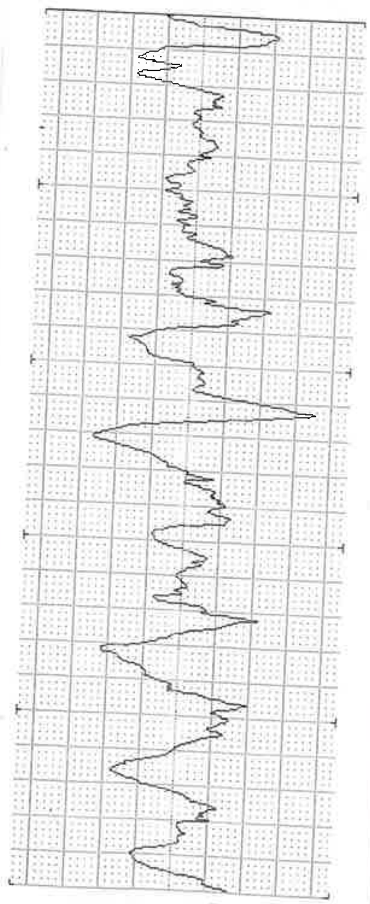

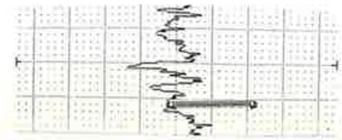

Mitutoyo Surftest SJ-400

DATE 28-03-2008
TIME 02:09:59

T3 140 80

R-PROFILE
EVA-L 1.25mm
λc 0.25mmX5

Ra 0.505µm
Rz 2.68µm
Rq 0.612µm
Rt 4.11µm

R-PROFILE
EVA-L 1.25mm
λc=0.25mmX5

×5K
×100

Ver. 2.0µm/cm
Hor. 100.0µm/cm

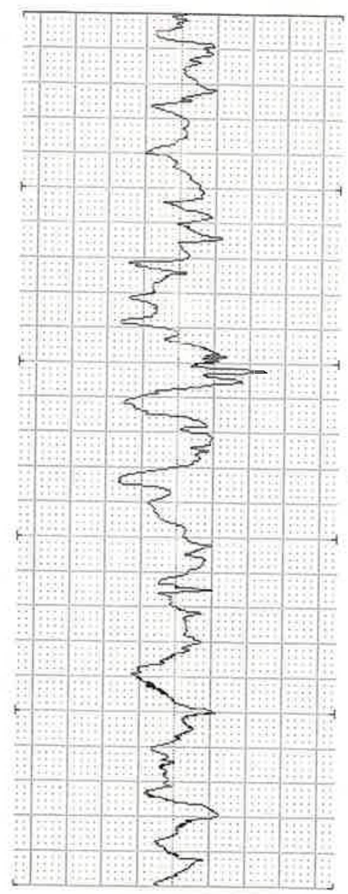

Validatie

Mitutoyo Surftest SJ-400

DATE 28-03-2008
TIME 02:30:03

R-PROFILE
EVA-L 12.5mm
λc 2.5mmX5

Ra 3.024µm
Rz 9.85µm
Rq 3.370µm
Rt 9.99µm

R-PROFILE
EVA-L 12.5mm
λc=2.5mmX5

×2K
×10

Ver. 5.0µm/cm
Hor. 1.0mm/cm

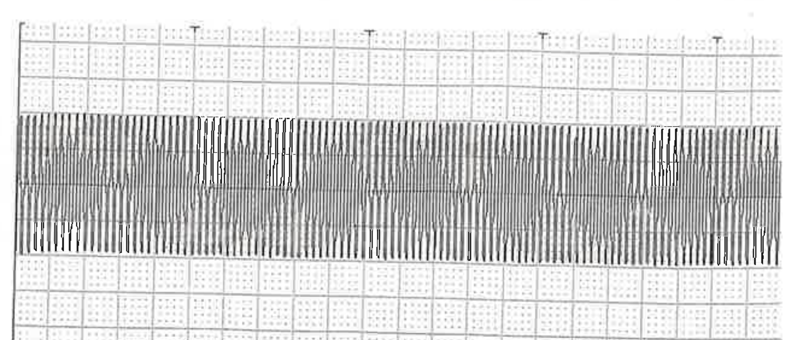

Mitutoyo Surftest SJ-400

DATE 26-10-2008
TIME 03:42:14

R-PROFILE

EVA-L 1.25mm
λc 0.25mmX5

Ra 0.696μm
Rz 3.29μm
Rq 0.828μm
Rt 4.19μm

R-PROFILE

EVA-L 1.25mm
λc=0.25mmX5

×5K

×100

Ver. 2.0μm/cm
Hor. 100.0μm/cm

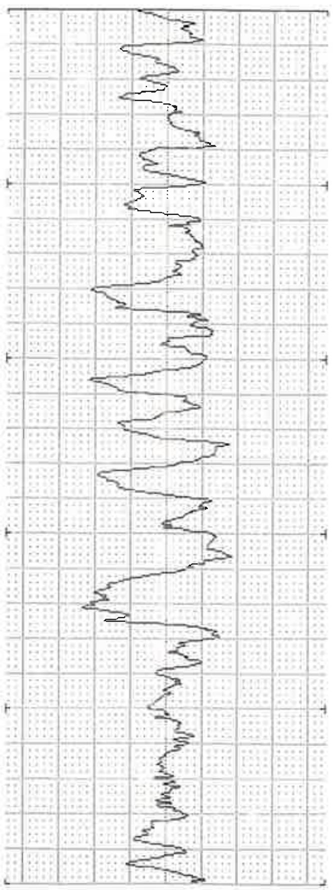

Mitutoyo Surftest SJ-400

DATE 26-10-2008
TIME 03:43:33

R-PROFILE

EVA-L 1.25mm
λc 0.25mmX5

Ra 0.489μm
Rz 2.92μm
Rq 0.625μm
Rt 3.74μm

R-PROFILE

EVA-L 1.25mm
λc=0.25mmX5

×5K

×100

Ver. 2.0μm/cm
Hor. 100.0μm/cm

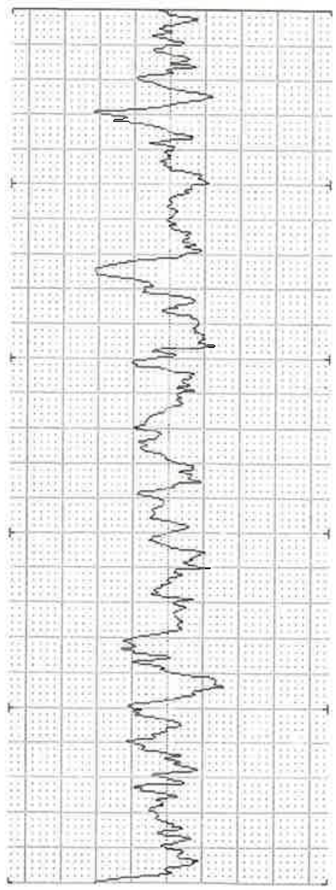

Mitutoyo Surftest SJ-400

DATE 26-10-2008
TIME 03:45:00

R-PROFILE

EVA-L 1.25mm
λc 0.25mmX5

Ra 0.494μm
Rz 2.62μm
Rq 0.606μm
Rt 3.37μm

R-PROFILE

EVA-L 1.25mm
λc=0.25mmX5

×5K

×100

Ver. 2.0μm/cm
Hor. 100.0μm/cm

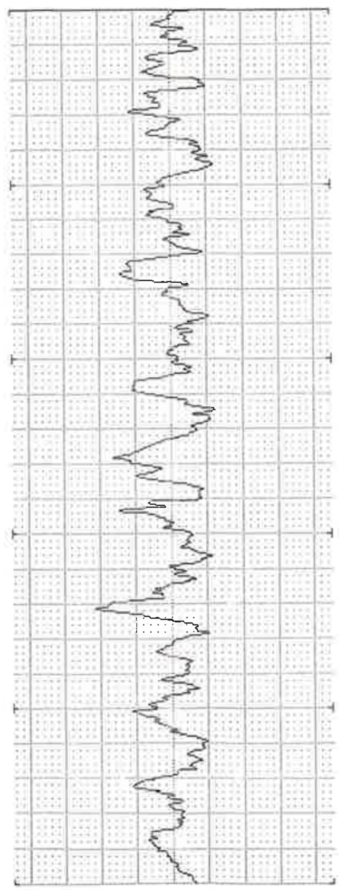

T2 - 3,2 mm

F.1 Measurement equipment

The Mitutoyo SJ-400 version 401 was used to conduct roughness measurements.